Ultrafast Intramolecular and Intermolecular Energy Transfer of Water Molecules in Pure Liquid Water and Aqueous Salt Systems

by

Naveen Kumar Kaliannan

Universität Paderborn, Deutschland

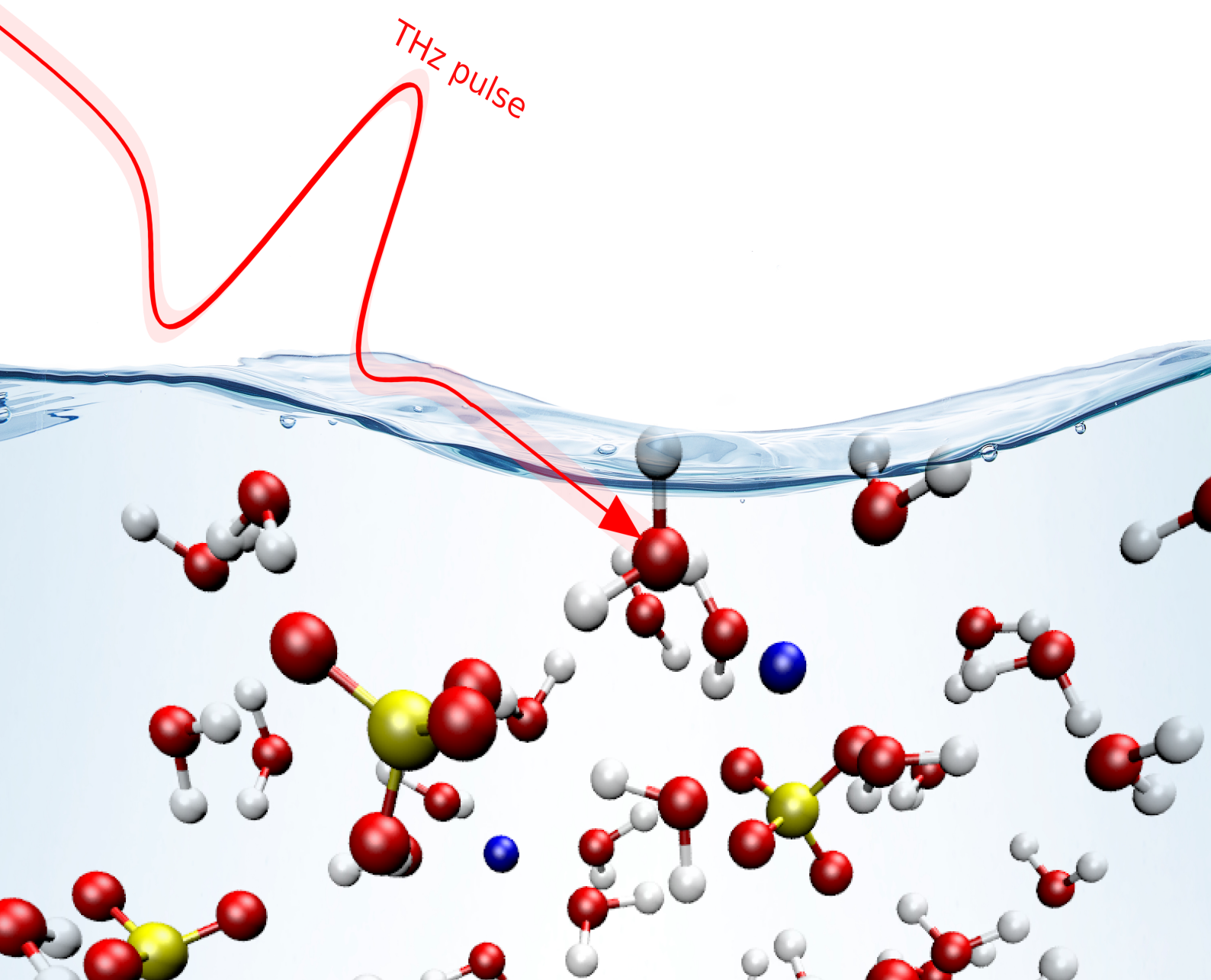

Ultrafast Intramolecular and Intermolecular Energy Transfer of Water Molecules in Pure Liquid Water and Aqueous Salt Systems

by

Naveen Kumar Kaliannan (**Matrikelnummer: 6832870**)

A Ph.D. thesis submitted to the Universität Paderborn for the title Doktor der Naturwissenschaften (Dr. rer. nat.)

Under the guidance of

Prof. Dr. Thomas D. Kühne

Prof. Dr. Matthias Bauer

Dr. Hossam Elgabarty

DYNAMICS OF CONDENSED MATTER
THEORETISCHE CHEMIE
UNIVERSITÄT PADERBORN, GERMANY

APRIL 11, 2023

Declaration

I, **Naveen kumar Kaliannan**, hereby declare that I have written my Ph.D. thesis independently myself, using only the sources and aids documented therein, and that I have cited all quotations. The work was not yet in the same or a similar form as coursework or an examination.

Paderborn, April 11, 2023 Naveen kumar Kaliannan

Acknowledgments

First of all, I would like to thank Prof. Dr. Thomas D. Kühne for giving me a chance to do my Ph.D. work under him. He offered a superb working environment, all the required tools, funding and most importantly, his theoretical knowledge on Density Functional Theory and Molecular Dynamics. It is a pleasure to work with such a wonderful and kind person as him.

I would also like to express my gratitude to Dr. Hossam Elgabarty for his continuous assistance and support for my Ph.D. thesis work and articles. For the completion of my thesis work, the technical discussions I have had with him over the past few years have been very crucial.

I am really grateful to Paderborn University for the generous allocation of computing time on the Noctua and TC-Heisenberg supercomputers and for the accommodations.

A special thanks to all the members of Arbeitskreis Kühne : Britta Fremerey, Dr. Andres Henao Aristizabal, Dr. Hossein Mirhosseini, Dr. Ramya Kormath Raghupathy, Dr. Frederik Zysk, Dr. Julian Heske, Konstantin Tamoev, Karlo Nolkemper, Simon Richter, Dr. Mohsen Sajadi, Dr. Svetlana Pylaeva, Dr. Hendrik Wiebeler, Dr. Sudhir Kumar Sahoo and also to a member of the Fritz Haber Institute: Dr. Vasileios Balos.

I want to express my gratitude to Nallammal, Kaliannan Karupannan, Vaideki Palaniarasu, Shrish Athithya, Navaneetha, Yuvaraj Kumar Ranganathan, Jyoshna Umaiyaal, Nithikshna Nacchiyar for their personal support and inspiration over the years. Last but not least, I would also like to thank my friends Karthik Krishnamurthy, Anto Michael Ronson, Sivakarthik, Adhithyan Krishnaswamy, R Muthu Kumar for always staying around me.

Contents

List of Figures

List of Tables

Units• and Constants⋆

- **Temperature** T - K
- **Length** L - Bohr, Å
- **Time** t - fs, ps
- **Electric field** E - Atomic unit, V.m^{-1} (or J C^{-1} m^{-1})
- **Dipole** μ - Atomic unit, Debye
- **Radial distribution function** g(r) - No unit
- **Mean squared displacement** MSD - Å^2.
- **Polarizability anisotropy** $\triangle\alpha$ - Å^3
- **Polarizability** α - Å^3
- **First hyperpolarizability** β - Å^5
- **Second hyperpolarizability** γ - Å^7
- **Velocity and center of mass velocity** v, v_{com} - Å fs^{-1}
- **Angular velocity** ω - fs^{-1}. Throughout the angular velocity is calculated and reported in 1/time dimension.
- **Auto- and Cross-Correlation Functions** - No Unit
- **Hydrogen bond strength** $\triangle$E - Hartree, kJ mol^{-1}
- ⋆ **Gas constant** R - 8.3144621 J. mol^{-1}. K^{-1}
- ⋆ **Boltzmann constant** k$_B$ - 1.38 $\times$ 10^{-23} J. K^{-1}
- ⋆ **Avagardo's number** N$_A$ - 6.023 $\times$ 10^{23} mol^{-1}
- ⋆ **Pi** π - 3.14159265359.....
- ⋆ **Coulomb's constant** k$_e$ = 8.98755 $\times$ 10^9 J m C^{-2}
- ⋆ **Elementary charge** e = 1.60217 $\times$ 10^{-19} C

Unit Conversions

- 1 THz = 10^{12} Hz
- 1 atomic unit of length = 0.529177249 Å
- 1 fs = 0.001 ps
- 1 atomic unit of electric field = 5.14220652.E11 V.m^{-1} (or J C^{-1} m^{-1})
- 1 atomic unit of dipole moment = 2.541161873 Debye
- 1 Hartree = 2625.5 kJ mol^{-1} = 627.5 kcal mol^{-1}

Abbrevations•, Chemical Symbols⋆ and Formulas△

- **THz** - Terahertz
- **TKE** - THz Kerr effect
- **DID, DID^{1}, DID^{1,2}** - Dipole-induced-dipole, First-order extended DID, First and second-order extended DID
- **MD** - Molecular Dynamics
- **NEMD** - Non-equilibrium Molecular Dynamics
- **AIMD** - Ab initio Molecular Dynamics
- **PFFMD** - Polarizable force field Molecular Dynamics
- **FFMD** - Non-Polarizable force field Molecular Dynamics
- **ALMO-EDA** - Absolutely localized molecular orbital - energy decomposition analysis
- **AMOEBA** - Atomic multipole optimized energetics for biomoleular simulation
- **AMBER** - Assisted Model Building with Energy Refinement
- **SPC** - Simple Point Charge
- **RDF** - Radial distribution function
- **HB, H-bond, HBNs** -Hydrogen bonding, Hydrogen bond, Hydrogen bond networks
- **COM, AV** - Centre of mass, Angular velocity
- **ACF, CCF, ssVVCF** - Auto-Correlation Function, Cross-Correlation Function, surface-specific velocity-velocity correlation function
- **IR, SFG** - Infrared, Sum Frequency Generation

⋆ **H** - Hydrogen

⋆ **O** - Oxygen

⋆ **Mg** - Magnesium

⋆ **Cl** - Chloride

⋆ **Na** - Sodium

⋆ **F** - Fluoride

⋆ **S** - Sulfur

△ **H_2O** - Water

△ **SO_4** - Sulfate

List of publications

1. **Naveen Kumar Kaliannan**, Andres Henao Aristizabal, Hendrik Wiebeler, Frederik Zysk, Tatsuhiko Ohto, Yuki Nagata and Thomas D. Kühne, *"Impact of intermolecular vibrational coupling effects on the sum-frequency generation spectra of the water/air interface"*, Molecular Physics 118, 1620358 (2019).

2. Hossam Elgabarty, **Naveen Kumar Kaliannan** and Thomas D. Kühne, *Enhancement of the local asymmetry in the hydrogen bond network of liquid water by an ultrafast electric field pulse*, Scientific Reports 9, 10002 (2019).

3. Deepak Ojha, **Naveen Kumar Kaliannan** and Thomas D. Kühne, *Time-dependent vibrational sum-frequency generation spectroscopy of the air-water interface*, Communications Chemistry 2, 116 (2019).

4. Hossam Elgabarty, Tobias Kampfrath, Douwe Jan Bonthuis, Vasileios Balos, **Naveen Kumar Kaliannan**, Philip Loche, Roland R. Netz, Martin Wolf, Thomas D. Kühne and Mohsen Sajadi, *Energy Transfer within the Hydrogen Bonding Network of Water Following Resonant Terahertz Excitation*, Science Advances 6, 17 (2020).

5. Vasileios Balos, **Naveen Kumar Kaliannan**, Hossam Elgabarty, Martin Wolf, Thomas D. Kühne, and Mohsen Sajadi, *Time-resolved terahertz–Raman spectroscopy reveals that cations and anions distinctly modify intermolecular interactions of water* Nature Chemistry 14, 1031–1037 (2022).

6. Marie Hartmann, Frederik Zysk, Waldemar Keil, **Naveen Kumar Kaliannan**, Hans Egold, Claudia Schmidt, Christian Weinberger, Thomas D. Kühne, and Michael Tiemann, *The Structure of Water in Silica Mesopores – Influence of the Pore Wall Polarity* Advanced Materials Interfaces 9, 2200245 (2022).

7. **Naveen Kumar Kaliannan**, Hossam Elgabarty, and Thomas D. Kühne, *Simulating bulk polarizability of aqueous ionic solutions with non-equilibrium molecular dynamics and a multipolar expansion* in preparation.

8. **Naveen Kumar Kaliannan**, Hossam Elgabarty, and Thomas D. Kühne, *Intramolecular and intermolecular energy transfer in liquid water revealed by the THz Kerr effect : From theoretical perspective* in preparation.

Abstract

Insights into the structure and dynamics of the hydrogen bonding (HB) network in pure liquid water and aqueous salt systems are essential for understanding many biological, biochemical, and environmental processes at the molecular level. Because the spectroscopic range of the dynamics of HB networks lies in the terahertz (THz) frequency region, the promising novel time-resolved THz-pump-Raman-probe technique can be applied directly to excite/pump the low-frequency collective modes of water with a single-cycle THz pulse, and to track the system's collective polarizability anisotropy responses, which contain both single molecule and molecular collision/interaction-induced responses.

In this thesis work, we have simulated the THz-electric-field-induced transient collective polarizability anisotropy of pure liquid water and several aqueous salt systems, via simple and molecular hyperpolarizabilities extended dipole-induced-dipole (DID) models, using polarizable and non-polarizable force field molecular dynamics (MD) trajectories. The MD trajectories were directly simulated with the effect of a single-cycle THz pulse used in the time-resolved THz Kerr effect (TKE) experiments of Mohsen and Vasileios[1], but with a stronger intensity to overcome statistical problems. Our study demonstrates that the hyperpolarizabilities extended DID model faithfully reproduces several TKE experimental birefringence measurements, while the simple DID model is not enough. The comparisons of polarizability anisotropy results from polarizable and non-polarizable force fields show that the inclusion of induced polarization effects in the force field MD is essential to reproduce the experimentally measured concentration-dependent birefringence of strong aqueous salt systems.

We have related the polarizability anisotropy of SPC liquid water to its separated kinetic energies and rotation-translation cross-correlation functions to understand the effects of the THz pulse on the ultrafast intramolecuar and intermolecular energy transfer of water molecules. When the THz pulse is applied in the x-direction of the system, the intramolecular energy transfer happens from rotation to translation motion of water occurs in the yz- and zy-symmetry. The intramolecular energy transfer process then excites intermolecular energy transfer between two H-bonded water molecules via translation-translation motions in the y and z directions. The ensuing intermolecular energy transfer causes the molecular structural anisotropy and enhanced anharmonicity of the HB. All these explain how the THz pulse energy deposited into the rotational motion of water molecules is transferred into the translational motion of neighboring water molecules, which in turn affects the collision-induced contribution to the collective polarizability anisotropy of aqueous systems.

We have further provided molecular level insights into the ion-induced perturbation of water's HB network by decomposing the polarizability anisotropy of aqueous salt systems. The decomposition reveals that cations strongly increase the polarizability anisotropy of water, while anions suppress it. However, the water shared between an anion and a cation exhibit stronger anisotropy than pure liquid water. In addition, we also find that the TKE transform isotropic polarizability of anions into highly anisotropic, while the cations exhibit almost negligible anisotropy. Our analysis on H-bond strengths using the ALMO-EDA technique suggests that ion-induced effects on H-bond strengths between their first- and second-solvation shells affect the collision-induced contributions significantly, providing new insights into some of the long standing debates about the Hofmeister series.

[1]Nature Chemistry **14**, 1031–1037 (2022) , Science Advances **6**, 17 (2020)

Zusammenfassung

Einblicke in die Struktur und Dynamik des Wasserstoffbrückenbindungsnetzwerks (HB) in reinem flüssigen Wasser und wässrigen Salzsystemen sind für das Verständnis vieler biologischer, biochemischer und umweltbezogener Prozesse auf molekularer Ebene von wesentlicher Bedeutung. Da der spektroskopische Bereich der Dynamik von HB-Netzwerken im Terahertz (THz)-Frequenzbereich liegt, kann die vielversprechende neue zeitaufgelöste THz-Pump-Raman-Probe-Technik direkt angewendet werden, um die niederfrequenten kollektiven Moden von Wasser mit einem THz-Puls mit einem einzigen Zyklus anzuregen/anzuregen und die kollektiven Polarisationsanisotropie-Antworten des Systems zu verfolgen, die sowohl Einzelmolekül- als auch molekulare kollisions-/interaktionsinduzierte Antworten enthalten.

In dieser Arbeit haben wir die THz-elektrische Feld-induzierte transiente kollektive Polarisierbarkeitsanisotropie von reinem flüssigem Wasser und mehreren wässrigen Salzsystemen über einfache und molekulare Hyperpolarizitäten mit erweiterten Dipol-induzierten-Dipol (DID)-Modellen unter Verwendung von polarisierbaren und nicht-polarisierbaren Kraftfeld-Molekulardynamik (MD) Trajektorien simuliert. Die MD-Trajektorien wurden direkt mit der Wirkung eines Einzelzyklus-THz-Pulses simuliert, der in den zeitaufgelösten THz-Kerr-Effekt (TKE)-Experimenten von Mohsen und Vasileios verwendet wurde[2], jedoch mit einer stärkeren Intensität, um statistische Probleme zu überwinden. Unsere Studie zeigt, dass das erweiterte DID-Modell für Hyperpolarizitäten mehrere experimentelle TKE-Doppelbrechungsmessungen getreu reproduziert, während das einfache DID-Modell nicht ausreicht. Der Vergleich der Ergebnisse der Polarisationsanisotropie von polarisierbaren und nichtpolarisierbaren Kraftfeldern zeigt, dass die Einbeziehung von induzierten Polarisationseffekten in das Kraftfeld-MD wesentlich ist, um die experimentell gemessene konzentrationsabhängige Doppelbrechung von starken wässrigen Salzsystemen zu reproduzieren.

Wir haben die Polarisierbarkeitsanisotropie von SPC-Flüssigwasser mit seinen getrennten kinetischen Energien und Rotations-Translations-Kreuzkorrelationsfunktionen in Beziehung gesetzt, um die Auswirkungen des THz-Pulses auf den ultraschnellen intramolekularen und intermolekularen Energietransfer von Wassermolekülen zu verstehen. Wenn der THz-Puls in der x-Richtung des Systems angelegt wird, geschieht der intramolekulare Energietransfer von der Rotations- zur Translationsbewegung des Wassers in der yz- und zy-Symmetrie. Der intramolekulare Energietransfer regt dann den intermolekularen Energietransfer zwischen zwei H-gebundenen Wassermolekülen durch Translation-Translation-Bewegungen in y- und z-Richtung an. Der daraus resultierende intermolekulare Energietransfer verursacht die molekulare strukturelle Anisotropie und die erhöhte Anharmonizität des HB. All dies erklärt, wie die in die Rotationsbewegung von Wassermolekülen eingebrachte THz-Pulsenergie in die Translationsbewegung benachbarter Wassermoleküle übertragen wird, was wiederum den kollisionsbedingten Beitrag zur kollektiven Polarisierbarkeitsanisotropie wässriger Systeme beeinflusst.

Durch die Zerlegung der Polarisierbarkeitsanisotropie wässriger Salzsysteme haben wir weitere Einblicke in die ioneninduzierte Störung des HB-Netzwerks von Wasser auf molekularer Ebene gewonnen. Die Zerlegung zeigt, dass Kationen die Polarisierbarkeitsanisotropie von Wasser stark erhöhen, während Anionen sie unterdrücken. Das Wasser, das von einem Anion und einem Kation geteilt wird,

[2]Nature Chemistry **14**, 1031–1037 (2022) , Science Advances **6**, 17 (2020)

weist jedoch eine stärkere Anisotropie auf als reines flüssiges Wasser. Darüber hinaus stellen wir fest, dass die TKE die isotrope Polarisierbarkeit von Anionen in eine stark anisotrope verwandelt, während die Kationen eine fast vernachlässigbare Anisotropie aufweisen. Unsere Analyse der H-Bindungsstärken mit Hilfe der ALMO-EDA-Technik deutet darauf hin, dass ioneninduzierte Effekte auf die H-Bindungsstärken zwischen ihren ersten und zweiten Solvatationsschalen die kollisionsinduzierten Beiträge erheblich beeinflussen, was neue Einblicke in einige der seit langem bestehenden Debatten über die Hofmeister-Reihe bietet.

Chapter 1

Introduction

Liquid water is the most abundant liquid on earth. It has a number of unique and anomalous properties such as density maximum at 277K (4°C), numerous crystalline polymorphs, high surface tension, isothermal compressibility and heat capacity divergences at 228 K (−45°C) [1–5]. Moreover, it also dissipates energy very quickly [6] and more efficiently than many other liquids. All these anomalies are generally attributed to water's ability to form and break a fluctuating three-dimensional hydrogen bonding (HB) network that, on average, organizes water molecules into tetrahedral structures [4]. The complex collective and cooperative intermolecular degrees of freedom within the fluctuating HB network have a very diverse dynamics [7–9] that occurs on sub-picosecond to pico-second timescales [10,11], which corresponds to the spectroscopic range of 10^{-1} – 10^{3} cm^{-1} [12]. Insights into the HB network structure and the associated diverse dynamics are central not only for understanding the anomalous properties of liquid water, but also for understanding many biological, biochemical, and environmental processes [13–18] at the molecular level.

In addition to the HB network characteristics of pure liquid water, it is also important to understand the physical nature of ion-induced perturbation of water's HB network in aqueous solutions because the water molecules in natural environments and biological organisms always contain ions [19] and interact electrostatically with them. Besides their existence, they significantly affect the conductivity, thermodynamics, and many other characteristics of aqueous solutions [20] that have been exploited in wide range of applications. For example, consuming ion-rich water alters calcium and glucose concentrations in human body [21], and has an important effect on cell survival. The use of ions in aqueous solutions has also been very advantageous for the processing and storage of inorganic toxic waste, and radioactive nuclear waste in geological salt formations [22,23]. Furthermore, ion contained aqueous solutions have been employed to boost the durability, power, and efficiency of lithium-ion [24] and flow batteries [25] as well as to address their safety and environmental concerns. More importantly, ion solvation have a strong ability to alter a variety of biological processes, including the folding and unfolding of proteins and enzymes [26–28].

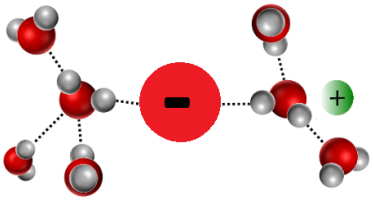

Figure 1.1: Anion interact with water molecules by forming H-bonds, while the cation interact electrostatically with the partially negatively charged oxygen atoms and polarize the water molecules.

Ion-water (solute-solvent) interactions are traditionally categorized as either kosmotropes (structure makers) or chaotropes (structure breakers) [29,30] based on the ion ability to disturb water structuring, as shown in Figure 1.1. The Hofmeister series [30] ranks the ions according to how well they can stabilize or destabilize proteins. Most ion-water interactions are driven by the van der Waals (dipole-dipole, dipole-induced-dipole and London dispersion (induced-dipole-induced-dipole) interactions), hydrogen bonding, ion (charge)-dipole, ion (charge)-induced-dipole and charge-charge interactions. Such interactions can also alter water—water (solvent-solvent) interactions or hydrogen bond (H-bond) strengths up to some distance from the solute position. The ion effects on water HB network characteristics are known to be concentration-dependent; at low concentrations, the influence is little, while at greater concentrations, the effect is significant. In particular, the water molecules that are closest to the ions are strongly influenced and are generally referred to as "hydration" or "solvation" water. One important aspect of ion-water interactions is the extent to which ions structurally or dynamically disturb the HB network of water molecules in aqueous solutions.

Through the use of both theoretical [31–34] and experimental [35–45] techniques, the HB network properties and solute-solvent interactions of aqueous solutions have been well explored in the past decades. Energy decomposition analysis based on absolutely localized molecular orbitals (ALMO-EDA) [7,31–34,46,47] has been employed to calculate the interaction energies of solute-solvent and solvent-solvent interactions in aqueous systems. The method quantified the energy profiles of water-ion and water-water interactions [34] as well as the heterogeneity in the HB network characteristics [9,48]. Ultrafast infrared spectroscopy has explored the HB network structure and associated dynamics of water in aqueous salt solutions through the intramolecular OH stretch vibrations of water [37,49–51]. The technique observed a decrease in OH stretch frequency and an increase in librational and HB intermolecular motions [50], hence revealing that the water HB network becomes stronger as salt concentration increases. Optical Kerr effect (OKE) techniques have studied the microscopic origin of the ion effects on the orientational dynamics, relaxation time constants, diffusion, rotational correlation of water and etc [52]. Non-linear vibrational spectroscopy technique, particularly surface-sensitive vibrational sum-frequency generation (SFG) techniques [53–63], are primarily employed to characterize the structure and dynamics of distorted HB network at the aqueous interfaces. Thanks to quantum mechanical selection rules of the SFG techniques, the SFG signal vanishes in centrosymmetric or isotropic bulk media and is only active at interfaces or surfaces, where the symmetry is broken. Dielectric spectroscopy was used to measure the dielectric spectra of water, which contain the mixed HB modes and debye-like modes [64,65], as shown in Figure 1.2. Whereas the Raman spectrum of liquid water lacks the debye-like modes. The time-resolved terahertz (THz)-pump-Raman-probe is of special interest [41–43,66–70] to study the low-frequency collective modes of aqueous systems, since it directly excite/pump the dielectric ps and sub-ps motions, i.e., the time scale at which water's intermolecular motions such as translation (HB bending and HB stretching modes) and rotation (libration modes) are active [71]. Hence, we will use this latter technique extensively in our research investigation.

In a typical process of a time-resolved THz-pump-Raman-probe experimental measurement, as depicted in the Figure 1.3, a time-dependent THz electric field E excites the collective rotational degrees of freedom of molecules, hence exerting a torque or rotational force [68],

$$\tau = -\mu \times E \tag{1.1}$$

$$\mu = \mu_{perm} + \mu_{ind}$$

on molecules by coupling into the permanent (μ_{perm}) and induced (μ_{ind}) molecular dipole moments (μ), which partially aligns the dipole moment along the field direction [68–70,72]. As a result, the system exhibits dielectric anisotropy, resulting in optical birefringence $\triangle n$[1] (THz Kerr effect, TKE), which is obtained by the changes in a time-delayed 800 nm off-resonant Raman pulse transpassing the sample

[1]Birefringence is defined by the difference $\triangle n = n_{\parallel} - n_{\perp}$ between the refractive indices along parallel and perpendicular directions

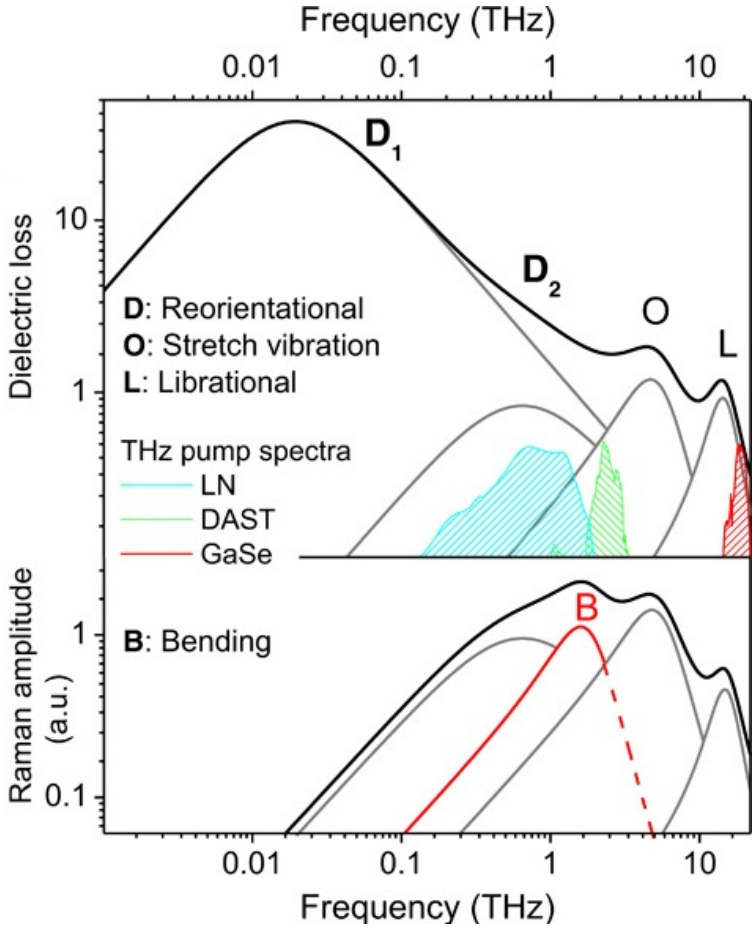

Figure 1.2: Equilibrium dielectric loss and incoherent Raman spectra of water [64]. Two Debye processes and two vibrations (network stretch vibrations and single-molecule hindered rotation, libration) are typically sufficient to fit the dielectric spectrum of water [65]. The Raman spectrum of water lacks the first Debye process [64], but the H-bond bending vibration (red line) gains a significant amplitude. The spectra of the excitation THz fields at 1, 3, and 19 THz are indicated by the cyan, green, and red dashed areas, respectively. a.u., arbitrary units.

and by combining the measured amplitude and phase information in TKE experiments. Since the THz pulse excites the intermolecular motions of molecules rather than the motions from intramolecular ones, this technique has been proven successful in studying the deformation of molecular electron clouds, HB interactions, librations, Van der Waals dispersion forces, solvent-solute interactions in liquids and aqueous solutions [41–44,67–70]. It is also well know that the refractive index or dielectric constant of a system is proportional to the total polarizability of all the molecules, according to the Lorentz-Lorenz [73] or Clausius–Mossotti [74] equations. Hence, both birefringence $\triangle n$ and polarizability anisotropy $\triangle\alpha$[2] can be directly related, and the TKE experimental results can be readily modeled by theory.

The polarizability anisotropy of a system can be calculated via various first-principle theoretical approaches such as Density Functional Perturbation Theory and Wannier functions [75–81]. These approaches have been demonstrated to accurately determine the Raman spectra of liquid water, ionic solutions and various organic chemical compounds [79,81,82]. Recently, machine learning and deep neural

[2] As in the case of birefringence, the polarizability anisotropy $\triangle\alpha$ of a system can be mathematically calculated as the difference $\triangle\alpha = \alpha_{\parallel} - \alpha_{\perp}$ between systems' polarizability in directions, parallel and perpendicular to the applied field direction.

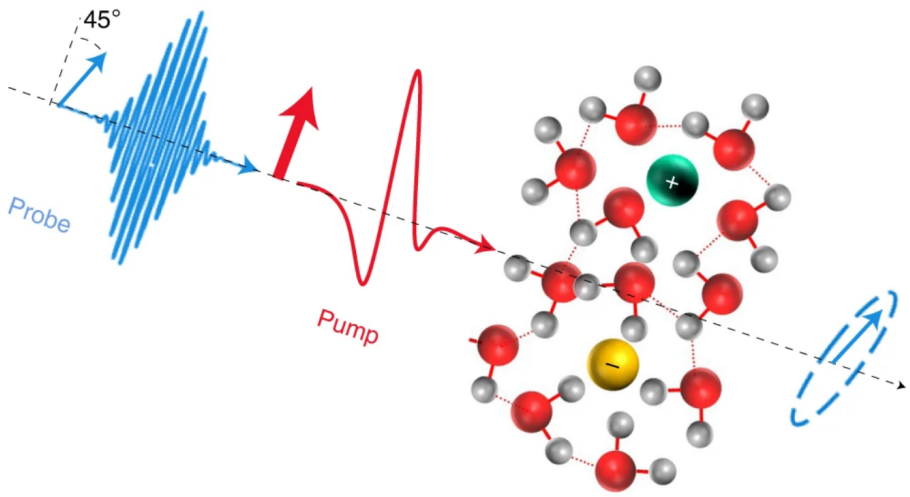

Figure 1.3: Time-resolved THz-pump-Raman-probe experimental process. An intense THz pump pulse induces optical birefringence in the solution. The effect is monitored by an optical probe pulse that becomes elliptically polarized upon traversing through the medium.

network models were trained to predict the maximally localized Wannier function centers and compute the molecular polarizabilities of liquid water and various organic molecules [83,84]. Although these approaches are recognized to be the most accurate methods, they are still computationally expensive, which makes them unsuitable for treating larger systems and lengthy simulations. Classical dipole-induced-dipole (DID) model, on the other hand, is a computationally cheaper but still powerful model to compute atomic, bond and molecular polarizabilities for larger systems [52,61,85–93]. The accuracy of the DID model can also be improved by involving the anisotropic components of polarizability [33,94], the hyperpolarizability-local electric field interaction effects [95–100], the dipole-quadrupole polarizability effects [101] and by making the polarizabilities as a function of the inter-atomic distances [102,103].

The accuracy of the polarizability anisotropy calculation also depends on the degree to which the molecular dynamics (MD) trajectories correctly reproduce the structure and dynamics of an experimental molecular system. The most precise way for calculating the polarizability anisotropy is to use trajectories generated from the *ab initio* MD (AIMD) simulations, since the MD forces are determined on-the-fly on the basis of the potential energy obtained using the electronic structure theory [104,105]. However, this is unlikely to be achieved for larger systems or longer MD trajectories owing to the computationally costly nature of computing polarizability using AIMD simulation. Classical MD simulations, on the other hand, employs force fields to describe the potential energy of a system, and are recognized as the fastest way for simulating bigger systems and long MD trajectories, although it is less accurate in prediction [106]. However, by adding induced polarization effects in the force field MD, a fair compromise between accuracy and computational cost can be reached [107–113]. Furthermore, as compared to non-polarizable force fields, polarizable force-fields have been demonstrated to be significantly better at modeling the Kerr response and spectra of hydrogen-bonded liquids [88]. In most simulation research works, the OKE polarizability anisotropy response estimated from the correlation function of the system polarizability has been investigated for liquids and aqueous solutions systems [52,97,114–120], but not the TKE-induced collective polarizability anisotropy responses, which will be the major emphasis of this thesis study.

The main focus of this thesis is to complement the time-resolved THz-pump-optic-Raman-probe experiments [48,121] conducted to deeply understand the intermolecular HB, intermolecular energy transfer and solvent-solute interactions in pure liquid water and aqueous salt systems. For this purpose, we have performed non-equilibrium (DFT based ab initio, non-polarizable force fields, polariz-

able force fields) MD simulations of liquid water and several aqueous salt systems under the effect of the same THz field but with a stronger intensity. In addition, we have employed the extended DID formalism to calculate the simulated systems's (TKE-induced) transient-collective-polarizability anisotropy responses, which contain both single molecule and molecular collision/interaction-induced responses. In order to demonstrate the accuracy of our formalism, the obtained simulation results are compared to TKE experimental measurements from different research groups. Furthermore, we have employed ALMO-EDA to measure the strength of HBs in pure liquid water and several aqueous salt solutions. The effects of cations and anions on water-water H-bond strengths and solvation water polarizability anisotropy are investigated, which helps to understand the intermolecular energy transfer and solvent-solute interactions in aqueous salt systems.

The structure of this thesis is as follows: The simulation techniques and concepts that we used for this thesis study are covered in Chapter 2. Chapter 3 presents the details, types and specifics regarding the simulation techniques parameters. Chapter 4 derives the extended DID formalism in order to accurately determine the molecular polarizabilities, dipole moment and polarizability anisotropy of water and ions in condensed matter as well as in an external electric field. Chapter 5 unravels the intra- and inter-molecular energy transfer of water molecules in liquid water during the TKE. This is mainly achieved by employing the Intra- and Inter-molecular rotation-translation coupling cross-correlation functions. Chapter 6 presents the effects of cations and anions on the intermolecular HB interactions and solvation water polarizability anisotropy via ALMO-EDA and DID formalism, providing new insights into some of the long standing debates about the Hofmeister series. In Chapter 7, the effects of intermolecular vibrational coupling effects of the O-H stretch modes on the simulated sum-frequency generation spectra of the water/air interface are investigated. In addition, we have presented the correlation between interface water structure and their SFG signal to better understand the water/air interface. Chapter 8 provides a summary of the thesis study.

Chapter 2

Computational methodology

In this chapter, we explain the concept of polarizable and non-polarizable force field molecular dynamics, the basics involved in them, and various other frameworks such as energy decomposition analysis based on absolutely localized molecular orbitals, kinetic energy decomposition, dipole-induced-dipole formalism, auto- and cross-correlation functions, pair correlation function and etc that we employed for this thesis work.

2.1 Molecular Dynamics

Molecular dynamics (MD) is a computational method for simulating gases, liquids, and solids under various thermodynamic circumstances that is widely utilized in the fields of physics, chemistry, and material sciences [106]. The trajectories defining the motion of atomic nuclei are generated in MD over a period of time by computing the forces acting on the nuclei at each time step. The generated MD trajectories can be used to determine various types of of spectra [8,58,59,61,105,122,123], structures [8,105], thermodynamic, dynamic [8,52,89,124] and many other properties. The determined properties can be directly compared to experimental data.

The most often used MD methods are Density Functional theory (DFT) based *Ab-initio* MD and force field MD. Since the force acting on the atomic nuclei is calculated on-the-fly on the basis of the potential energy obtained from electronic structure methods, DFT based *Ab-initio* MD [8,104,105] is considered to be the most accurate method but is very expensive in terms of computing, as a result, they are not well suited for treating larger systems, lengthy simulations and signal to noise ratio problems. The force fields MD [125], on the other hand, employs simple empirical functions to represent the potential energy, and is hence recognized as the fastest way for simulating bigger systems, although it is less accurate in prediction. However, a good balance between accuracy and computational cost can be achieved by including polarization effects [107–109] in force field MD, which is why it is a suitable method for our research work. Hence, we have carried out the majority of this thesis work with the force field MD and a small part with DFT based *Ab-initio* MD.

The theory and concepts of DFT based *Ab-initio* MD are omitted in this work.

In force field MD, the time evolution of atomic configurations is determined by integrating the newtons equation of motion [106,126],

$$m_i \frac{d^2 r_i}{dt^2} = F_i \tag{2.1}$$

$$F_i = -\frac{\partial}{\partial r_i} U(r_1, r_2, ..., r_N) \tag{2.2}$$

where m_i is the mass of atom i and F_i is the force acting on the ith-atom. The forces are obtained from the gradient of the potential energy $U(r_1, r_2, ..., r_N)$ with respect to atomic coordinates, while

the potential energy is calculated using the force fields. The effects of external electric field $E(t)$ can also be incorporated in force field MD by adding the electric force term [127],

$$F_i^{Ext} = kq_iE(t) \tag{2.3}$$

in the F_i term on the right hand side of the equation 2.1. In the equation, q_i is the fixed partial charge of atom i, k is a unit conversion factor equal to 1185.859, which gives force in kcal per Å per mol, when $E(t)$ is in atomic unit. The $E(t)$ can be fixed as a constant or varying over time depending on the scenarios. This kind of MD is generally called as non-equilibrium MD [106].

2.1.1 Velocity-Verlet integrator

There are several numerical algorithms such as Velocity-Verlet [128], reversible reference system propagator [129], stochastic dynamics [130] and leapfrog integrator [130] that can accurately integrate the newtons equation of motion. In our work, we have employed Velocity-Verlet integrator scheme since it offers numerical stability, numerical accuracy and time reversibility [128,131]. The Velocity-Verlet algorithm uses positions $r(t)$, velocities $v(t)$ propagated from the accelerations at t and $t - \triangle t$, and accelerations $a(t)$ computed from the forces F, in order to calculate the new positions $r(t + \triangle t)$ and new velocities $v(t + \triangle t)$ at $t + \triangle t$. The equations used to calculate $r(t + \triangle t)$ and $v(t + \triangle t)$ at $t + \triangle t$ are given by,

$$r(t + \triangle t) = r(t) + v(t)\triangle t + \frac{1}{2}a(t)\triangle t^2 \tag{2.4}$$

$$v(t + \triangle t) = v(t) + \frac{1}{2}[a(t) + a(t + \triangle t)]\triangle t \tag{2.5}$$

where $\triangle t$ is the time step, which must be properly selected to avoid systematic and statistical errors [132,133] in numerical integration.

2.1.2 Force Fields

The accuracy of force field MD simulations depends on the choice of force fields, i.e., a collection of empirical potential functions and associated parametric constants to describe the potential energy of a system as a function of atomic position [106,134]. There are many types of force fields available in the literature, specifically for the MD simulations of aqueous salt solutions [109,125]. The most commonly used force fields are non-polarizable fixed-charge force fields : AMBER(Assisted Model Building with Energy Refinement) [135–137], CHARMM(Chemistry at HARvard Macromolecular Mechanics) [138–142], GROMOS (Groningen Molecular Simulation) [143], COMPASS [144], and OPLS (Optimized Potential for Liquid Simulations) [145,146], in conjunction with water models : SPC (simple point charge) [147,148] and TIP (Transferable Intermolecular Potential) [149,150] series. The former ones were in fact developed for protein, organic compound, and biomolecular simulations, respectively. As a result, they contain parametric constants and potential functions for different varieties of atoms, molecules, and ions. The chief advantage of them is that they offer transferability of ion parameters [151] to several molecules as well as to several water models. However, the shortcomings of non-polarizable force fields are that they underestimate or overestimate various properties such as vaporization enthalpies [152], ion hydration free energies [109], ion diffusion coefficients [153–155], water self-diffusion coefficients [111,112], viscosity, and surface phenomena [156]. The latter ones are developed in a way to reproduce the density, structure, vibrational spectra, and dynamics of liquid water [59,147,148,157].

Polarizable force fields : AMOEBA (atomic multipole optimized energetics for biomoleular simulation) [112,158–161] and CHARMM Drude [162,163] are becoming popular nowadays, since they include the important effects such as permanent electrostatics and polarization via induced dipole, fluctuating charge, and classical drude oscillator models [164–166]. Inclusion of such effects has significantly improved several properties, even though it comes at the price of higher computational cost. Compared

to others, AMOEBA force field is superior in describing heat of vaporization [109,112], dielectric constant [109,112], surface tension [112], ion dynamics [152,167,168], ion-water interaction energies [33,34], and water residence times in the hydration shell [169].

To contribute various information to our thesis study, we use two separate force fields, AMOEBA and AMBER/SPC, one from polarizable force fields and the other from non-polarizable force fields. This variety also allows us to investigate how induced polarization effects affect THz-induced polarizability anisotropy responses.

AMOEBA model

The AMOEBA force field has the following functional form for all atomic interactions [158],

$$U(r) = U_{\text{bond}} + U_{\text{angle}} + U_{\text{b}\theta} + U_{\text{oop}} + U_{\text{torsion}} + U_{\text{vdw}} + U_{\text{Permanent}} + U_{\text{Polarization}} \tag{2.6}$$

The first five terms represent the short-range valence interactions: bond stretching, angle bending, stretching-bending coupling, out-of-plane bending and torsion. The last three terms are the non-bonded interactions: van der Waals, permanent electrostatic and polarization contributions. The final two terms, polarization and permanent electrostatics energy, are computationally expensive to obtain. The functional forms for bond stretching, angle bending, stretching-bending coupling, out-of-plane bending and torsion are given by:

$$U_{\text{bond}} = K_b(b-b_0)^2[1 - 2.55(b-b_0) + \frac{7}{12}2.55(b-b_0)^2] \tag{2.7}$$

$$U_{\text{angle}} = K_\theta(\theta-\theta_0)[1 - 0.014(\theta-\theta_0) + 5.6*10^{-5}(\theta-\theta_0)^2 + 7*10^{-7}(\theta-\theta_0)^3 + 2.2*10^{-8}(\theta-\theta_0)^4] \tag{2.8}$$

$$U_{\text{b}\theta} = K_{b\theta}[(b-b_0) + (b^{'} - b_0^{'})](\theta-\theta_0) \tag{2.9}$$

$$U_{\text{oop}} = K_\chi \chi^2 \tag{2.10}$$

$$U_{\text{torsion}} = \sum nK_{n\phi}[1 + cos(n\phi \pm \delta)] \tag{2.11}$$

where b_0 and θ_0 are the equilibrium bond lengths and angles, b, $b^{'}$ and θ, $\theta^{'}$ are the bond lengths and angles, K is the force constant. Equation 2.10 is the Wilson-Decius-Cross function and used at sp^2-hybridized trigonal centers to control the out-of-plane bending

The van der Waals interactions are represented using the buffered 14-7 potential functional form due to its strong ability in providing better fits to gas phase *ab-initio* results [170]. The functional form is give by the following equation,

$$U_{\text{vdw}} = \epsilon_{ij}\left[\frac{1.07}{\rho_{ij}+1.07}\right]^7\left[\frac{1.12}{\rho_{ij}^7+0.17} - 2\right] \tag{2.12}$$

where ϵ_{ij} is the potential well depth and $\rho_{ij} = \frac{r_{ij}}{r_{ij}^0}$, where r_{ij} is the norm distance between atoms i and j. r_{ij}^0 is the minimum energy distance. The van der Waals parameters are derived by fitting to both gas phase and bulk phase experimental properties. The combination rules for calculating the ϵ_{ij} and r_{ij}^0 are given by [170],

$$\epsilon_{ij} = \frac{4\epsilon_{ii}\epsilon_{jj}}{(\epsilon_{ii}^{\frac{1}{2}} + \epsilon_{jj}^{\frac{1}{2}})^2} \qquad r_{ij}^0 = \frac{(r_{ii}^0)^3 + (r_{jj}^0)^3}{(r_{ii}^0)^2 + (r_{jj}^0)^2} \tag{2.13}$$

The total permanent electrostatic energy is calculated as the double loop over all atomic pairs

$$U_{\text{Permanent}} = \frac{1}{2}\sum_{i=1}^{N-1}\sum_{j=i+1}^{N} M_i^T T_{ij} M_j \tag{2.14}$$

where the T_{ij} is the interaction tensor as a function of distance between atoms i and j, M_i and M_j are the permanent multipoles ($M = [q, \mu, Q]^T$) of atoms i and j, which contain their charge (q) or monopole , dipole (μ), and quadrupole (Q) moments. The values of the multipoles are derived from ab initio calculations of the small molecules using Stone's distributed multipole analysis (DMA) [171,172].

The polarization energy is calculated as the following,

$$U_{\text{Polarization}} = -\frac{1}{2}\sum_i (\mu_i^{\text{ind}})^T E_i^P \tag{2.15}$$

where the $(\mu_i^{\text{ind}})^T$ is the transpose of induced dipole vector of atom i and E_i^P is the electric field vector at atomic site i created by all the surrounding permanent multipoles. The induced dipole is computed using the induced point dipole model. The basic idea of the dipole model is that the induced dipole μ_i at each atomic site i is calculated via,

$$\mu_i^{\text{ind}} = \alpha_i E_i = \alpha_i(\sum_{i\neq j} T_{ij} M_j + \sum_{i\neq j} T_{ij}\mu_j^{\text{ind}}) \tag{2.16}$$

where α_i is the isotropic atomic polarizability of atom i and E_i is the electric field created at atomic site i by all the surrounding induced dipoles (μ^{ind}) and permanent multipoles ($M = [q, \mu, Q]^T$). $T_{ij} = 3\vec{r}_{ij}\vec{r}_{ij}^T/r_{ij}^5 - I/r_{ij}^3$ is the standard dipole-dipole interaction tensor [85,86] between atoms i and j, $\vec{r}_{ij}$ and r_{ij} are the distance vector and norm distance from atom i to j, I is a 3×3 unit tensor. Thole exponential damping function [85,86] was used to avoid the "polarization catastrophe" when atoms are very closer. The damping function is expressed as,

$$\rho = \frac{3a}{4} exp(-au^3) \tag{2.17}$$

where $u = r_{ij}/(\alpha_i\alpha_j)^{1/6}$ and a is a dimensionless width parameter of the smeared charge distribution and controls the strength of damping. The parameters and atomic polarizabilities are parameterized from *ab-initio* calculations on gas phase monomers [173]. Since the induced dipole variable appears on both sides of the equation 2.16, the equation must be solved self-consistently via iterations. For solving it, there are different schemes such as preconditioned conjugate gradient, optimized perturbation theory and extended-Lagrangian/self consistent field schemes employed [174–179]. We have used the preconditioned conjugate gradient iterative scheme for our simulations due to its faster convergence and computational efficiency for large scale simulations [178,179].

The effects of external electric field E^{ext} are treated in induced dipole at each atomic site by adding the expression k α_i E^{ext} on the right hand side of the equation 2.16. The unit conversion factor k = 3.567 gives the dipoles in Å^2, when the E and α are in atomic unit and Å. The effects are treated before the self-consistently cycle in order to reduce the computational cost.

AMBER/SPC model

The AMBER/SPC force field [135–137,147,148], unlike the AMOEBA force field, has a simple functional form and is typically written as

$$U(r) = \sum_{i<j} K_b(b_{ij}-b_0)^2 + \sum_{i<j<k} K_\theta(\theta_{ijk}-\theta_0)^2 + \sum_{i<j<k<l} \frac{K_{n\phi}}{2}[1+cos(n\phi-\gamma)] + \sum_{i<j} 4\epsilon_{ij}\left[(\frac{\sigma_{ij}}{r_{ij}})^{12} - (\frac{\sigma_{ij}}{r_{ij}})^6\right] \tag{2.18}$$

Here the first three terms represent the bonded interactions: bond stretching, angle bending and torsion. The final term is van der Waals interactions, which is represented by the Lennard-Jones potential function (12-6) [180]. Here the ϵ_{ij} and σ_{ij} are calculated using the combination rules given by

$$\epsilon_{ij} = \sqrt{\epsilon_i\epsilon_j} \qquad \sigma_{ij} = \frac{\sigma_i + \sigma_j}{2} \tag{2.19}$$

The σ_{ij} is calculated by arithmetic average, while the ϵ_{ij} is calculated by the geometric rules [170].

2.1.3 Long-range electrostatic interactions in periodic systems

The total electrostatic energy of a simulation system can be calculated as the summation over all atom-pairwise coulombic interactions within the original simulation cell, between original and replicated simulation cells,

$$U_{\text{Coulomb}} = \frac{1}{2}\sum_{\vec{n}}\sum_{i}\sum_{j}\frac{q_i q_j}{|r_{ij}+\vec{n}|} \tag{2.20}$$

where q_i,q_j represent the fixed partial charges of atom i and j, r_{ij} is the distance between them, $\vec{n} = [n_x.L_x, n_y.L_y, n_z.L_z,]$ is the lattice vector of the original and replicated cells, L is length of the original simulation box and $n = 0, \pm1, \pm2, ., .,$. The r_{ij}^{-1} term in the equation 2.20 decays very slowly, as a result, it is essential to replicate the original cell to a large extent in all three directions by increasing the n, which also makes MD simulation computationally very expensive. So the long-range Coulomb interactions must be treated in a special way.

The standard way to treat the long-range Coulomb interactions in a periodic system is Ewald summation method [181]. The idea of Ewald summation method is to divide the slow decaying r_{ij}^{-1} term in the above Coulomb summation into two rapidly converging sums: one in real space and other one in reciprocal space, i.e.,

$$\begin{aligned} U_{\text{Coulomb}} &= \frac{1}{2}\sum_{i,j=1}^{N} q_i q_j \left\{ \sum_{\vec{a}} \frac{erfc\left[\kappa\left|\vec{r_{ij}}+\vec{a}\right|\right]}{\left|\vec{r_{ij}}+\vec{a}\right|} \right\} \\ &+\frac{2\pi}{V}\sum_{\vec{g}\neq 0} g^{-2} exp\left[-\frac{g^2}{4\kappa^2}\right] S(\vec{g})S(-\vec{g}) - \sum_{i=1}^{N} q_i^2 \frac{\kappa}{\sqrt{\pi}} \end{aligned} \tag{2.21}$$

$$S(\vec{g}) = \sum_{j} q_j exp(\vec{g}.\vec{r_j}) \tag{2.22}$$

Here the reciprocal space vector $\vec{g}$ and the real space vector $\vec{a}$ are defined via:

$$\vec{g} = n_x.\vec{g_x} \ + \ n_x.\vec{g_y} \ + \ n_x.\vec{g_z} \ \ and \ \vec{a} = n_x.\vec{a_x} \ + \ n_y.\vec{a_y} \ + \ n_z.\vec{a_z}$$

$$\vec{g_x} = \frac{2\pi}{V}\ \vec{a_y}\times\vec{a_z}, \ \ \vec{g_y} = \frac{2\pi}{V}\ \vec{a_z}\times\vec{a_x} \ and \ \vec{g_z} = \frac{2\pi}{V}\ \vec{a_x}\times\vec{a_y}$$

$$\vec{a_x} = \begin{bmatrix} L_x \\ 0 \\ 0 \end{bmatrix}, \ \vec{a_y} = \begin{bmatrix} 0 \\ L_y \\ 0 \end{bmatrix}, \ \vec{a_z} = \begin{bmatrix} 0 \\ 0 \\ L_z \end{bmatrix}$$

where κ is Ewald convergence parameter, S($\vec{g}$) is the structure factor and V is the volume of the simulation box. The last term in the equation 2.21 is the self-energy correction term. Even thought the Ewald summation converges more rapidly than the equation 2.20, for very larger systems, it is still computationally expensive to calculate because of its $\mathcal{O}(N^2)$ scaling.

For larger systems, the reciprocal space summation in Ewald summation is modified by several methods [182–186] in order to reduce the scaling. Among those methods, smooth particle mesh Ewald summation method [182,184] is one of widely used method to efficiently approximate the reciprocal space summation with an improved $\mathcal{O}(N \log N)$ scaling. The method uses spline interpolation for exponential term and 3D fast Fourier transformation for determining the reciprocal sum. This is achieved by approximating the structure factor term with,

$$\sum_j q_j exp(\vec{g}.\vec{r_j}) \approx b_1(g_1)b_2(g_2)b_3(g_3)F(Q)(g_1,g_2,g_3) \tag{2.23}$$

where $b_i(g_i)$ are cardinal B-splines, $F(Q)$ is the discrete Fourier transform of the 3D matrix Q of dimension $K_1 \times K_2 \times K_3$. The approximate reciprocal energy term can be re-expressed as the convolution,

$$\frac{2\pi}{V}\sum_{\vec{g}\neq 0} g^{-2} exp\left[-\frac{g^2}{4\kappa^2}\right] S(\vec{g})S(-\vec{g}) \approx \frac{1}{2}\sum_{k_\alpha=o}^{K_\alpha-1} Q(g_1,g_2,g_3) \times (\theta_{rec} * Q)(g_1,g_2,g_3) \tag{2.24}$$

where $\theta_{rec} = F(B \times C)$ and B, C are given by

$$B(g_1,g_2,g_3) = \prod_{i=1}^{3} |b_i(g_i)|^2 \tag{2.25}$$

$$C(g_1,g_2,g_3) = \frac{1}{\pi V} g^{-2} exp\left[-\pi\frac{g^2}{\kappa^2}\right] \tag{2.26}$$

The detailed expression of the $b_i(g_i)$ and $F(Q)$ can be found in refs [182,184].

2.1.4 Ensembles

Different types of thermodynamic ensembles can be used in MD, each of which is achieved by the control of certain thermodynamic quantities, thus making the system experiences distinct [106]. The popular ensembles are grand canonical (μVT), isothermal-isobaric (NPT), micro canonical (NVE) and canonical (NVT) ensembles [187,188]. The thermodynamic quantities in the brackets are held constant during their respective simulation [189]. In our simulations, we used the last two ensembles.

Micro canonical (NVE) ensemble: This ensemble represents a totally isolated system with constant energy. During a NVE ensemble based simulation, the quantities number of atoms, volume and energy are fixed constant, while the remaining quantities are permitted to fluctuate. As a result, the system goes via an adiabatic process with no heat exchange.

Canonical (NVT) ensemble: In the NVT ensemble, the number of atoms, volume, and temperature are fixed constants, while the remaining parameters like as pressure and energy are allowed to change. The system is kept at a constant temperature by coupling it to an external thermal bath through a thermostat. In our NVT-based MD simulations, we used the Nosé-Hoover thermostat. The next part shortly explains how the Nosé-Hoover thermostat keeps a system at a constant temperature.

Nosé-Hoover thermostat

The Nosé-Hoover thermostat adds an additional degree of freedom to the Hamiltonian of the system for describing the heat bath, which can then be used to calculate the equations of motion [190]. This is accomplished by introducing a thermodynamic friction factor ξ, which regulates the movement of atoms until the temperature reaches the desired value. The chief advantage of this thermostat is that it provides a canonical ensemble with atomic pathways that are smooth and time reversible. The equation for Nosé-Hoover thermostat can be written as [190,191] ,

$$m_i \frac{d^2 r_i}{dt^2} = F_i - \xi m_i v_i \tag{2.27}$$

$$\frac{d\xi}{dt} = \frac{1}{Q}\left[\sum_i \frac{m_i v_i^2}{2} - X k_B T\right] \tag{2.28}$$

where $X = \frac{3N+1}{2}$ is the number of degrees of freedom in the system, ξ is the thermodynamic friction factor, T is the desired temperature and Q is the coupling term which controls the coupling to heat bath.

2.2 Energy decomposition analysis

Energy decomposition analysis based on absolutely localized molecular orbitals (ALMO-EDA)[192] is an *ab-initio* technique primarily used to determine the hydrogen bond (HB) strength, charge-transfer and ion-water interaction energies in aqueous systems[7,31–34,46]. The technique proceeds by first filtering out frozen electrostatic and polarization effects from the total many-body intermolecular binding energy, and then splitting the remaining electron transfer (i.e. covalent) component into two-body terms, $\triangle E_{DEL}$, each corresponding to an individual HB[31,32]. These two-body terms are obtained self-consistently under fully periodic boundary conditions and include cooperativity effects. The average HB strength of a system can be calculated by summing all the energies of HB interactions and dividing the sum by the total number of HBs,

$$\triangle E^{\text{tot}} = \sum_{i}^{N^{\text{HB}}} \triangle E_i \tag{2.29}$$

where N^{HB} is the total number of HBs in the system. Furthermore, the asymmetry between the two strongest HB donor interactions involving a particular water molecule can also be calculated by a dimensionless asymmetry parameter,

$$\gamma_{\text{D}} = 1 - \frac{\triangle E_{A \rightarrow B^{2nd}}}{\triangle E_{A \rightarrow B^{1st}}} \tag{2.30}$$

where the $\triangle E$ terms are the two strongest two-body donor (involving charge transfer from molecule A to B) interaction energies. A similar asymmetry parameter for acceptor interactions γ_A can also defined from the two strongest two-body acceptor. In liquid water under ambient conditions, the joint distribution of γ_A and γ_D found that there is a significant population of water molecules with both parameters close to unity[31,32,193]. The detailed description of the ALMO-EDA methodology can be found in the ref[192].

2.3 Auto- and cross-correlation functions of linear and angular velocities

The rotation-translation coupled motion, in other words, the kinetic energy transfer from rotation motion to translation motion in a water molecule or between two H-bonded water molecules can be probed by computing the cross-correlation functions[194–204] between the linear (Centre of Mass, COM) and angular velocities of the individual water molecules or of two H-bonded water molecules in aqueous systems. The cross-correlation function between COM and angular velocities of a water molecule is referred as intramolecular rotation-translation coupling cross-correlation function, while those between COM and angular velocities of two H-bonded water molecules is referred as intermolecular rotation-translation coupling cross-correlation function. Both the intramolecular and intermolecular cross-correlation functions are tensors with nine components that can be computed on both the Cartesian and molecular axes[194,205]. The intramolecular and intermolecular rotation-translation coupling cross-correlation functions are typically written as[194,198–200,204],

$$\text{Intramolecular rotation-translation coupling CCF} = \frac{< \omega_{i,\alpha}(0) \cdot v_{\text{COM},i,\beta}(t) >}{< \left|\omega_{i,\alpha}(0)\right| \cdot \left|v_{\text{COM},i,\beta}(0)\right| >} \tag{2.31}$$

$$\text{Intermolecular rotation-translation coupling CCF} = \frac{< \omega_{i,\alpha}(0) \cdot v_{\text{COM},k,\beta}(t) >}{< \left|\omega_{i,\alpha}(0)\right| \cdot \left|v_{\text{COM},k,\beta}(0)\right| >} \tag{2.32}$$

where α, β are the x, y, and z directional components, ω_i and $v_{\mathrm{COM},i}$ are the COM and angular velocities of water molecule i, which can be obtained by the following equations:

$$\vec{v}_{\mathrm{COM},i} = \sum_{j=1}^{3} \frac{m_j}{M_i}.\vec{v}_j \tag{2.33}$$

$$\vec{\omega}_i = \sum_{j=1}^{3} \frac{\vec{r}_j \times \vec{v}_j}{|\vec{r}_j|^2} \tag{2.34}$$

$$\vec{r}_{\mathrm{COM},i} = \sum_{j=1}^{3} \frac{m_j}{M_i}.\vec{r}_j \qquad and \qquad M_i = \sum_{j=1}^{3} m_j \tag{2.35}$$

where M_i is the mass of water molecule i, $\vec{r}_j$ and $\vec{v}_j$ are the position and velocity of atom j, respectively. The latter two are subtracted with their COM position and COM velocity in order to shift them to molecular axis system [194]. The $|\vec{r}_j|^2$ is introduced in angular velocity calculations to bring the unit to $\frac{1}{time}$ [194]. Note that here the j represents the atoms and the i, k represent the molecules.

The auto-correlation functions of COM and angular velocities, of individual water molecules (intramolecular) and of two H-bonded water molecules (intermolecular), can be written as,

$$\text{Intramolecular COM velocity ACF} = \frac{<\vec{v}_{\mathrm{COM},i}(0)\cdot\vec{v}_{\mathrm{COM},i}(t)>}{<\vec{v}_{\mathrm{COM},i}(0)\cdot\vec{v}_{\mathrm{COM},i}(0)>} \tag{2.36}$$

$$\text{Intramolecular angular velocity ACF} = \frac{<\vec{\omega}_i(0)\cdot\vec{\omega}_i(t)>}{<\vec{\omega}_i(0)\cdot\vec{\omega}_i(0)>} \tag{2.37}$$

$$\text{Intermolecular COM velocity ACF} = \frac{<\vec{v}_{\mathrm{COM},i}(0)\cdot\vec{v}_{\mathrm{COM},k}(t)>}{<\vec{v}_{\mathrm{COM},i}(0)\cdot\vec{v}_{\mathrm{COM},k}(0)>} \tag{2.38}$$

$$\text{Intermolecular angular velocity ACF} = \frac{<\vec{\omega}_i(0)\cdot\vec{\omega}_k(t)>}{<\vec{\omega}_i(0)\cdot\vec{\omega}_k(0)>} \tag{2.39}$$

Evans is a pioneer in the study of cross-correlation functions for rotation-translation coupling [195–204].

The $<\vec{v}(0)\cdot\vec{v}(t)>$, $<\vec{\omega}(0)\cdot\vec{\omega}(t)>$ and $<\vec{v}_{\mathrm{COM}}(0)\cdot\vec{v}_{\mathrm{COM}}(t)>$ auto-correlation functions can be Fourier transformed to produce the power, rotational and translational spectra, as the following equation:

$$\text{Power spectra } (\omega) = \int_0^\infty dt\ e^{-i\omega t} \times \left\langle \sum_{i=1}^{N} <\vec{v}(0)\cdot\vec{v}(t)> \right\rangle \tag{2.40}$$

$$\text{Rotational spectra } (\omega) = \int_0^\infty dt\ e^{-i\omega t} \times \left\langle \sum_{i=1}^{N} <\vec{\omega}(0)\cdot\vec{\omega}(t)> \right\rangle \tag{2.41}$$

$$\text{Translational spectra } (\omega) = \int_0^\infty dt\ e^{-i\omega t} \times \left\langle \sum_{i=1}^{N} <\vec{v}_{\mathrm{COM}}(0)\cdot\vec{v}_{\mathrm{COM}}(t)> \right\rangle \tag{2.42}$$

Hann window function can be applied to the Fourier transformation of the TCF [58].

2.4 Kinetic energy decomposition

In our investigations, the kinetic energy (KE) of water is decomposed solely into translational and rotational kinetic energies , assuming that the covalent bonds within the water molecules are rigid as well as the THz pulse only has a modest impact on vibrational motions [206]. The translational KE of a water molecule is calculated as,

$$KE_{\text{trans}} = \frac{m_{\text{COM}} v_{\text{COM}}^2}{\sum_{j=1}^{3} m_i.v_i^2} \tag{2.43}$$

where m_i is the mass of atom i, m_{COM} is center of mass of a water molecule, v_i is the velocity of atom i and v_{COM} is the velocity of center of mass of a water. whereas the rotational KE is determined by calculating the difference between translational and total kinetic energies,

$$KE_{\text{rot}} = \frac{1}{2} \sum_{i=1}^{3} m_i.v_i^2 - KE_{\text{trans}} \tag{2.44}$$

These calculation are done directly with the atomic velocities acquired from MD simulations. Note that the translation and rotational KE in this work is reported per molecule. This is done by adding up all the molecules' KE of interest and dividing it by the total number of molecules.

2.5 Pair correlation function

In statistical mechanics, the pair correlation or radial distribution function (RDF) is one of the most useful functions for describing the average structure and arrangement of atoms in a system [106]. It offers information about the bond distance, nearest neighbour distances and coordination numbers [207,208]. More importantly, the Fourier transform of the RDF yields the structure factor, which can be directly compared with the experimental measurements such as X-ray or Neutron scattering [106,209].

To compute RDF, we start with an MD frame and create a series of spherical shells around an atom with a thickness dr. Second, by counting the number of atoms in each shell at regular intervals, the average number of atoms in a shell is computed. Then the RDF is calculated by dividing the average number of atoms in a shell by the volume of each shell and its bulk number density. Mathematically, the $g(r)$ for a overall system can be calculated as

$$g(r) = \frac{N(r, dr)}{\rho 4\pi r^2 dr} \tag{2.45}$$

where $N(r, dr)$ is the number of atoms in shell of radius r, thickness dr, and $\rho = \frac{N}{V}$ is the bulk number density. $4\pi r^2 dr$ is the shell volume. The procedure is then repeated for all all the atoms in the frame and for all MD frames, until the statistical convergence is reached.

The average structure and arrangement of two specific chemical species can also be described by slightly modifying the above RDF equation 2.45. For two specific chemical species α and β, the modified $g(r)$ equation is as follows,

$$g_{\alpha-\beta}(r) = \frac{N_{\alpha-\beta}(r, dr)}{\rho_\alpha 4\pi r^2 dr} \tag{2.46}$$

where $N_{\alpha-\beta}(r, dr)$ is the number of α-atoms in shell of radius r from the β-atom and $\rho_\alpha = \frac{N_\alpha}{V}$ is the number density of α-atoms.

2.6 Modeling of collective polarizability anisotropy

In this work, we use the polarizability anisotropy definition from the simple model, derived by Tobias and co-workers [69], for the terahertz kerr effect process. They have defined the polarizability anisotropy as the difference $\triangle\alpha = \alpha_{zz} - \frac{(\alpha_{xx}+\alpha_{yy})}{2}$ between polarizability in directions, parallel (z-axis) and perpendicular (x- and y-axes) to the applied THz field. The advantage of this definition is that it is signed and allowed simulated polarizability anisotropies [44,114] to compare directly with the experimentally measured birefringence measurements.

Since in this work the field is applied in x direction, the polarizability anisotropy has been written as the difference between the total polarizability of xx-component and the average of remaining two diagonal components, yy and zz:

$$\triangle\alpha = \alpha_{xx} - \left[\frac{\alpha_{yy} + \alpha_{zz}}{2}\right] \tag{2.47}$$

The total polarizability of each component can be calculated by summing the permanent (α^{perm}) and induced (α^{ind}) polarizabilites of all the molecules in the system:

$$\alpha_{\text{total}} = \sum_{i=1}^{n} (\alpha_i^{\text{perm}} + \alpha_i^{\text{ind}}) \tag{2.48}$$

where n is the total number of molecules. The ionic polarizability parameters in the polarizable force fields [159,173,210,211] were chosen to treat the permanent polarizabilites of the ions. Whereas the permanent polarizabilites of water were calculated in the gas phase conditions using the polarizability parameters in Table 3.1. Unlike coupled cluster single double polarizability parameters [212–214], which are isotropic, our polarizability parameters are anisotropic as Huiszoon polarizability parameters [215].

The induced polarizability of each molecule is calculated via the dipole-induced-dipole (DID) model by including up to second-order molecular hyperpolarizability terms, and the calculation was evaluated by the self-consistent field (SCF) procdeure. The following expression provide general SCF equations for classical DID model [52,61,85–91] neglecting higher order terms and extended higher-order DID models [95–101] with the inclusion of effects between local electric field and first- and second-order molecular hyperpolarizabilities:

$$\text{Simple DID model} : \alpha_i^{\text{ind}} = \alpha_i^{\text{perm}} \sum_{j!=i}^{n} T_{ij}(\alpha_j^{\text{perm}} + \alpha_j^{\text{ind}}) \tag{2.49}$$

$$\text{First–order extended DID}^1 \text{ model} : \alpha_i^{\text{ind}} = \alpha_i^{\text{perm}} \sum_{j!=i}^{n} T_{ij}(\alpha_j^{\text{perm}} + \alpha_j^{\text{ind}}) + \beta_i \vec{E}_i \tag{2.50}$$

$$\text{First- and second-order extended DID}^{1,2} \text{ model} : \alpha_i^{\text{ind}} = \alpha_i^{\text{perm}} \sum_{j\neq i}^{n} T_{ij}\left(\alpha_j^{\text{perm}} + \alpha_j^{\text{ind}}\right) + \beta_i \mathbf{E}_i + \frac{\mathbf{E}_i \cdot \gamma_i \cdot \mathbf{E}_i}{2} \tag{2.51}$$

where $T_{ij} = 3\vec{r}_{ij}\vec{r}_{ij}^{T}/r_{ij}^5 - I/r_{ij}^3$ is the standard dipole-dipole interaction tensor [85,86] between molecules i and j, $\vec{r}_{ij}$ and r_{ij} are the distance vector and norm distance from molecule i to j, I is a 3×3 unit tensor, β_i and γ_i are the first and second hyperpolarizability tensors of molecule i, which are calculated in gas phase conditions using our parameters in Table 3.1. Here $\vec{E}_i$ is the local electric field vector at molecule i created only by all the surrounding molecules ((i.e., the permanent ionic charges and the permanent and induced dipoles of all entities but excluding the external THz field)) up to a certain specified cutoff distance r_t. To include the field from long-range interactions greater than half of the simulation box length, we have employed the replica method [174,175], which replicates the original simulation box in all the directions. Even though this method is computationally expensive than the Ewald summation [216,217], we employ it in this work because for the purpose at hand it is very easy to implement and overall simpler than the Ewald summation. The SCF equations are solved iteratively until the solution reaches the tolerance of 0.000001 Å^3. Thole exponential damping function [85,86] is employed throughout to avoid the "polarization catastrophe" when molecules are very closer. The correction parameters in the damping function are updated between SCF iterations in order to improve the accuracy of polarizability anisotropy results as suggested by an earlier work [88].

2.7 Modeling of permanent and induced dipole moments

The permanent dipole moment of ions is set to zero, while for water, gas phase dipole moment of $\sim$ 1.9 Debye is assigned to their bisector direction.

The induced dipole moment of each molecule is obtained by solving the standard dipole linear equation

$$(\frac{1}{\alpha^{\text{perm}}} + T)\boldsymbol{\mu}^{\text{ind}} = \mathbf{E} \tag{2.52}$$

via the preconditioned conjugate gradient method [174–179] with the convergence tolerance 0.000001 Debye and with the following initial guess, residue and direction:

$$\text{Initial guess:} \quad \boldsymbol{\mu}_i^{\text{ind},0} = \alpha_i^{\text{perm}} [\mathbf{E}_{\text{external}} + \mathbf{E}_i] \tag{2.53}$$

$$= \alpha_i^{\text{perm}} \left[\mathbf{E}_{\text{external}} + \sum_{j \neq i}^{n} \frac{q\, \hat{\mathbf{r}}_{ij}}{r_{ij}^2} - \sum_{j \neq i}^{n} \frac{1}{r_{ij}^3} \boldsymbol{\mu_j}^{\text{perm}} + \sum_{j \neq i}^{n} \frac{3}{r_{ij}^5} (\mathbf{r_{ij}} \cdot \boldsymbol{\mu_j}^{\text{perm}}) \mathbf{r_{ij}} \right] \tag{2.54}$$

$$\text{Initial residue:} \quad \mathbf{r}_i^0 = \sum_{j \neq i}^{n} T_{ij}\, \boldsymbol{\mu}_j^{\text{ind},0} \tag{2.55}$$

$$\text{Initial direction:} \quad \mathbf{p}_i^0 = \alpha_i^{\text{perm}}\, \boldsymbol{r}_i^0 \tag{2.56}$$

where $\hat{r}_{ij}$ is the unit vector pointing from molecule i to j, q is the molecular charge and $\mathbf{E}_{\text{external}}$ is externally applied field vector. $\mathbf{E}_{\text{i}}$ is the local or microscopic field at molecule i due to all surrounding molecules.

Chapter 3

Computational details

In this chapter, the types and parameter specifics of MD simulations employed in this thesis work are presented. Moreover, we also present the calculation details for all theoretical frameworks used in this work, including ALMO-EDA, correlation functions, polarizability anisotropies, definitions of HBs, and solvation shells.

Molecular Dynamics

We have performed three different types of MD simulations (DFT-based ab initio MD, polarizable force field MD, and non-polarizable force field MD). Simulations were performed on aqueous salt systems: pure liquid water (as reference), $MgCl_2$ (1M, 2M and 4M), Na_2SO_4 (1M), $MgSO_4$ (2M), $NaCl_2$ (2M and 4M) and NaF (1M). All simulations were performed under the microcanonical ensemble with constant energy, volume, and number of particles. All initial configurations were uniformly sampled from equilibrated constant temperature (canonical ensemble) MD simulations. Table 3.3 lists the details of the simulated systems. All simulations were performed under fully periodic boundary conditions. The time step was set to 0.4 fs, and double precision floating point was always used. A THz electric field pulse identical to the one used in the time-resolved TKE experiments of Mohsen and Vasileios [44,121] was applied in the x-direction. In order to improve the signal-to-noise ratio we have used two pulses with amplitudes that are three times stronger for DFT-based ab initio MD simulations and eight times stronger for polarizable force field MD, and non-polarizable force field MD simulations. Figure 9.1 shows employed pulse in atomic unit. The MD trajectory data are printed at every 80 time step. Further details specific for each MD technique are given below:

Polarizable force field MD: Simulations were performed using the TINKER software [174,175]. The Velocity-Verlet algorithm was employed to time-propagate the positions and velocities of atoms. The amoeba force field parameter set 'amoebanuc17' was used [158–161]. For SO_4^{2-} ion, the parameters were taken from the refs [169,218] and for CO_3^{2-} ion the parameters were taken from refs [219]. Buffered 14-7 potential [170] was used to include the effects of short-range repulsion-dispersion interaction. Short range interactions were truncated at 9 Å, whereas the smooth particle mesh Ewald [182] was employed to treat the long-range electrostatic interactions. The mutual induced dipoles were computed using the conjugate gradients method [178,179] with a tolerance of 0.00001 Debye. For modeling of the external electric field in TINKER, we have implemented the electric force term $F = k_1\ q\ E$ and induced dipole term $\mu = k_2\ \alpha\ E$ in the energy and force calculations. The units conversion factors $k_1 = 1185.85$ and $k_2 = 3.567$ give the forces and dipoles in kcal per Å per mol and $Å^2$, when the electric field E and polarizability α are in atomic unit and $Å^3$. The existing implementation of conjugate gradients minimization in TINKER was utilized to compute the mutual induced dipoles that produce the local field at each molecule.

Non-polarizable force field MD: Simulations were carried out using GROMACS 2020.4 software [220] with the rigid three point (SPC/E) water model [147,148] and the AMBER force field parameters [135–137] for the ions. The Verlet leap-frog algorithm [221] was employed to evolve the position and velocities of atoms. Long-range electrostatic interactions were computed using a smooth particle mesh Ewald summation [182] with a real-space cutoff less than half of the simulation box length, while Lennard-Jones interactions [180] were computed using a shifted potential such that they are zero at the same cut-off distance. LINCS algorithm [222] was used to keep water molecules rigid.

Ab initio MD: Simulations were conducted using the Quickstep module of the CP2K software [104,223]. The energies and forces were computed using the mixed Gaussian-plane waves (GPW) approach [224], with the Kohn–Sham orbitals represented by an accurate triple-ζ basis set with two sets of polarization functions (TZV2P) [225]. Plane-waves with a cutoff of 400 Ry were used to represent the charge density, whereas the core electrons were described by the Goedecker-Teter-Hutter (GTH) pseudopotentials. The BLYP exchange-correlation functional was used together with a damped interatomic potential for dispersion interactions (Grimme-D3) [226]. The Berry-phase approach [227,228] was employed for the proper description of the electric field under periodic boundary conditions.

THz pulse details: We have employed a single-cycle THz electric pulse in our MD simulations with a maximum field strength of $\sim 10^9$ V/m and a frequency of ~ 1 THz (1 ps) [44,121].

Energy decomposition analysis

All ALMO-EDA calculations in this work were performed using the ALMO-EDA implementation in CP2K program [104,223] with same settings as described in our AIMD simulations. ALMO's technical specifics are detailed elsewhere [192]. Configurations for ALMO-EDA were obtained from AIMD simulations under field-free conditions for pure liquid water (as a reference), and for $MgCl_2$ (2M), Na_2SO_4 (1M) and $MgSO_4$ (2M). The systems were initially equilibrated in the canonical ensemble for 40 ps, followed by a production run in the microcanonical ensemble for 50 ps. For each system, ALMO EDA was performed for 500 AIMD snapshots uniformly sampled from the 50 ps well equlibrated trajectories.

DID mechanism

The polarizability anisotropy reported in this work were calculated mostly using the program [229] developed by me. The ionic polarizability parameters in the polarizable force fields [159,173,210,211] were chosen to treat the permanent polarizabilites of the ions, as show in Table 3.2. Whereas the permanent polarizabilites of water were calculated in the gas phase conditions. The induced polarizability of each molecule is computed by using three different DID mechanisms (simple DID, [52,61,85–92], DID^1 [95–101], and $DID^{1,2}$) solved in SCF approach. To include the field from long-range interactions greater than half of the simulation box length, we have employed the replica method [174,175], which replicates the original simulation box in all the directions. The SCF equations were solved iteratively until the solution reaches the tolerance of 0.000001 $Å^3$. Thole exponential damping function [85,86] is employed and the correction parameters in the damping function are updated between SCF iterations. The time-dependent polarizability anisotropy results reported in this work were averaged over 90000 trajectories.

Parameterization of dipole moment, polarizability, and hyperpolarizabilities

The permanent dipole moment of the ions was set to zero, while for water, a gas phase dipole moment of $\sim$ 1.90 Debye was assigned along the molecular bisector. The ionic polarizability parameters from the Ref[173,210] were used to model the permanent polarizabilites of the ions. Whereas the permanent polarizabilites of water were calculated in the gas phase. All the employed parameters for water are listed in Table 3.1.

The values of dipole moment and polarizability parameters of gas phase water reported in this work were parameterized using CP2K program[77,104], while the first and second hyperpolarizability parameters of gas phase water were parameterized using DALTON program[230]. For this parameterization, we used the same settings as described in our DFT based AIMD simulations. Note also that a quadratic response function[231,232] is used for the first hyperpolarizability parameterization, while a cubic response function[233,234] is used for the second hyperpolarizability parameterization. We calculated all these parameters in the gas phase using 2000 AIMD condensed water, and we utilized the mean value in our work.

Hydrogen bond and solvation shell definitions

Throughout, we have used the standard hydrogen bond definition of Luzar and Chandler[235] (O-O distance $<$ 3.5 Å and an hydrogen bond angle $<$ 30 Degree). In addition, the first minimum in the radial distribution function between ion and center of mass of water is used to define the radius of the ionic solvation shell[52].

Intramolecular and intermolecular auto- and cross-correlation functions

The intramolecular and intermoelcular auto- and cross-correlation functions reported in this work were calculated using the program[229] developed by me. The components of the cross-correlation functions are displayed in both Cartesian axis and principal axis system. The reported correlation function results functions were averaged over 40000 SPC pure liquid water MD trajectories, under field-on and field-free conditions. The correlation function used for averaging were sampled every 100 fs. Throughout a window length of 0.8 ps was employed during which the set water molecules were kept fixed for intermolecular coupling.

The principal axis system (also called molecular axis system) is transformed from the Cartesian coordinate axis system using the rotation matrix, which basically contains the components of three unit vectors representing the principal axis system[194]. In the principal axis system of our water molecule, the x-axis belongs to the vector uniting the two hydrogen atoms (H-H vector), y-axis to the vector of water bisector and the z-axis to the vector perpendicular to both water bisector and H-H vector.

Table 3.1: Parameterized molecular dipole moment, polarizabilites, first and second order hyperpolarizabilites of a gas phase water. Note that in the molecular frame of our gas phase water molecule, the x-axis belongs to the vector uniting the two hydrogen atoms (H-H vector), y-axis to the vector of water bisector and the z-axis to the vector perpendicular to both water bisector and H-H vector. Here a.u. means atomic unit.

Properties	H_2O parameters	Units
Dipole		
μ_y	1.93 (0.759)	Debye (a.u.)
Polarizability		
α_{xx}	1.3725 (9.2713)	$Å^3$ (a.u.)
α_{yy}	1.1580 (7.8224)	$Å^3$ (a.u.)
α_{zz}	0.9127 (6.1653)	$Å^3$ (a.u.)
First hyperpolarizability		
β_{yyy}	-0.5282 (-12.730)	$Å^5$ (a.u.)
β_{xxy}	-0.6824 (-16.445)	$Å^5$ (a.u.)
β_{zzy}	-0.2297 (-5.5365)	$Å^5$ (a.u.)
Second hyperpolarizability		
γ_{xxxx}	3.1351 (269.8054)	$Å^7$ (a.u.)
γ_{yyyy}	1.470 (126.5123)	$Å^7$ (a.u.)
γ_{zzzz}	0.09407 (8.096200)	$Å^7$ (a.u.)
γ_{xxyy}	2.1019 (180.8921)	$Å^7$ (a.u.)
γ_{xxzz}	1.0817 (93.09720)	$Å^7$ (a.u.)
γ_{yyxx}	2.1019 (180.8921)	$Å^7$ (a.u.)
γ_{yyzz}	0.4124 (35.49410)	$Å^7$ (a.u.)
γ_{zzxx}	1.0817 (93.09720)	$Å^7$ (a.u.)
γ_{zzyy}	0.4124 (35.49410)	$Å^7$ (a.u.)

Table 3.2: Screening length, Van der Waals Radius and parameterized isotropic polarizability of ions.

Ion	α ($Å^3$) [159,173,210,211]	Screening length [174–177]	Van der Waals Radius [236,237]
Mg^{2+}	0.08	0.1150	1.364
Na^+	0.12	0.3900	2.27
Cl^-	4	0.3900	1.639
F^-	1.35	0.3900	1.47
SO_4^{2-}	7	0.3900	1.47
H_2O	above table	0.3900	1.7

Table 3.3: Simulated systems with their concentration, proportion and box length. AIMD=ab initio MD, PFFMD=polarizable force field MD, FFMD=non-polarizable force field MD. The number of independent simulated trajectories of each kind is given between square brackets.

Solution	Conc. (mol/L)	No. of ions	No. of H2O	Box length in Å	MD kind
Liquid water	-	-	128	15.64	AIMD[400], PFFMD [90K], FFMD [150K]
$MgCl_2$	1	2	125	15.57	PFFMD [90K], FFMD [150K]
$MgCl_2$	2	5	121	15.62	AIMD[400], PFFMD [90K], FFMD [150K]
$MgCl_2$	4	8	101	15.00	PFFMD [90K], FFMD [150K]
Na_2SO_4	1	2	125	15.56	AIMD[400], PFFMD [90K], FFMD [150K]
$MgSO_4$	2	5	125	15.72	AIMD[400]
NaCl	2	5	108	15.07	PFFMD [90K]
NaCl	4	8	104	15.00	PFFMD [90K]
NaF	1	3	137	16.09	PFFMD [57K]

Chapter 4

Simulating bulk polarizability of aqueous salt solutions with non-equilibrium molecular dynamics and a multipolar expansion

In this chapter, we derived the hyperpolarizability extended DID formalism for calculating the THz-induced polarizability anisotropy of aqueous salt solutions. We further show that the DID formalism can be used to accurately reproduce the experimental TKE birefringence measurements as well as the polarization and polarizability calculated from first-principle approaches.

4.1 Polarization and Polarizability : At Molecular Level

The electric field interactions with molecules in a condensed matter will have their nuclei's positions changed and electron density (polarization) displaced. The magnitude and direction of the nuclear position displacement depends on the strength and sign of the electric field, as described by the electric force (= charges × electric field). Whereas the magnitude of polarization depends on the displacement of electron density to keep up with the oscillation of the electric field [238]. Such changes have a variety of effects on the structure and dynamics of molecules, including bond stretching, bond alignment, molecular reorientation, electron cloud redistribution and many other effects [238], which actually alter the molecules' characteristics.

Dipole moment and polarizability are two terms that are commonly used to describe how molecules interact with electric fields. To understand both of them, we use the familiar Multipolar expansion [239], which defines the electric potential $\varphi(\vec{r})$ of a polarizable charge distribution. The starting point is to Taylor expand the external electric potential around an origin, taken to be the center of the molecular charge distribution. as shown in Figure 4.1:

$$\begin{aligned}\varphi(\vec{r}) &= \varphi(0) - r_\alpha \left.\frac{\partial\varphi}{\partial r_a}\right|_{\vec{r}=0} - \frac{1}{2!} r_\alpha r_\beta \left.\frac{\partial^2\varphi}{\partial r_a \partial r_\beta}\right|_{\vec{r}=0} - \frac{1}{3!} r_\alpha r_\beta r_\gamma \left.\frac{\partial^3\varphi}{\partial r_a \partial r_\beta \partial r_\gamma}\right|_{\vec{r}=0} - \cdots \qquad (\alpha,\beta,\ldots = x,y,z) \\ &= \varphi(0) - r_\alpha E_\alpha(0) - \frac{1}{2!} r_\alpha r_\beta E_{\alpha\beta}(0) - \frac{1}{3!} r_\alpha r_\beta r_\gamma E_{\alpha\beta\gamma}(0) - \cdots, \end{aligned} \tag{4.1}$$

Here the Einstein summation being implied. In this section, the potential and all its gradients will

always be taken at the origin of the charge distribution under discussion, and we drop from the notation the explicit dependence on position, i.e. $E_{\alpha\beta\ldots} = E_{\alpha\beta\ldots}(0)$.

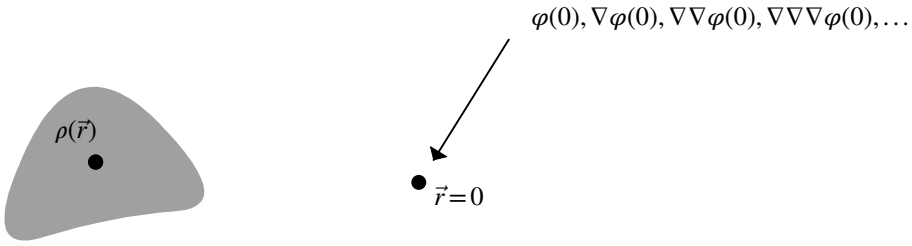

Figure 4.1: a) Molecular charge distribution. b) Taylor expansion of electric potential around an origin.

The interaction energy ΔU between the charge distribution and the external potential can now be written as the integration of electron density and electric potential in space:

$$\begin{aligned} \Delta U &= \int_V \mathrm{d}\vec{r}\rho(\vec{r})\varphi(\vec{r}) \\ &= q\varphi(0) - \mu_\alpha E_\alpha - \frac{1}{2}Q_{\alpha\beta}E_{\alpha\beta} - \frac{1}{6}R_{\alpha\beta\gamma}E_{\alpha\beta\gamma} - \cdots, \end{aligned} \tag{4.2}$$

where q, μ, Q, R etc are the charge distribution's monopole, dipole, quadrupole, and octopole. We stress here that all these quantities are not the quantities at zero external field, but are taken at a finite external field and hence can include induced contributions:

$$\mu_\alpha = \mu_\alpha^0 + \mu_\alpha^{ind}, \qquad Q_{\alpha\beta} = Q_{\alpha\beta}^0 + Q_{\alpha\beta}^{ind}, \qquad \text{etc.}$$

In order to relate the values of the perturbed expansion coefficients in Eq. (4.2) to their zero-field values, the interaction energy is expanded as a Taylor series in the field and all its derivatives:

$$\begin{aligned} \Delta U &= \Delta U(\varphi, \nabla\varphi, \nabla\nabla\varphi, \ldots)|_{\varphi=0} \\ &= -q\varphi(0) - \left(\left.\frac{\partial U}{\partial E_\alpha}\right|_{\varphi=0} E_\alpha + \left.\frac{\partial U}{\partial E_{\alpha\beta}}\right|_{\varphi=0} E_{\alpha\beta} + \left.\frac{\partial U}{\partial E_{\alpha\beta\gamma}}\right|_{\varphi=0} E_{\alpha\beta\gamma} + \cdots \right) \\ &\quad -\frac{1}{2}\left(\left.\frac{\partial^2 U}{\partial E_\alpha \partial E_\beta}\right|_{\varphi=0} E_\alpha E_\beta + \left.\frac{\partial^2 U}{\partial E_\alpha \partial E_{\beta\gamma}}\right|_{\varphi=0} E_\alpha E_{\beta\gamma} + \left.\frac{\partial^2 U}{\partial E_{\alpha\beta} \partial E_{\gamma\delta}}\right|_{\varphi=0} E_{\alpha\beta} E_{\gamma\delta} + \cdots \right) \\ &\quad -\frac{1}{6}\left(\left.\frac{\partial^3 U}{\partial E_\alpha \partial E_\beta \partial E_\gamma}\right|_{\varphi=0} E_\alpha E_\beta E_\gamma + \left.\frac{\partial^3 U}{\partial E_\alpha \partial E_\beta \partial E_{\gamma\delta}}\right|_{\varphi=0} E_\alpha E_\beta E_{\gamma\delta} + \cdots \right) - \cdots. \end{aligned} \tag{4.3}$$

The values of the perturbed expansion coefficients in Eq. 4.2 can then be obtained by differentiating the Taylor series in Eq. (4.3).

For the molecular dipole one obtains:

$$\begin{aligned} \mu_\alpha &= -\frac{\partial \Delta U}{\partial E_\alpha} \\ &= \left.\frac{\partial U}{\partial E_\alpha}\right|_{\varphi=0} + \left.\frac{\partial^2 U}{\partial E_\alpha \partial E_\beta}\right|_{\varphi=0} E_\beta + \frac{1}{2}\left.\frac{\partial^3 U}{\partial E_\alpha \partial E_\beta \partial E_\gamma}\right|_{\varphi=0} E_\beta E_\gamma + \frac{1}{2}\left.\frac{\partial^2 U}{\partial E_\alpha \partial E_{\beta\gamma}}\right|_{\varphi=0} E_{\beta\gamma} \\ &\quad + \frac{1}{2}\left.\frac{\partial^3 U}{\partial E_\alpha \partial E_\beta \partial E_{\gamma\delta}}\right|_{\varphi=0} E_\beta E_{\gamma\delta} + \cdots. \end{aligned} \tag{4.4}$$

The first term on the right-hand side is the permanent dipole moment, followed by the zero-field polarizability α^0, followed by higher-order polarizabilities: the first hyperpolarizability, dipole-quadrupole

polarizability, dipole-dipole-quadrupole polarizability etc. We emphasize that $\vec{\mu}$ in Eq. (4.4) is the dipole moment of the polarized charge distrbution, given in terms of zero-field parameters and the external field and field gradients acting at one point inside the charge distribution.

Thus by increasing the applied field $\vec{E} \to \vec{E} + \delta\vec{E}$ we have:

$$\begin{aligned}\delta u_\alpha &= \left(\alpha^0_{\alpha\beta} + \frac{\partial^2 U}{\partial E_\beta \partial E_\gamma}\bigg|_{\varphi=0} E_\gamma + \frac{1}{2}\frac{\partial^3 U}{\partial E_\beta \partial E_\gamma \partial E_\delta}\bigg|_{\varphi=0} E_\gamma E_\delta + \frac{1}{2}\frac{\partial^2 U}{\partial E_\beta \partial E_{\gamma\delta}}\bigg|_{\varphi=0} E_{\gamma\delta} + \cdots\right)\delta E_\beta \\ &= \Pi_{\alpha\beta}\delta E_\beta.\end{aligned}$$

This quantity represents the increase in the first moment of the charge distribution per unit increase in the applied external field. This only coincides with the moment-to-field ratio in the limit of vanishing external fields.

If one ignores the contributions of field gradients, then the quantity obtained was referred to by Buckingham as the 'differential polarizability'. Employing the Lorenz-Lorentz relation, in an ensemble of N non-interacting molecules, each represented by a polarizable charge distribution, the birefringence between two axes $e^{\parallel}$ and $e^{\perp}$ is obtained as:

$$n_\parallel - n_\perp = \frac{2\pi N}{V}\Pi_{\alpha\beta}(e^\parallel_\alpha e^\parallel_\beta - e^\perp_\alpha e^\perp_\beta).$$

In interacting systems, one still has to face the issue of the local field, that the actual field acting on each molecule is the superposition of the external field and the fields due to all the surrounding molecules.

Dipole moment : Eq. (4.4) describes how the electron density surrounding the nuclei is displaced as the field interacts with the charges q in the molecules. Classically, the induced dipole moment is written as

$$\mu_{induced} = \alpha E + \frac{\beta E^2}{2} + \frac{\gamma E^3}{6} + ... \tag{4.5}$$

where α is the zero-field polarizability tensor of a molecule and β, γ are the zero-field first and second hyperpolarizability tensors of a molecule, E contains both externally applied electric field and local electric field due to all surrounding molecules. The α provides the linear relation between μ and E, and associated with harmonic oscillation potential, while the higher order terms such as β, γ provide the non-linear relation, and associated with anharmonic potential well [238]. The first term αE is valid only for the weak electric fields, where the linear trends are observed. The terms beyond it are important to capture the non-linear effects at stronger electric fields.

It's essential to consider the fact that some molecules, such as water, methyl chloride, and etc, have a permanent dipole moments $\mu_{permanent}$ [240] because of the electronegativity variation among atoms in the molecule. The $\mu_{permanent}$ continue to persist even in the absence of both an externally applied electric field or a local electric field due to surrounding molecules. Hence, the total dipole moment μ_{total} exists and typically written as the sum of the permanent and induced dipole moments,

$$\mu_{total} = \mu_{permanent} + \mu_{induced} \tag{4.6}$$

Notably, the permanent and induced dipole moments are what lead to the bulk polarization at macroscopic level. The relationship between the bulk polarization P and the dipole moment μ of the N molecules per unit volume V is as $P = \frac{1}{V}\sum^N \mu$ [239]. The bulk polarization can thus be expressed as follows:

$$P = P_0 + \chi^{(1)}E + \chi^{(2)}E.E + \chi^{(3)}E.E.E \tag{4.7}$$

where $\chi^{(n)}$ are the nth-order nonlinear susceptibility, P_0 is the intrinsic dipole of the system, $\chi^{(1)}$ is the first-order susceptibility (second rank tensor) where describes the linear polarization with respect to the field. These macroscopic susceptibilities are analogous to the microscopic hyperpolarizabilities.

Local field correction: When an external field is applied to a condensed system, each of the molecules in the system experiences both macroscopic external electric field and microscopic or local electric field as a result of the molecules around it. The local field corrections [240] balance the distinct true local field experienced by each molecule, and consequently, each molecule won't have the same polarization and effective polarizability, hence the electronic transition and other essential effects are also considered. The true local field surrounding a molecule can be computed by simply solving the dipole and polarizability equations in a self-consistency field manner as earlier works [85,86,104].

Polarizability : The derivative of the dipole expression with respect to electric field gives the effective polarizability as:

$$\alpha^{\text{Effective}} = \alpha^0 + \beta^0 E + \frac{E \cdot \gamma^0 \cdot E}{2} + ... \tag{4.8}$$

Here E is only the local electric field due to all surrounding molecules. The complete expression to calculate the dipole moment and polarizability in SCF is given in equations 2.51 and 2.54 from the previous chapter 2.

4.2 Simulated dipole moment and polarizability

First, we have investigated the degree to which ionic charged particles and a THz electric field can polarize water. The term $\frac{q}{r^2}$ in principle can be used to describe the electric field produced by an ionic charge q at a distance r from the origin. We have calculated the electric field of Mg^{2+} and Na^{+} ions at various distances from the origin, and compared them with the peak field strength of THz pulse, this is shown in Figure 4.2. Ionic electric fields are $\sim$ 100 times more powerful than the employed THz electric fields. The first and second hydration waters experience ionic electric fields of $\sim$ 1 - 2 $\times$ 10^{11} $\frac{V}{m}$ and $\sim$ 0.5 - 1 $\times$ 10^{11} $\frac{V}{m}$, respectively.

We have also computed the dipole moment of water due to strongly charged cation (Mg^{2+}) at various distances from the water's COM, as shown in Figure 4.2. The moment exhibits classic Lennard-Jones-potential behavior [180]. At wider distances, only the permanent dipole moment of water ($\sim$ 1.9 Debye) is present; as the cation comes closer, the contribution of the induced dipole moment rises. Without Thole damping [85,86], the DID formalism strongly induces dipole moment and the SCF procedure fails to convergence. The polarization of water will be $\sim$ 100 times less induced by the THz electric field than by the ionic electric field.

Second, to assess the quality of the DID approach, we have computed the dipole moment and polarizability tensor of a small aqueous salt system using both DID[1,2] and first-principle [77] approaches, the results are shown in Figure 4.3. Only the x-directional dipole moment and the two polarizability tensor components have been shown. Visually, the quantities calculated from both the approaches are more comparable. Hence, the quantities determined from the DID approach can also be used to calculate the polarizability anisotropy, Raman and IR spectra of aqueous salt solutions since they fluctuate in the same way as those in the first-principle approach.

4.3 Simulated polarizability anisotropy

We have simulated the THz-electric-field-induced transient collective polarizability anisotropy of pure liquid water and several aqueous salt systems, via DID models, using polarizable and non-polarizable force field molecular dynamics (MD) trajectories. The MD trajectories were directly simulated with the effect of a single-cycle THz pulse used in the time-resolved TKE experiments of Mohsen and Vasileios [48,121], but with a 8 times stronger intensity to overcome statistical problems. Unfortunately, due to the computationally expensive nature of this problem, we are unable to use AIMD simulations

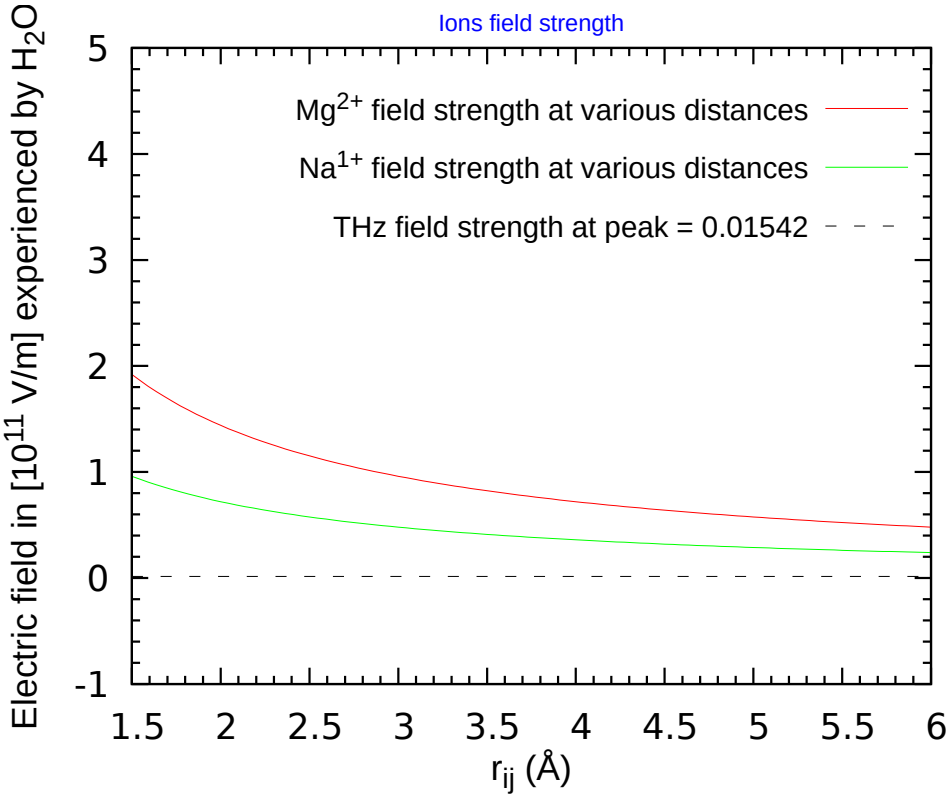

(a)

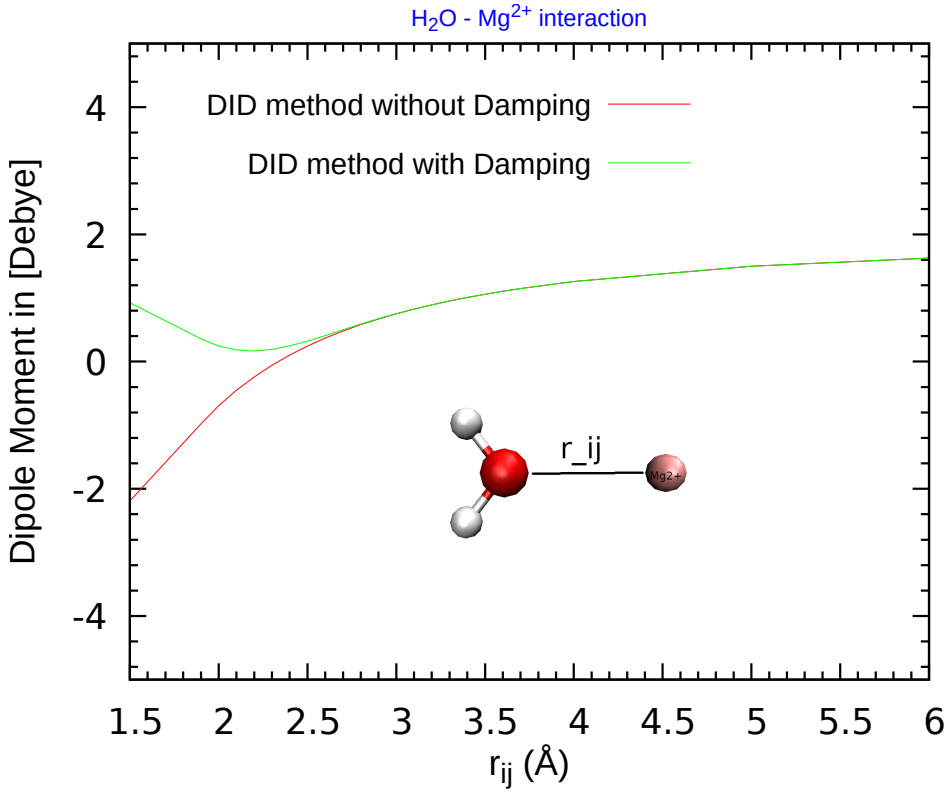

(b)

Figure 4.2: a) Ionic and THz pulse field strength in $\frac{V}{m}$ b) Dipole moment of water due to the strongly charged cation Mg^{2+} at various distances from the water's COM. The moment was calculated using DID formalism with and without Thole damping function.

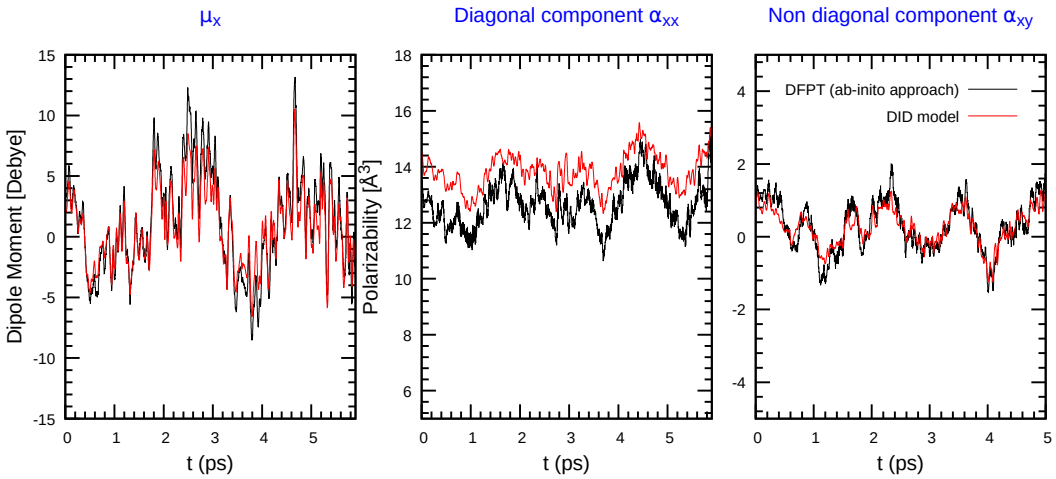

Figure 4.3: The time-varying dipole moment (only in the x-direction) and polarizability tensor (xx and xy components) of a small aqueous salt system (containing 5 H_2O and 1 $MgCl_2$) calculated via first-principle and DID approaches. Note that the small system was simulated using CP2K program with same settings as described in our equilibrium AIMD simulations (see Chapter 3).

or the first-principle polarizability calculation method. We have therefore compared the polarizatbility anisotropy of our simulations with experimental measurements directly.

4.3.1 Suitable cutoff for intermolecular collision-induced effects

We have first studied the impact of intermolecular collision-induced effects in the overall polarizability anisotropy of high salt concentrated aqueous solution and pure liquid water by varying r_t, from 3.5 to 15 Å, as shown in Figure 4.4. It can be clearly seen that the polarizability anisotropy of pure liquid water doesn't change with increase in the r_t from 3.5 Å. But in the case of $MgCl_2$ solution, there are substantial differences up to a cut off 5.7 Å, and very tiny changes between 5.7 and 15 Å. This suggest that the collision-induced effects are very significant for salt solutions when compared to pure liquid water. Moreover, the results also suggest that the collision-induced effects from long range interactions beyond the second solvation shell are insignificant. Hence, in this work, we set r_t = 7.5 Å, which is less than half of the simulation box length used.

4.3.2 Impact of higher order terms in DID model to calculate polarizability anisotropies

Here, we have demonstrated the ability of simple DID model and extended higher-order DID models to reproduce the experimental TKE measurements. The example systems we have chosen for the purpose of this demonstration are high (4M $MgCl_2$) salt concentrated aqueous system and pure liquid water.

Pure liquid water: As shown in Figure 4.5 a), the experimentally measured terahertz kerr effect signal of pure liquid water has a bipolar shape with a positive peak followed by a negative peak, both the peaks have roughly same height. The bipolar signal is attributed to the intermolecular hydrogen bond stretching and bending vibration modes [41,42], while the relaxation tail of the negative peak is attributed to the relaxation dynamics of the excess translational KE [44].

Our polarizability anisotropy calculation shows the result when the DID model are turned off, essentially only the intramolecular response. Here, the intramolecular response is almost unipolar with a tiny positive peak, followed by a strong negative peak. The intermolecular collision-induced response

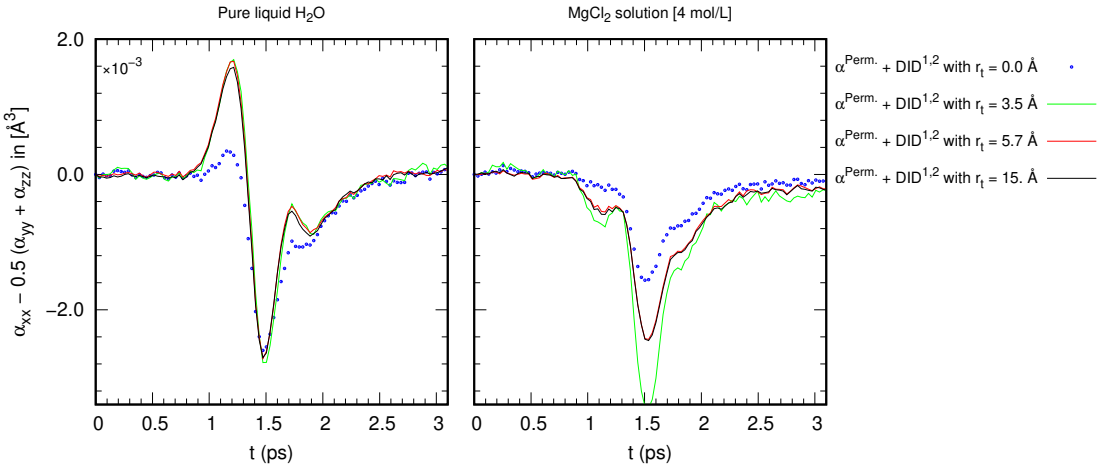

Figure 4.4: The simulated transient polarizability anisotropy of pure liquid water and $MgCl_2$ aqueous system as a function of collision induced cut offs r_t. The polarizability anisotropy is calculated via the first- and second-order molecular hyperpolarizabilities extended DID model with the non-polarizable force field MD trajectories.

can be obtained purely by simulating only the DID model. Here the intermolecular response is also unipolar but with a positive sign. Introducing the effects of interactions between hyperpolarizability and local electric field via extended DID model lead to a strong enhancement in the intermolecular unipolar response. When both intramolecular and intermolecular responses summed, the eventual shape of the response is bipolar with equal heights, which strikingly resembles the experimental measurement [44,121]. This clearly demonstrates that including the effects of interactions between hyperpolarizability and local electric field in DID model is essential to reproduce the experimental terahertz kerr effect measurements of pure liquid water.

$MgCl_2$ solution (4 mol/L): Experimental terahertz kerr effect signal of $MgCl_2$ salt aqueous solution taken from Vasilos work [44,121,241] and Haoyu Huang work [72] are shown in Figure 4.5 b). In the measurement of Vasilos, 8 times weaker pulse than the ones in this simulation work was used, while in the measurement of Haoyu Huang, slightly a different THz pulse with a maximum intensity of $5 \times 10^7 \frac{V}{m}$ was used. Haoyu Huang measurement shows a unipolar response with a strongly enhanced negative peak, while the Vasilios measurement shows almost a unipolar shape with a small positive peak, followed by a strong enhanced negative peak. This enhancement is generally attributed due to the increase of the polarizability anisotropy of water molecules [242], especially the collision induced contribution term [121].

The total polarizability anisotropy calculated via classical DID model shows a unipolar response with a strong negative peak as experiments. However, the amplitude of the negative peak position is underestimated by a factor 2.5. When the effects of interactions between first hyperpolarizability and local electric field are introduced, the amplitude of the peak is slightly enhanced and the factor reduces to 2.3. The second hyperpolarizability further reduces the factor to 2.1. The lack of polarization effects in non-polarizable force field MD accounts for this 2.1 factor disagreement, as evidenced by a considerable rise in the negative peak when using polarizable force field MD in Figure 9.3. Nevertheless, the first- and second-order molecular hyperpolarizabilities extended DID model improves the results by increasing the amplitude of the polarizability anisotropy.

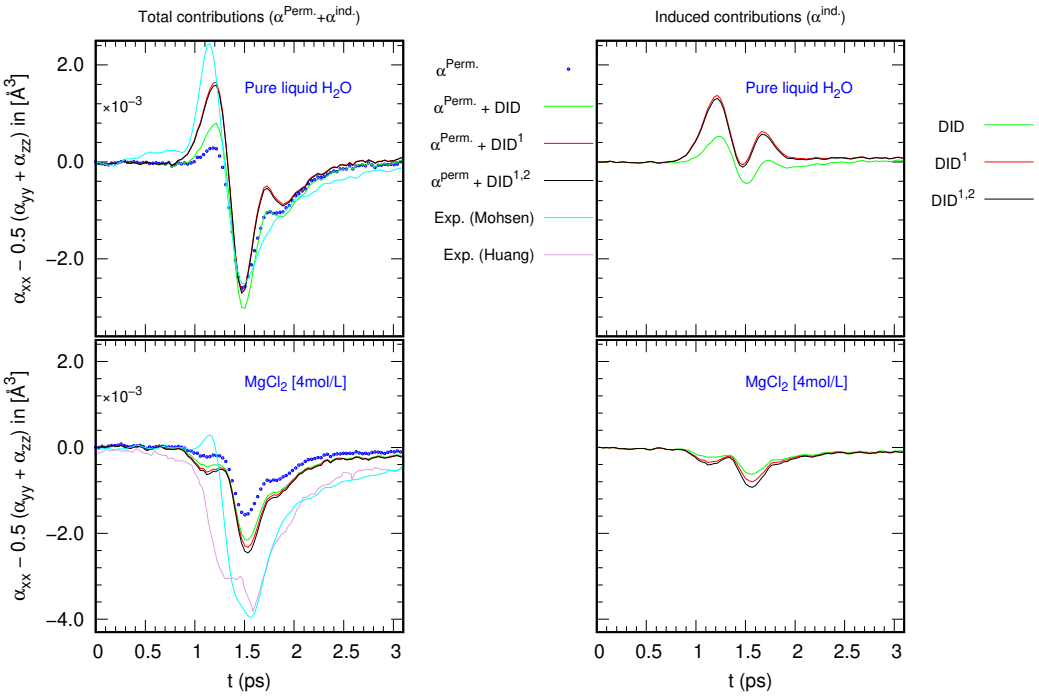

Figure 4.5: The simulated transient polarizability anisotropy of pure liquid water (top row) and $MgCl_2$ (bottom row) aqueous system, computed via classical DID model and extended higher-order DID models. In the first column of the figure, the total contribution summed from permanent and induced contributions is shown, whereas in the second column, only the induced contribution is shown, respectively. The polarizability anisotropy is calculated using the non-polarizable force field MD trajectories. Experimental measurements were taken from Ref.[44,72,121,241].

4.3.3 Impact of polarizable and non-polarizable force fields on the simulated polarizability anisotropy

Figure 4.6 shows the ability of polarizable and non-polarizable force fields to reproduce the TKE experimental measurements of various aqueous electrolyte solutions at various concentrations. With the exception of Na_2SO_4 solution, the experimentally measured concentration-dependent birefringence of several strong electrolyte solutions appears to be very well reproduced by the AMOEBA polarizable force field, whereas the non-polarizable force field model exhibits the opposite trend. This clearly suggests that the induced polarization effects must be included in the force field MD in order to accurately reproduce the TKE experimental measurements of aqueous electrolyte solutions. For polarizable force fields, the signal's amplitude is noticeably stronger, and it can be attributed to collision-induced contribution.

To better understand why the PFFMD can faithfully reproduce the experimental concentration dependency but the FFMD cannot, we separated the total polarizability anistropy of the MgCl2 salt system into intrinsic (permanent) and collisions-induced (induced) contributions, as shown in Figure 9.3. The permanent polarizability of PFFMD shows a weaker intensity when compared to that of FFMD, whereas the induced polarizability of PFFMD shows a much stronger intensity when compared to that of FFMD. This simply shows that, in contrast to FFMD, PFFMD transfers the THz energy deposited into the rotational motion of water into the translational motion of nearby molecules more efficiently. This is also supported by the water bisector orientation and translational KE, where the cosine theta of PFFMD shows a weaker signal compared to the ones in FFMD and the translational KE of PFFMD shows a stronger amplitude.

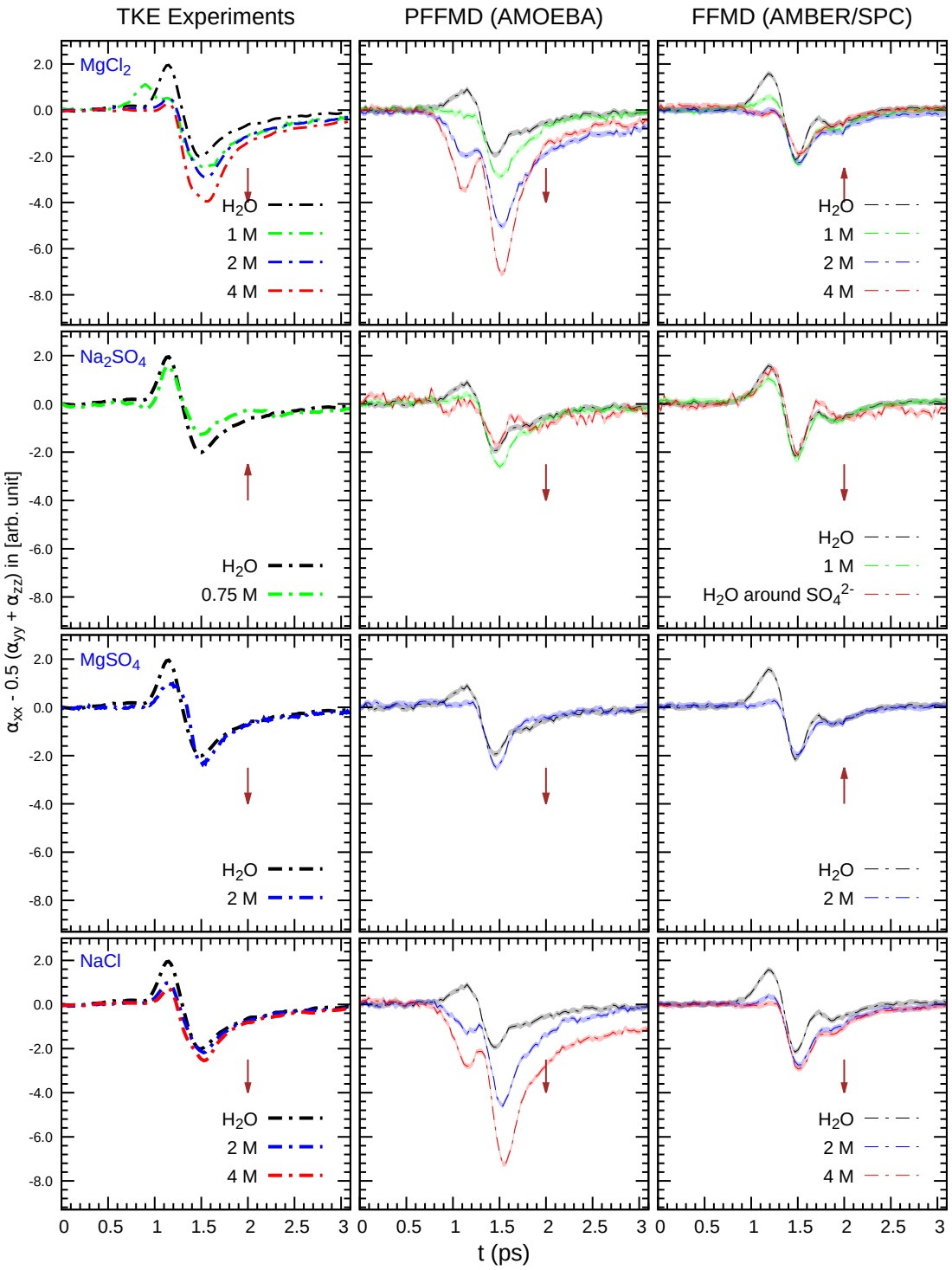

Figure 4.6: The transient polarizability anisotropy of pure liquid water and several aqueous salt systems at various concentrations, obtained via TKE experiments and MD simulations In the first column of the figure, the experimental measurement is shown, whereas in the second and third columns, the polarizability anisotropies of PFFMD and FFMD simulations are shown, respectively. The polarizability anisotropy is calculated via the first- and second-order molecular hyperpolarizabilities of the extended DID model. Experimental data were taken from the Ref. [44,72,121,241].

An Analysis of the FFMD Failure: The O-O pair RDF for pure liquid water and $MgCl_2$ salt systems is shown in Figure 4.7. The minima of the first and second RDF peaks of the AIMD water are strongly reproduced by the AMOEBA water, but some minor variations can be seen in them in the SPC water. Additionally, the structure of AMBER/SPC water in the $MgCl_2$ system is also not good enough in the RDF region between 3 and 5.5 Å, where the first and second peak minima are right-shifted in comparison to those of PFFMD and AIMD. This suggests that the interactions between ion solvation (first solvation) and bulk solvent (second solvation) of the AMBER/SPC model is weak. This weak interaction may have reduced the energy transfer between the first and second solvations and therefore having a less impact on the collision-induced contribution to polarizability anisotropy, which may be the possible reason why FFMD failure in reproducing the TKE experimental measurements.

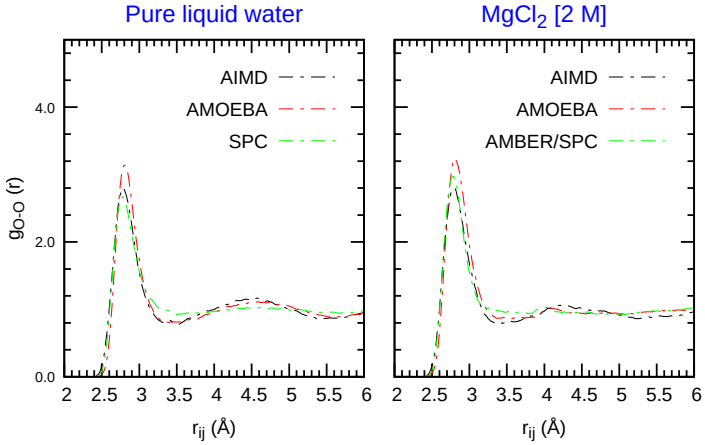

Figure 4.7: The O-O pair RDF for pure liquid water and $MgCl_2$ salt solutions, simulated from equilibrium AIMD, PFFMD, FFMD.

It is also interesting to report that the FFMD and PFFMD water in a MgCl2 aqueous system have roughly the same mean square displacement and OH vector orientation decay over shorter time scales, indicating that translational and rotational diffusion has no significant effect on FFMD failure, this is also shown in Figure 4.8.

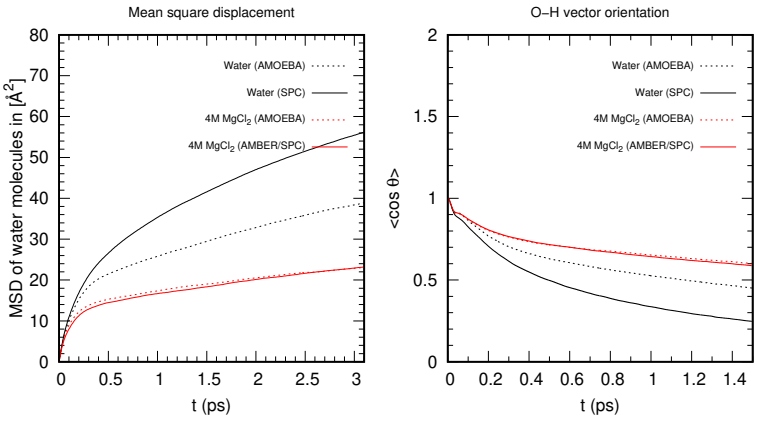

Figure 4.8: The average mean square displacement of water (left), orientational dynamics of OH vector (right) of water molecules in pure liquid water and $MgCl_2$ (4M) aqueous systems. In the orientational dynamics figure, the θ in the y axis is the angle between instantaneous and initial direction of a OH group vector in water molecules. For these analyses, the equilibrium MD trajectories were employed.

Chapter 5

Intramolecular and intermolecular energy transfer in liquid water revealed by the terahertz Kerr effect

Energy dissipation in water is very fast and more efficient than in many other liquids. This behavior is commonly attributed to the intermolecular interactions associated with hydrogen bonding. In this chapter, we aim to understand the energy transfer within the hydrogen-bonding network of liquid water by studying the non-equilibrium (*ab-initio*, non-polarizable force fields) MD trajectories of liquid water, simulated with the effect of a single-cycle THz electric pulse (see Chapter 3 and Chapter 2 for more on simulation details and method descriptions). During the MD simulations, the THz pulse excite the collective rotational degrees of freedom of water, and the resulting (TKE-induced) transient-polarizability anisotropy response[243] is calculated using the using DID^{1,2} formalism. We also computed the cross-correlation functions between components of the angular and COM velocities for non-polarizable force fields water in order to explore the intramolecular and intermolecular rotation-translation energy transfers that occur in liquid water.

5.1 Simulation results and discussion

THz-induced molecular orientation and structural anisotropy: We here calculate the degree of molecular orientation as an ensemble average of the angle between the THz electric field and the molecular bisector. The results of our AIMD simulations are given in Figure 5.1 (left). The orientation of water molecules follow the patterns of THz pulse waveform with a small phase shift ($\sim$ 150 fs). To see whether all types of water molecules participate in the reorientation process, we determine the orientation response ($\cos\theta$) for water molecules in strong and weak hydrogen bonding environments with the help of γ_d parameter. The γ_d is a dimensionless asymmetry parameter primary used to define the asymmetry between two strong HB donor interactions involving a specific water molecule. The expression used to calculate γ_d is typically written as,

$$\gamma_D = 1 - \frac{\triangle E_{A\rightarrow B^{2nd}}}{\triangle E_{A\rightarrow B^{1st}}} \tag{5.1}$$

where the $\triangle E$ terms are the two strongest two-body donor (involving charge transfer from molecule A to B) interaction energies, which are calculated using the ALMO-EDA technique[31,32,192,193]. Therefore, the water molecules with high γ_d ($\gamma_d > 0.8$) have strong asymmetric hydrogen bonding environ-

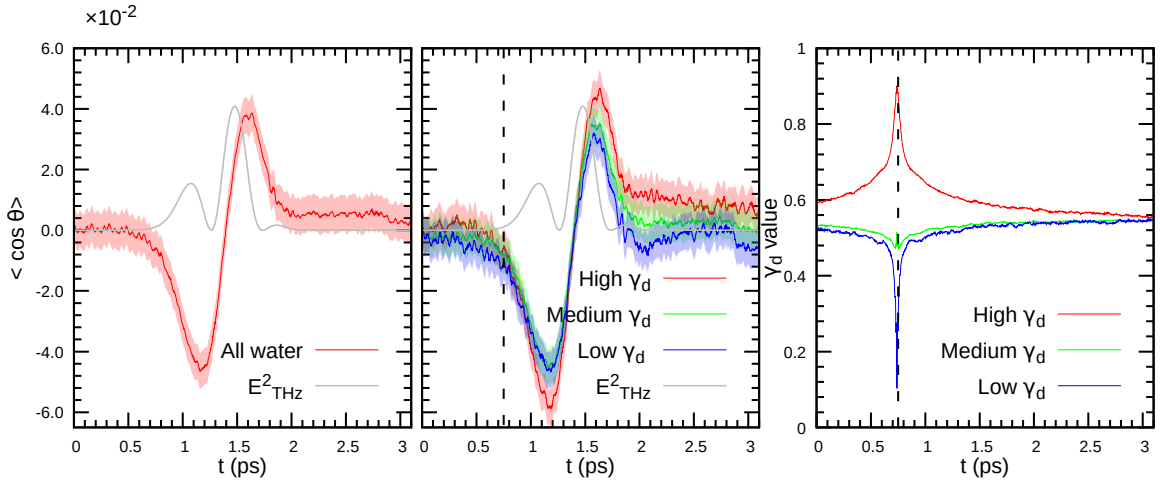

Figure 5.1: Left figure shows the time-varying alignment of the all the water molecules in the AIMD liquid water during the THz pulse excitation. The middle figure shows the time-varying alignment of water molecules with high, medium and low γ_d water molecules individually. The right figure displays the γ_d value for all the three species as a function of time. The time in which the γ_d value probed is shown by dashed black straight vertical line. Here the θ in y axis is the angle between water molecular bisector and the THz electric field direction. E^2_{THz} is the square of the THz electric field. The shadowed areas indicate standard errors.

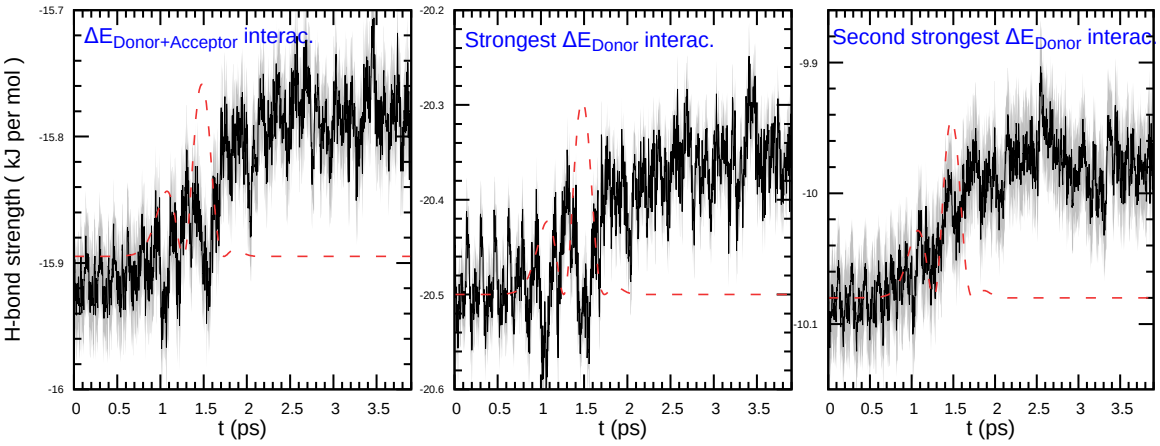

Figure 5.2: Time evolution of the HB strength for all HB interactions (Left figure), strongest donor interactions (Middle figure) and second strongest donor interactions (Right figure), respectively. Under field-free conditions, the calculated average HB strength in liquid water is $\sim$ -15.90 $\frac{kJ}{mol}$, whereas the average strongest and second-strongest donor interaction energies are $\sim$ -20.5 $\frac{kJ}{mol}$ and $\sim$ -10.1 $\frac{kJ}{mol}$. These calculations only take into account the tetrahedral HB network of liquid water. The red dashed line represents the square of the THz electric field. The shadowed areas indicate standard errors.

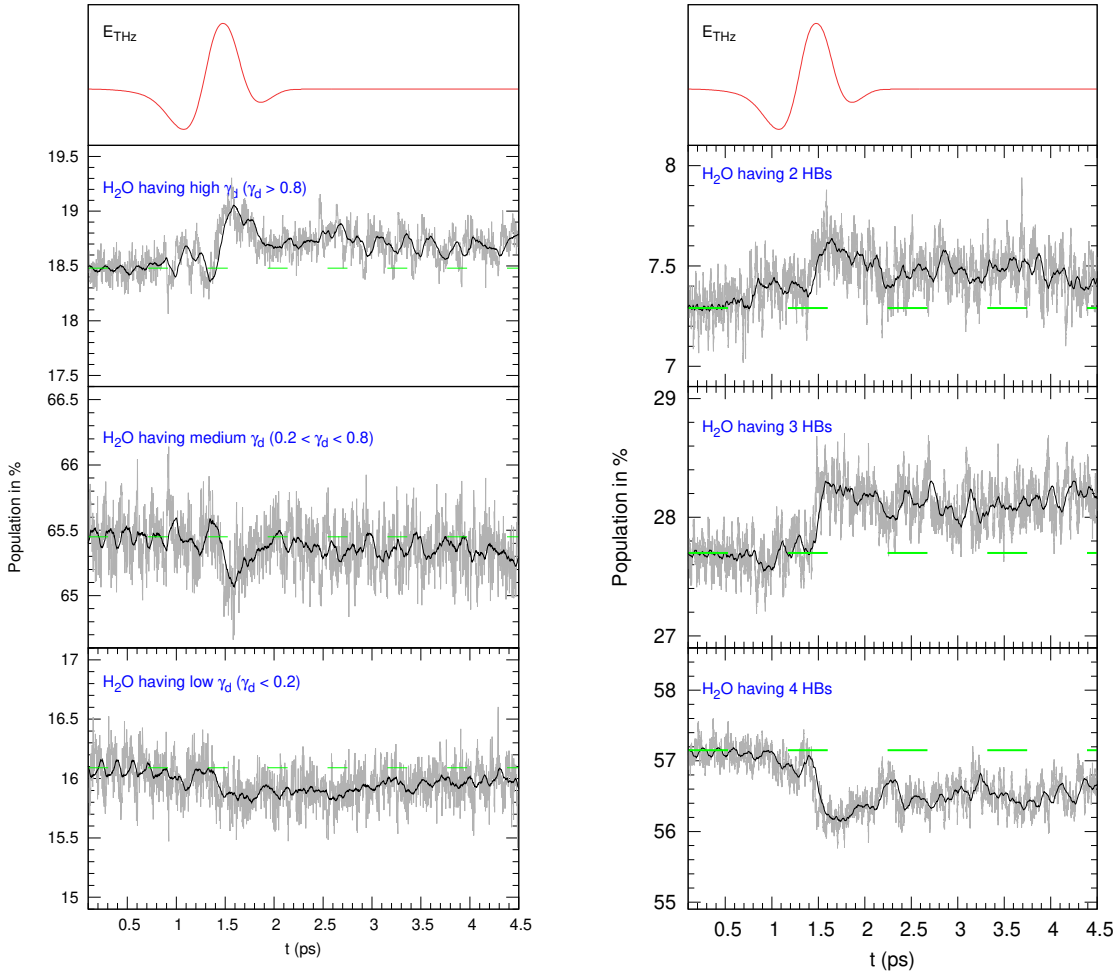

Figure 5.3: Variation in the population of a) high, low, and medium γ_d (Left figure) b) 2, 3, 4 H-bonded (Right figure) water molecules in the AIMD liquid water during the THz pulse excitation. The gray line shows the instantaneous value of the population, while the dark black line shows the 32 fs running average value of the population. The dashed green line represents the average population value under pulse-free conditions (i.e., before 0.5 ps). Top panel shows the THz pulse profile and amplitude.

ments [9,244–246], while those with low γ_d ($\gamma_d < 0.2$) have symmetric hydrogen bonding environments. As shown in Figure 5.1 (middle), the alignment of water molecules in response to the field is much stronger for the water species with a high γ_d than for other two water species. This is to be expected, since one of the weakly H-bonded proton in high γ_d water molecules dissipates less field energy via HB network due to the lengthened H-bonds [247], when compared to the other species. The low γ_d water is found to be more constrained in the field direction [248] due to its symmetric and strong hydrogen bonding environments [9,31,32,193]. Nevertheless, all three water species in the system orient and reorient in response to the direction of the field in the same speed without any time delay among them. It is interesting to report that the effect of γ_d-anisotropy in the orientational response persists more than a ps, even though the high γ_d-lifetime is $\sim$ 50 fs. However, the residual asymmetry that is present after $\sim$50 fs, as can be seen in Figure 5.1 (right), shows a slow non-exponential relaxation behaviour [31,193], which, in our opinion, is the primary cause for such a longer persistence in the alignment of high γ_d water molecules.

We have also calculated the changes in the population of water molecules having high, medium, and low γ_d as a function of time, as shown in Figure 5.3 (left). Under the pulse-free conditions i.e., before the THz excitation, the percentage of all three γ_d water species fluctuates slightly around the average value over time. When the intensity of THz pulse starts increasing, the population of water molecules with high γ_d starts rising minimally, while the population of remaining two species drops. This evidence shows that the THz pulse excitation enhances a small structural anisotropy in the HB network of the liquid water, which is in agreement with earlier MD simulation studies [7,48,248]. After the excitation, the population value of all the species slowly drops but fluctuates below/above their average values due to the observed temperature jump (see Figure 5.5 (middle)).

As shown in the Figure 5.3 (right), we have also further studied the population of water molecules with 2, 3, or 4 H-bonds as a function of time to understand the effects of THz pulse on the local HB network connectivity of liquid water. Interestingly, the THz excitation leads to the formations of more two- and three-coordinated water molecules by breaking the tetrahedral HB network [249]. This excess H-bond breaking in the system has resulted in a slight decrease in the average number of H-bonds per water molecule (see Figure 5.5) and a weakening of the strength of H-bonds (see Figure 5.2), making the system slightly less energetically favourable to form H-bonds. Moreover, we also observe a slight rise in the average temperature of the system (see Figure 5.5) and also a minute increase in the average HB length and angle [249], thus making the charge transfer via the HB minutely less favorable as it corresponds to a tiny elevation in the electric potential along the HB, which is at variance to the response observed during the ultrafast intense electric field pulse [7,48,250]. The THz field reduces the strength of H-bonds or water/water interaction energy by $\sim$ 0.1 KJ per mol. Under the pulse-free conditions, we found that the average population of all the water species in agreement with the previous reports [31,193,251–255].

Simulated THz-induced optical birefringence: In our TKE MD simulations, due to the action of the pump field polarized along x, we observe a transient difference $\triangle n = n_x - \frac{n_y+n_z}{2}$ between the refractive indices along the x and other two directions y and z. The resulting birefringence is given by [68]

$$\triangle n \propto < \triangle\Pi(t)_{xx} - \frac{\triangle\Pi(t)_{yy} + \triangle\Pi(t)_{zz}}{2} > \tag{5.2}$$

where $\triangle\Pi(t)_{\alpha\beta}$ is the pump-induced change in the collective electronic polarizability tensor element $\Pi(t)_{\alpha\beta}$, α, β are the x,y, and z directional components. Here, Π refers to the liquid phase and contains contributions from interactions/collisions between molecules in the condensed phase. The variation $\triangle\Pi$ can, in principle, be written as a sum $\triangle\Pi^{\mathrm{M}} + \triangle\Pi^{\mathrm{I}}$, whose two contributions arise, respectively, from the intrinsic gas-phase molecular polarizability ($\triangle\Pi^{\mathrm{M}}$) and the intermolecular interactions and collisions ($\triangle\Pi^{\mathrm{I}}$) in the condensed phase [96,97,100].

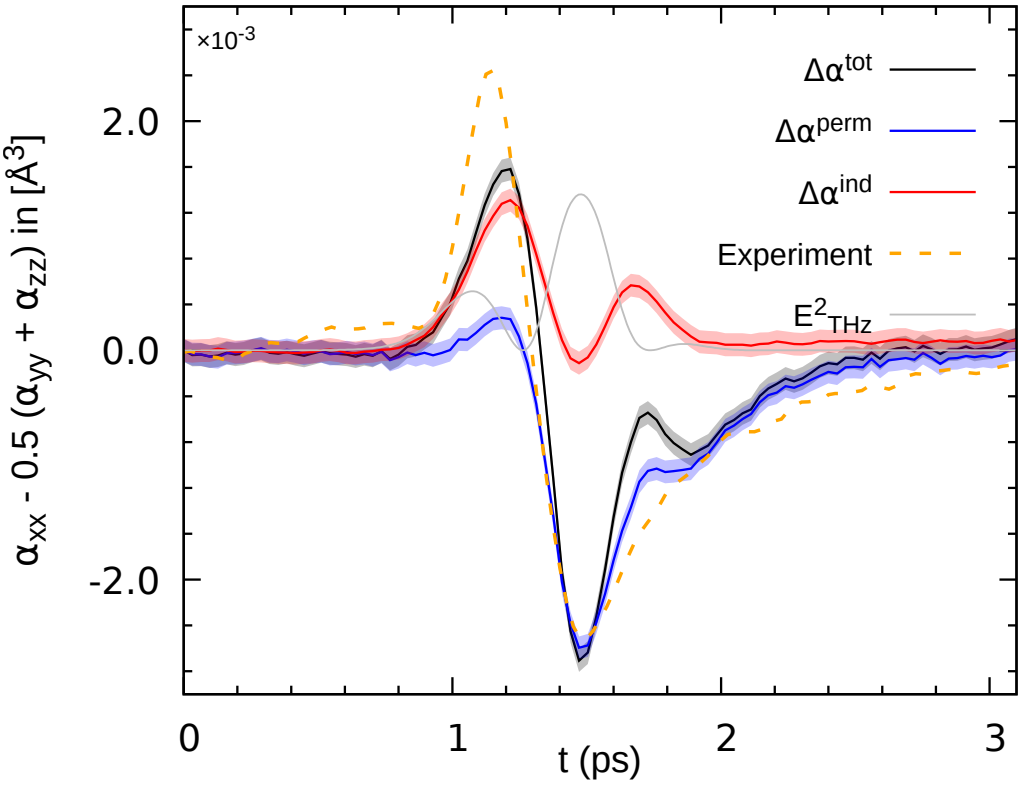

Figure 5.4: Simulated transient polarizability anisotropy for SPC liquid water during the THz pulse excitation. The total polarizability anisotropy $\triangle\alpha$ (black), single molecule $\triangle\alpha^{\mathrm{perm}}$ (blue) and collision-induced $\triangle\alpha^{\mathrm{ind}}$ (red) contributions are shown separately. $\mathrm{E}^2_{\mathrm{THz}}$ is the square of the THz electric field. The shadowed areas indicate standard errors.

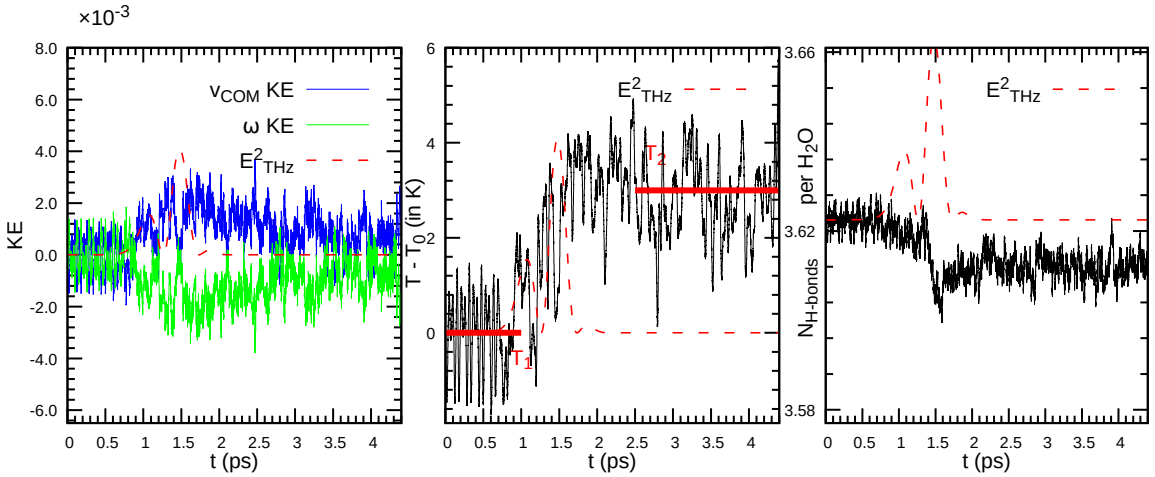

Figure 5.5: Variation in the AIMD liquid water's (a) translational and rotational kinetic energies, (b) mean temperature, (c) average number of H-bonds per water molecule, during the THz pulse excitation. To show the THz-induced temperature jump, the red lines are drawn in temperature graph. The horizontal red lines in the temperature graph represent the average temperature value under pulse-free conditions (i.e., before 0.5 ps is T_1) and after the THz excitation (i.e., between 3 - 4.5 ps is T_2). Here T_0 is the ambient temperature.

The $\triangle\Pi^M(t)$ characterizes the degree of anisotropy of the unperturbed Π and is usually labelled $\triangle\alpha^{\text{perm}}$ for single molecules. Averaging $\triangle\alpha$ over all molecules according to equation 5.2 yields an expression for single-molecule rotational birefringence $\triangle n_{rot}$ that scales with the degree of molecular alignment with respect to the polarization axis of the THz pump pulse. The averaged $\triangle\Pi^{\text{I}}(t)$ makes another contribution to the transient birefringence and arises directly or indirectly from the pump-induced changes in the collision-induced polarizability. Additionally, THz electric-field-induced ionization and charge separation may contribute to the total polarizability of water [256,257]. However, as demonstrated by Elsässer and co-workers, the latter contributions modulate the isotropic part of the complex dielectric response of water, with negligible impact on its anisotropic response, measured in the TKE experiment [256,257]. Here the $\triangle\Pi^{\text{I}}(t)$ is labelled as $\triangle\alpha^{\text{ind}}(t)$ and computed using DID^{1,2} model, whereas the $\triangle\alpha^{\text{perm}}$ of water molecules were computed in the gas phase conditions using the parameters in Table 3.1.

The calculated THz-pulse–induced polarizability anisotropy of liquid water (simulated with SPC water model) is shown in Figure 5.4 together with experimental measurements of pure liquid water, conducted by Mohsen Sajadi and Vasileios Balos [44,121]. The experimental measurement has a bipolar shape with a positive peak followed by a negative peak, both the peaks have roughly same height. The bipolar signal is attributed to the intermolecular hydrogen bond stretching and bending vibration modes [41,42], while the relaxation tail of the negative peak is attributed to the relaxation dynamics of the excess translational KE [44].

Our polarizability anisotropy calculation shows the result when the DID^{1,2} model are turned off, essentially only the intramolecular response. Here, the intramolecular response is almost unipolar with a tiny positive peak, followed by a strong negative peak, which is the main contributor the second peak of the bipolar signal. The intermolecular collision-induced response can be obtained purely by simulating only the DID^{1,2} model. Here the intermolecular response has two positive peaks, the first of which contributes to the first peak of the bipolar signal and the second to its relaxation. When both intramolecular and intermolecular responses summed, the eventual shape of the response is bipolar with roughly equal heights, which strikingly resembles the experimental measurement.

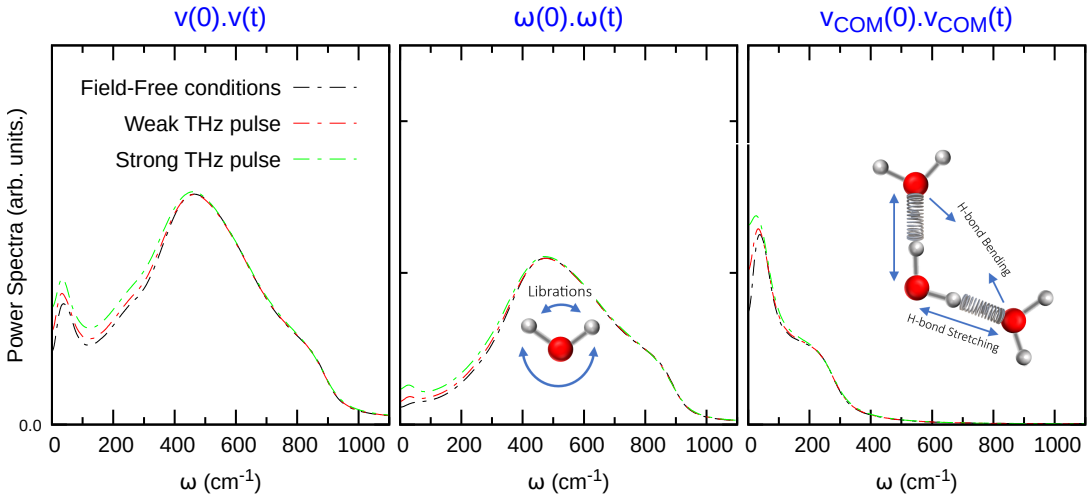

Figure 5.6: Power spectra for SPC liquid water under field-on (strong and weak THz pulses used) and field-free conditions. The spectra is calculated by Fourier transforming the auto-correlation function of its velocity, center of mass velocity, and angular velocity. The insets illustrate the intermolecular motions of the water, such as HB stretching, HB bending, and libration modes.

The single molecule term $\triangle\alpha^{\text{perm}}(t)$ results from the THz-induced molecular orientation or rotation, which is an IR-active (THz-active) motion, and the induced term $\triangle\alpha^{\text{ind}}(t)$ results from the molecular collision and the translation, which is a Raman active motion . Therefore, the results of the polarizability anistropy explored both IR and Raman active modes. In other words, the resulting (TKE-induced) transient-polarizability anisotropy response $\triangle\alpha(t)$ monitored both the Raman and IR active modes.

KE transfer : The main outcome of our MD simulations, shown in Figure 5.4, is that the observed dynamics in the experimental birefringence measurements of water excited at 1 THz originate also from the collision/interaction-induced polarizability. The remaining intriguing question is the mechanism of this effect. A collision-induced change in the polarizability must eventually be traced back to the restricted rotations and translations of molecules, and how their polarizability is modified as they stumble into their neighbors while rotating/translating.

To shed light on the nature of the underlying motion, we refer again to our MD simulations and calculate the KE evolution of water molecules after their excitation with the THz pulse at 1 THz. In the AIMD simulations, we partition the total KE of the system into three contributions from molecular rotational, translational, and intramolecular vibrational contributions. The latter component remains almost constant within the noise level and is not strongly affected by THz pulses [206], thereby is not shown. We monitor the deviation from equipartitioning by plotting the ratio of the translational (rotational) KE to the instantaneous total KE. A deviation of this ratio from one-third gives a non-equilibrium distribution of KE. Here, we also observe the transient non-equilibrium partitioning of KE between the molecular translational and rotational dynamics, with KE_{trans} gaining more KE at the expense of KE_{rot}. The MD simulation results also show that the relaxation dynamics of the excess KE_{trans} match nicely with the relaxation tail of the THz-pulse-induced-polarizability response of water. In AIMD, it relaxes to its equilibrium value also exponentially with a time constant of $\sim$ 0.75 ps.

The situation with AIMD is more subtle. Here, not only rotations but also translations are IR active. Previous AIMD simulations have shown that the H-bond stretching peak at 200 cm^{-1} is IR active, while the H-bond bending peak at 50 cm^{-1} does not seem to be so [258]. Here, to establish the

energy flow pathway, we calculate the power absorbed from the THz electric field by the molecular translations and rotations. We accomplish this by directly calculating the coupling between the electric field vector and the molecular Born effective charges, in case of the translations and with the MD dipoles, for the rotations[259].

Power Spectra : We have also calculated the power spectra for SPC liquid water by Fourier transforming the auto-correlation function of its velocity, center of mass velocity, and angular velocity. The spectra were calculated under field and field-free conditions, as shown in Figure 5.6. In the spectra, we observe intensities in the $\sim 0-1000$ cm^{-1} spectroscopic range, which corresponds to the translation and rotation motions of water molecules. The peak around ~ 50 cm^{-1} is assigned to the HB bending modes, the shoulder region in the COM velocity spectra around ~ 200 cm^{-1} is attributed to the HB stretching modes, and the peak around ~ 500 cm^{-1} is attributed to the librational modes[260–262] generated through the process of hydrogen bond breaking and reforming.

The THz excitation increase the amplitude of the spectra in the $\sim 0-500$ cm^{-1} spectroscopic region, which contains both translational and low-frequency librational motions of water molecules. The high-frequency librational motions, or the regions above ~ 500 cm^{-1}, are unaffected. Here, the intriguing question is how the THz energy, which was solely deposited into rotational motion of water molecules, induced the features that correspond to the translation motion of water molecules; the explanation for this will be covered in more detail in the following section.

How is the THz pulse energy pumped into the rotational degrees of freedom of water is transferred to the translational motion of the neighboring water molecules? : During the THz excitation, we observed the KE transfer in liquid water from rotation motion to translation motion, as well as the enhancement of characteristics that correspond to the translational and low-frequency librational motions of water molecules. This phenomenon can be examined by computing the cross-correlation functions[194–204] between the COM and angular velocities of the individual water molecules or of two H-bonded water molecules. The cross-correlation function between COM and angular velocities of a water molecule is referred as intramolecular rotation-translation coupling cross-correlation function, while those of two H-bonded water molecules is referred as intermolecular rotation-translation coupling cross-correlation function. Both the intramolecular and intermolecular cross-correlation functions are tensors with nine components that can be computed on both the Cartesian and molecular axes[194]. The intramolecular and intermolecular rotation-translation coupling cross-correlation functions are typically written as[194,198–200,204],

$$\text{Intramolecular rotation-translation coupling CCF} = \frac{< \omega_{i,\alpha}(0) \cdot v_{\text{COM},i,\beta}(t) >}{< \left|\omega_{i,\alpha}(0)\right| \cdot \left|v_{\text{COM},i,\beta}(0)\right| >} \tag{5.3}$$

$$\text{Intermolecular rotation-translation coupling CCF} = \frac{< \omega_{i,\alpha}(0) \cdot v_{\text{COM},k,\beta}(t) >}{< \left|\omega_{i,\alpha}(0)\right| \cdot \left|v_{\text{COM},k,\beta}(0)\right| >} \tag{5.4}$$

where α, β are the x, y, and z directional components, ω_i and $v_{\text{COM},i}$ are the COM and angular velocities of water molecule i, which can be obtained by the following equations:

$$\vec{v}_{\text{COM},i} = \sum_{j=1}^{3} \frac{m_j}{M_i} . \vec{v}_j \tag{5.5}$$

$$\vec{\omega}_i = \sum_{j=1}^{3} \frac{\vec{r}_j \times \vec{v}_j}{|\vec{r}_j|^2} \tag{5.6}$$

$$\vec{r}_{\text{COM},i} = \sum_{j=1}^{3} \frac{m_j}{M_i} . \vec{r}_j \qquad and \qquad M_i = \sum_{j=1}^{3} m_j \tag{5.7}$$

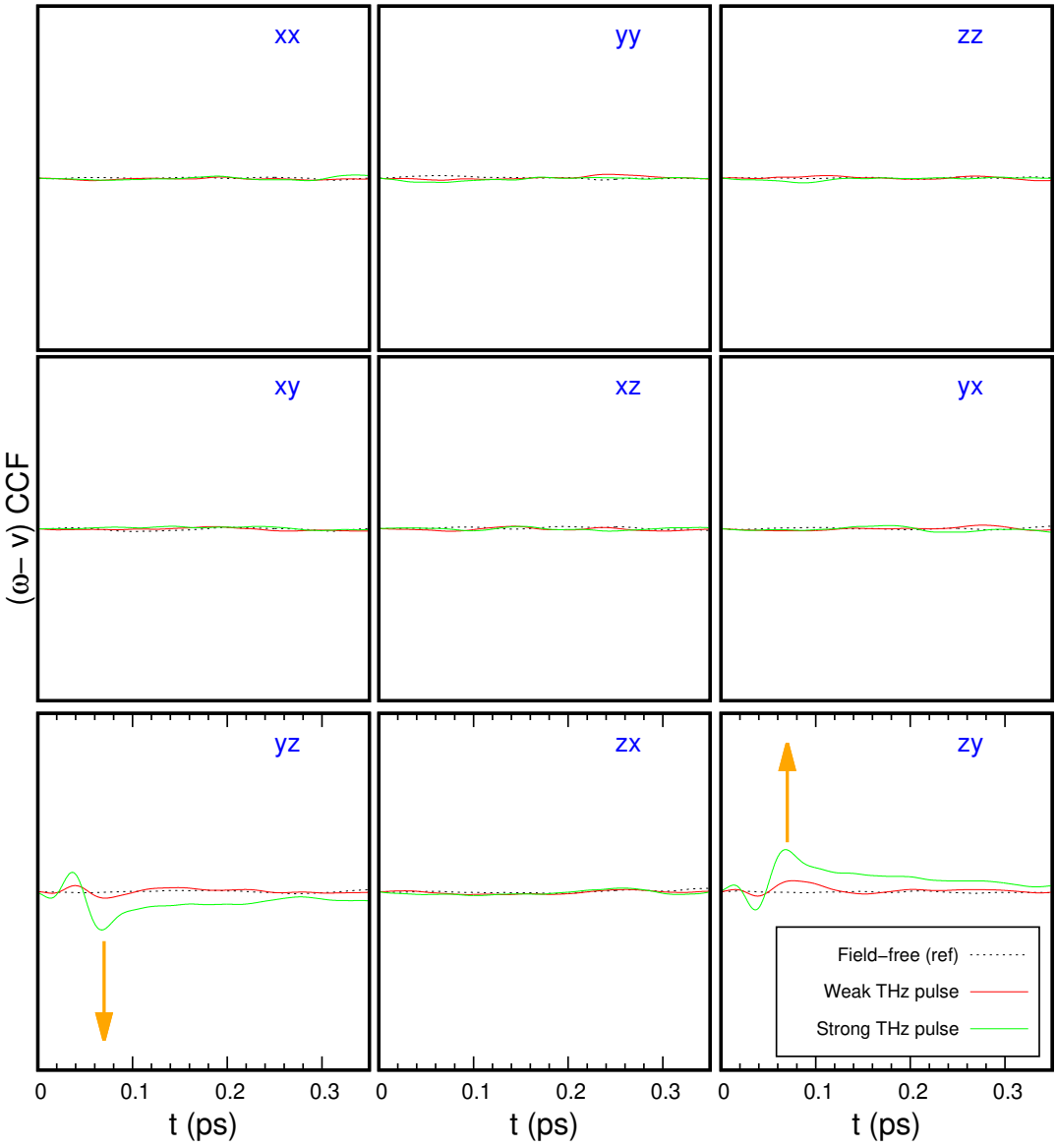

Figure 5.7: Intramolecular rotation-translation coupling CCF of nine components for SPC liquid water under field-on (strong and weak THz pulses used) and field-free conditions. In this figure, the Cartesian coordinates axis system is used.The field is applied in the x-direction. An arrow is drawn to indicate the enhancement or suppression of CCF components. All the Figures are plotted using the identical scale.

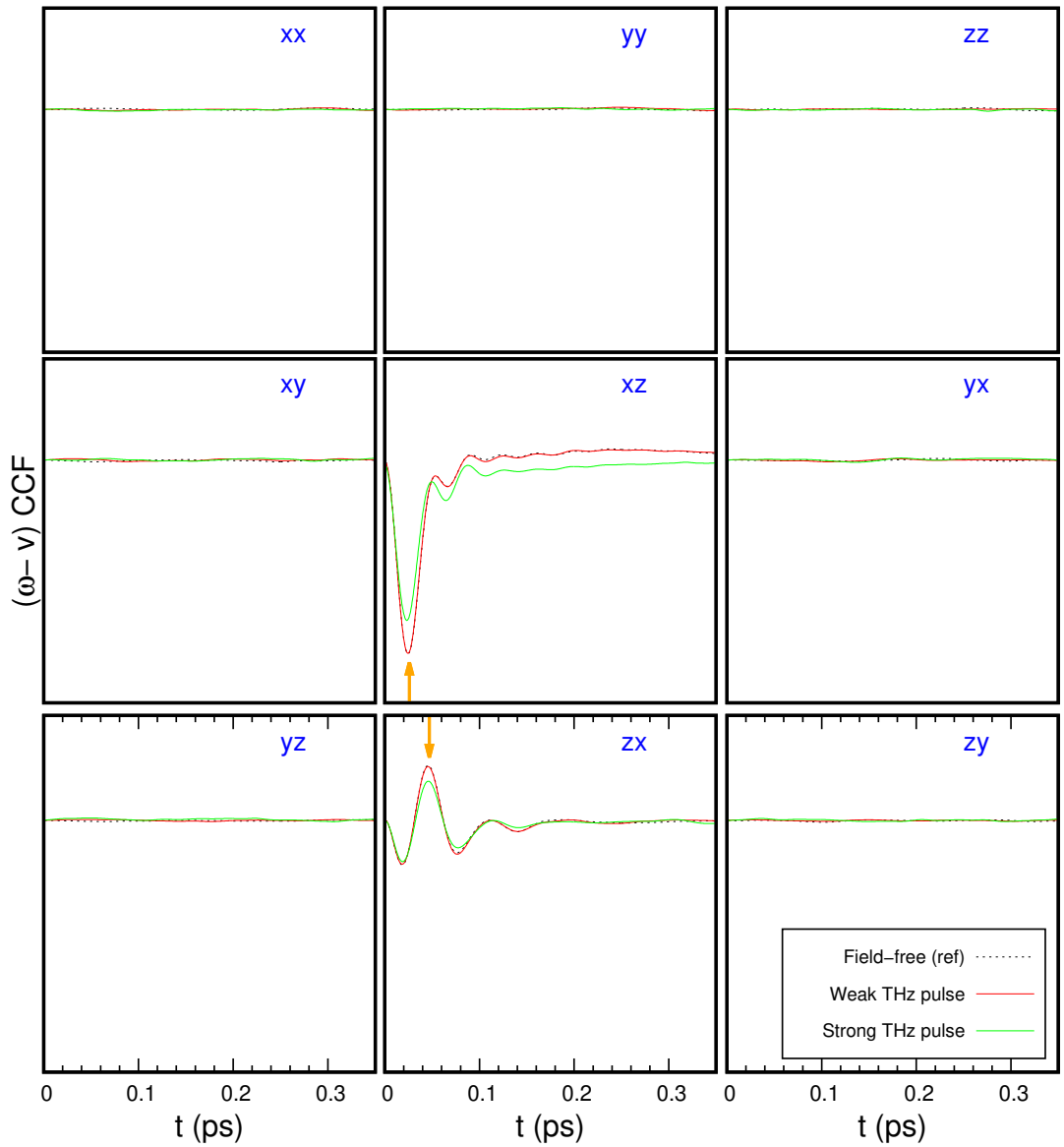

Figure 5.8: Intramolecular rotation-translation coupling CCF of nine components for SPC liquid water under field-on (strong and weak THz pulses used) and field-free conditions. In this figure, the molecular axis system is used. Note that in the molecular frame of our water molecule, the x-axis belongs to the vector uniting the two hydrogen atoms (H-H vector), y-axis to the vector of water bisector and the z-axis to the vector perpendicular to both water bisector and H-H vector. An arrow is drawn to indicate the enhancement or suppression of CCF components. All the Figures are plotted using the identical scale.

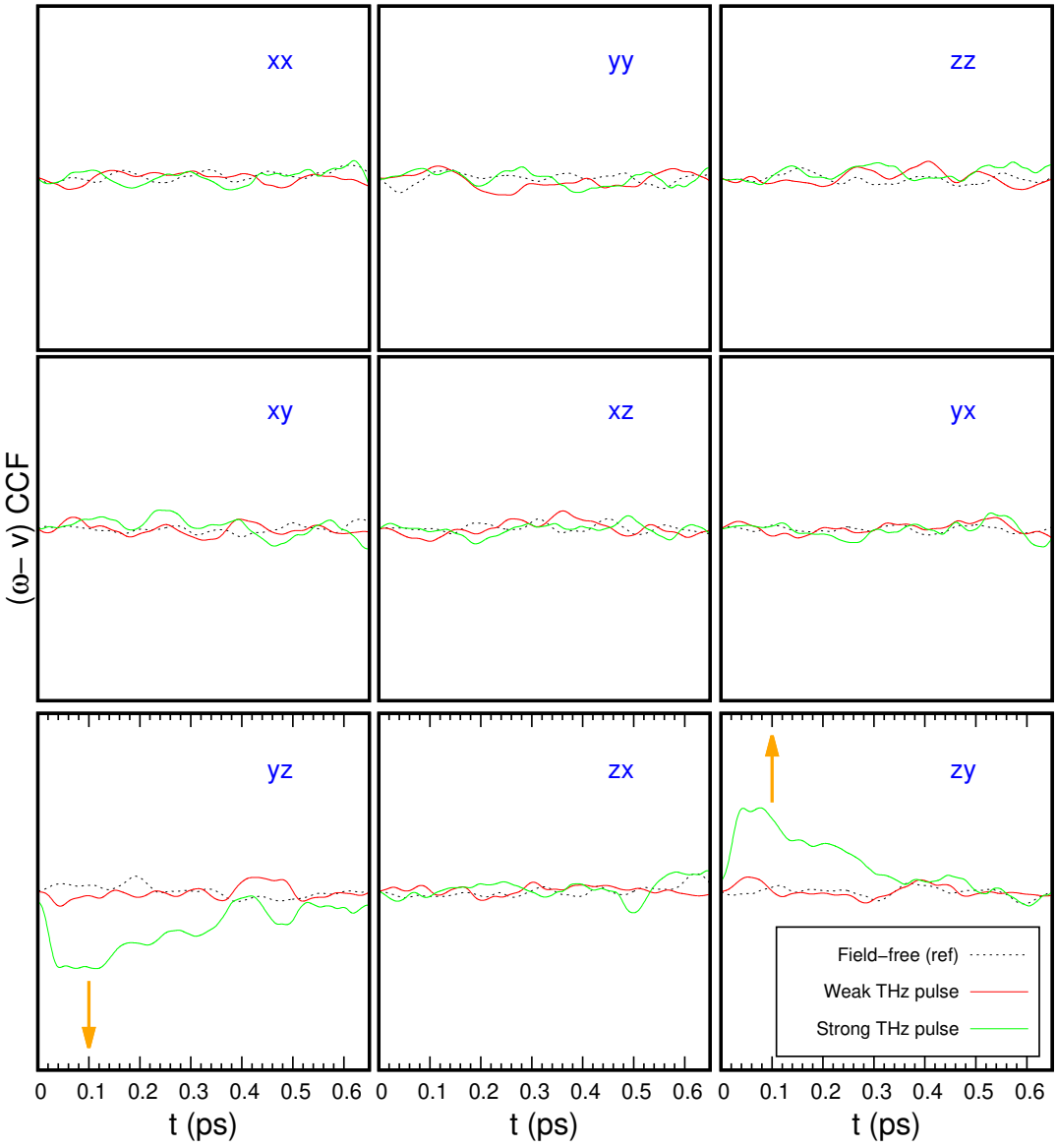

Figure 5.9: Intermolecular rotation-translation coupling CCF of nine components for SPC liquid water under field-on (strong and weak THz pulses used) and field-free conditions. In this figure, the Cartesian coordinates axis system is used. The field is applied in the x-direction. An arrow is drawn to indicate the enhancement or suppression of CCF components. All the Figures are plotted using the identical scale.

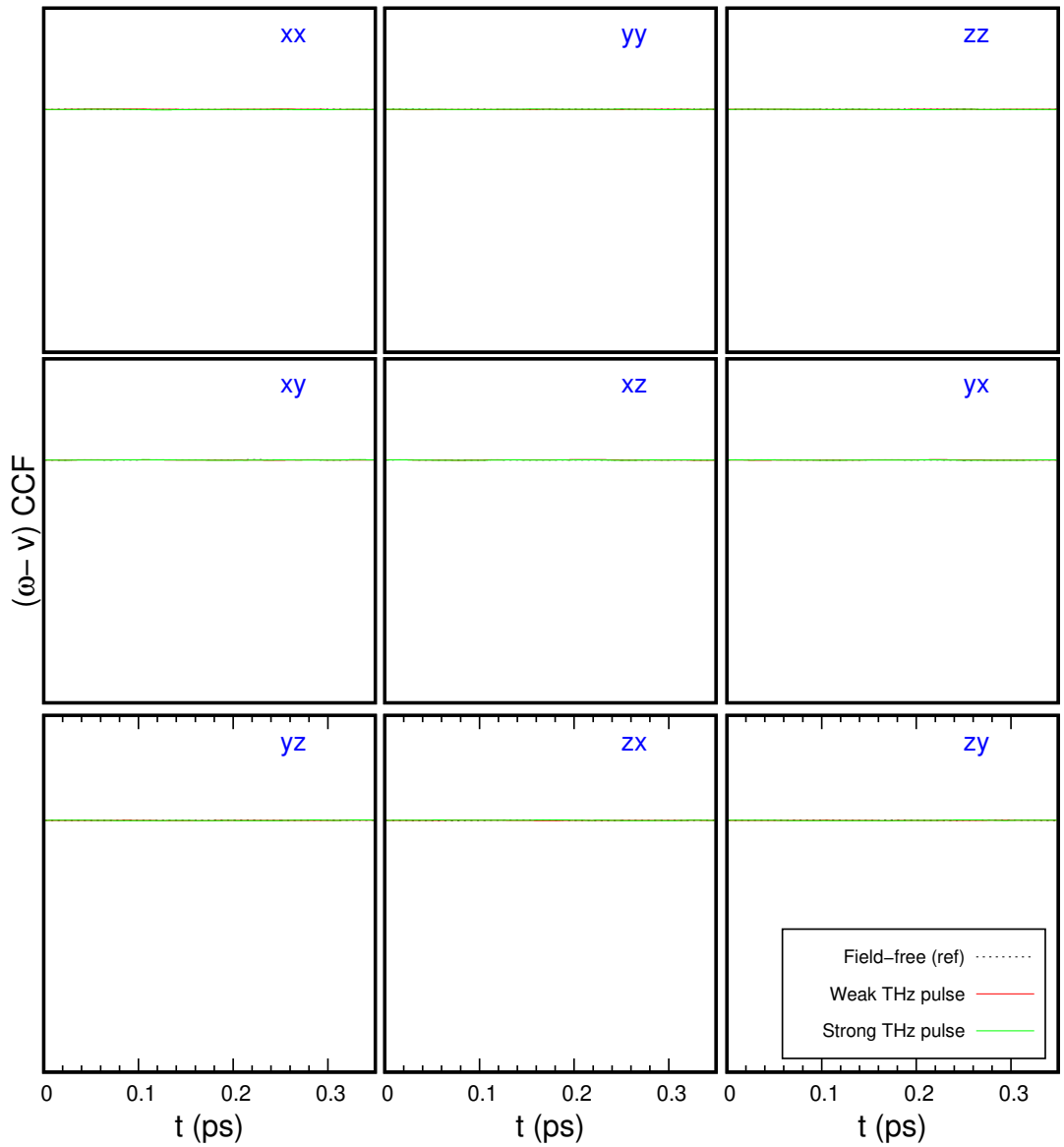

Figure 5.10: Intermolecular rotation-translation coupling CCF of nine components for SPC liquid water under field-on (strong and weak THz pulses used) and field-free conditions. In this figure, the molecular axis system is used. Note that in the molecular frame of our water molecule, the x-axis belongs to the vector uniting the two hydrogen atoms (H-H vector), y-axis to the vector of water bisector and the z-axis to the vector perpendicular to both water bisector and H-H vector. An arrow is drawn to indicate the enhancement or suppression of CCF components. All the Figures are plotted using the identical scale.

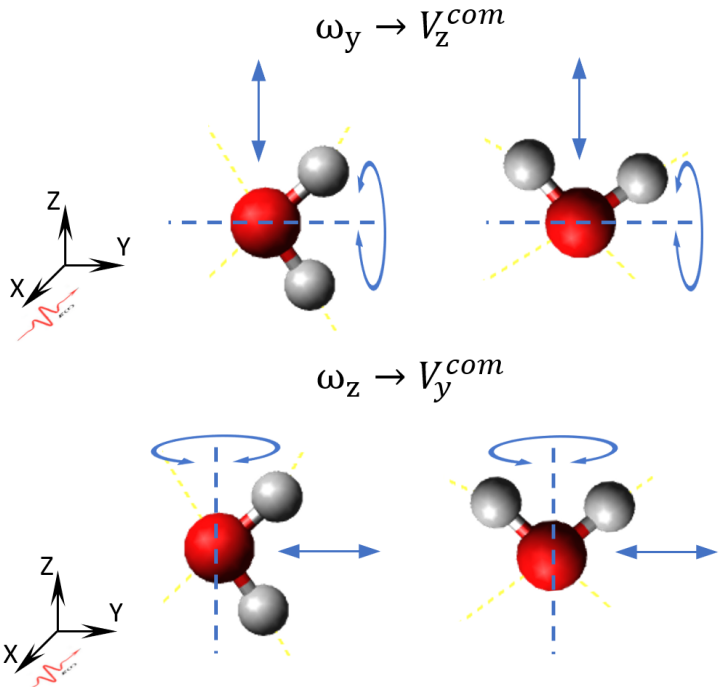

Figure 5.11: Intramolecular rotational-translational coupling of the individual water molecules. The energy transfer in the YZ direction is depicted in the top picture and the ZY direction in the bottom figure.

where M_i is the mass of water molecule i, $\vec{r}_j$ and $\vec{v}_j$ are the position and velocity of atom j, respectively. The latter two are subtracted with their center of mass position and velocity in order to shift them to molecular frame. The $|\vec{r}_j|^2$ is introduced in angular velocity calculations to bring its unit to $\frac{1}{time}$ [194,205]. Note that here the j represents the atoms and the i, k represent the molecules.

Figures 5.7 - 5.10 shows the nine components of intramolecular and intermolecular rotation-translation coupling cross-correlation function tensors for SPC liquid water under field-on (strong and weak THz pulses used) and field-free conditions. The components are displayed in both Cartesian and molecular axes. In the molecular axis of our water molecule, the x-axis belongs to the vector uniting the two hydrogen atoms (H-H vector), y-axis to the vector of water bisector and the z-axis to the vector perpendicular to both water bisector and H-H vector.

Examining the components of the intramolecular cross-correlation function tensor in Cartesian axis, the yz- and zy-components are enhanced in the field-on condition, which is the most notable difference between field-on and field-free MD simulations. At shorter timescales, a small repetition of pattern with a crest and trough can be observed, and the distance of one cycle is 55 fms ($\rightarrow$ 17 THz $\rightarrow$ 600 cm^{-1}), which corresponds to the librational motion of water. This means that when the THz pulse is applied in the x-direction of the system, the water molecules librating around y- and z-axes, due to intramolecular rotational-translational coupling, translate the water molecule in z- and y-directions in less than 100 fms [263], this energy transfer picture is depicted in Figure 5.11. Furthermore in the correlations, both the components are perfect mirror images of each other because of the axial symmetry. These results are in excellent agreement with Evans' work [199,200,204], which he labelled this entire phenomenon as *electric-field-induced translational anisotropy*.

In molecular axis, the intramolecular cross-correlation function tensor has two non-zero components in xz- and zx-symmetry. We observe a suppression in both the components in the field-on condition, which is the difference here. This means that as the external electric field's strength increases, it dominates the thermal forces of molecular axis, whose effects on the cross-correlation function reduces

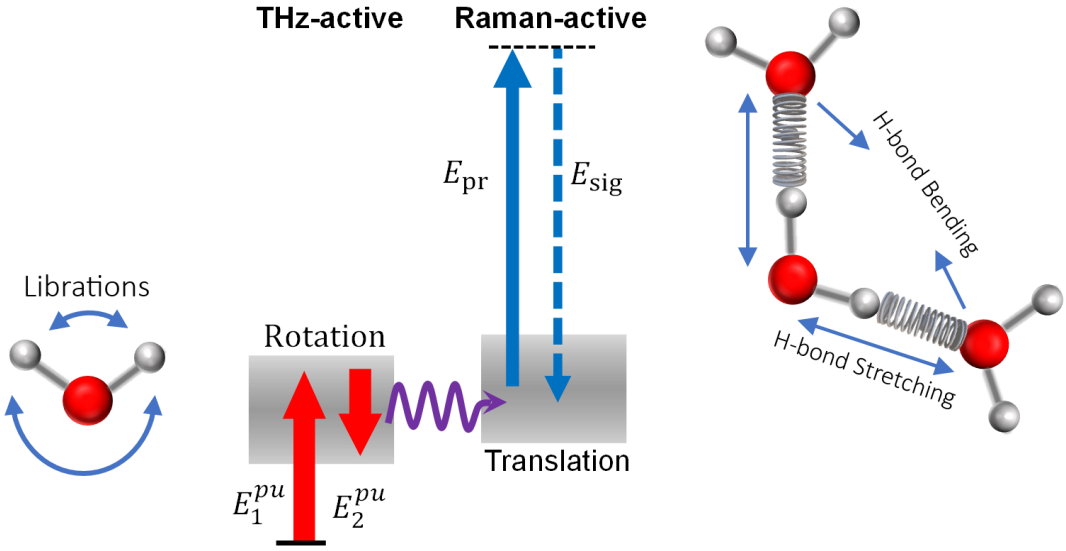

Figure 5.12: Upon excitation of the rotational degrees of freedom of water with the intense THz field (corresponding to two THz electric-field (E) interactions with the system, E_1^{pu} and E_2^{pu}), the deposited energy is rapidly transferred to the translational degrees of freedom and increases its KE. This causes an increase in the collision rate between molecules, accompanied by the enhancement of the polarizability of the system, which is resolved by a Raman interaction via optical fields E_{pr} and E_{sig}.

relative to the electric field. In other words, the rotation-translation motion in the molecular axis begins to decouple due to the strong torque caused by the strong electric field. These results are also in consistent with other studies [194,199,200,204,205,248,264,265].

Figure 5.10 shows that no component of the intermolecular cross-correlation function tensor is being enhanced or suppressed in molecular axis. But, we observe enhancement in yz- and zy-components of the intermolecular cross-correlation function tensor in Cartesian axis, as shown in Figures 5.9. This indicates that the rotation motion of a water molecule has impact on its nearest-neighbor water molecules translational motion in y- and z-directions, via intramolecular energy transfer but not via direct rotation-translation interaction between two water molecules. This is expected since the intramolecular energy transfer in the y- and z- directions takes place, causing molecule-to-molecule collisions in those directions. Moreover, we also see repetition of pattern on longer time scales due slow translational diffusion of water, and therefore the intermolecular energy transfer can be attributed to HB bending and stretching modes.

Thereby, the emerging picture thus far is as follows: When the single-cycle THz electric pulse is applied in the x-direction of the pure liquid water, the intramolecular energy transfer from rotation to translation motion of a water occurs less than 100 fms and in the yz- and zy-symmetry. The intramolecular energy transfer process then excites intermolecular energy transfer between two H-bonded water molecules via translation-translation (HB stretching and HB bending modes) motions. Both intramolecular and intermolecular energy transfer pathway is depicted in the Figure 5.12.

Chapter 6

Time-resolved TKE reveals the effects of cations and anions on intermolecular interactions of water

In this chapter, we employ the time-resolved TKE as an intermolecular probe to investigate the ion-induced perturbations of the hydrogen-bonding network of water in aqueous salt systems. For a systematic study, we select salts that contain a strongly charged cation or anion. The respective counterions are chosen to be almost 'neutral'; that is, counterion–water and water–water interaction strengths are comparable[266,267]. The cations of choice are sodium (Na^+) and magnesium (Mg^{2+}) with chloride (Cl^-) as their counterion. The anions are sulfate (SO_4^{2-}) with Na^+ as the counterion, and fluoride (F^-) with Na^+ as its counterion, for higher solubility. We have also investigated the TKE response of $MgSO_4$ solution in which both the cation and the anion are strongly charged. The selected ions have a relatively small electric polarizability, a criterion imposed for reducing potential artefacts emanating from direct contribution of the ion polarizability into the calculated polarizability responses.

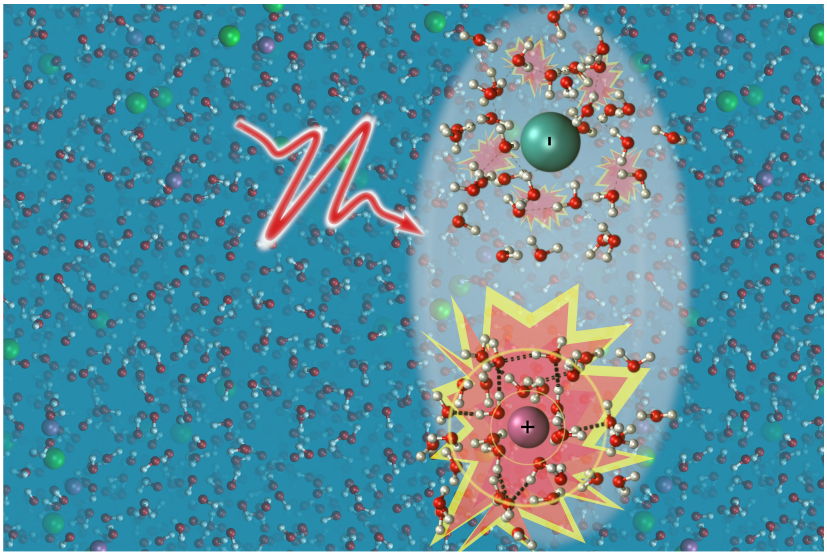

Figure 6.1: **Graphical Abstract:**An intense THz pump pulse induces birefringence in the aqueous salt system. The abstract shows that the cation strengthens the HB network of water, while the anion weakens it.

6.1 Simulation details

In aqueous ionic solutions, a combination of very strong ionic electric fields and field gradients; long-range interactions; and the interplay of polarization and charge transfer effects make the simulations a challenging feat [268]. For instance, ignoring the charge transfer polarization effects, as is done in simple point-charge models, can lead to the erroneous conclusion that all ions are structure makers [269,270]. Even for a simple electrolyte solution such as NaCl, the force fields based on point charges were found unable to reproduce the concentration dependence of important thermodynamic properties under ambient conditions [271]. For the current study, we found that a non-polarizable force field based on a simple point-charge model (the SPC force field) and AMBER parameters fails to reproduce concentration dependence of the THz signal for various aqueous strong electrolyte solutions, as already demonstrated in Chapter 4.

Given the substantial amount of statistical sampling that is required to obtain the THz pulse-induced polarizability anisotropy, we have resorted to non-equilibrium PFFMD simulations using the AMOEBA force field [158]. We have performed PFFMD simulations on pure liquid water and on several ionic solutions such as $MgCl_2$, NaCl, NaF, $MgSO_4$ and Na_2SO_4. Compared to simple point-charge models, AMOEBA assigns to each atom a permanent partial charge, a dipole and a quadrupole moment. Electronic many-body effects are also represented using a self-consistent dipole polarization procedure. Due to the immense electric fields of ions, this explicit treatment of polarization becomes important in order to reproduce the THz Kerr response and its concentration dependence.

In our non-equilibrium MD simulations, the THz external field is directly included in the Hamiltonian that is used to time-propagate the system. The essential idea is that for a system perturbed from equilibrium, all non-equilibrium properties can be computed using equilibrium averaging of dynamical properties, time evaluated under the full (perturbed) dynamics [272,273]. This is in contrast to an equilibrium MD-based approach, where under a linear response assumption, the response is computed as an ensemble-averaged time-correlation function. The direct non-equilibrium approach offers two advantages: First, by simulating a non-equilibrium system, one can visualize microscopically the physical mechanisms that are important to excitation and relaxation, including the distortions of the local molecular structure, the processes of molecular alignment and rotation, and transport processes like the aforementioned transient energy fluxes. Second, the validity of the approach is not limited to the linear response regime. The downside is that one needs perturbation strengths that are huge in order to produce a detectable response that is larger than the statistical noise, but this is becoming less important with the current intensities of laser pulses. Nevertheless, under the employed electric-field strength, obtaining an acceptable signal-to-noise ratio required the simulation of 25000 trajectories for each investigated system.

The analysis of HB strengths is based on equilibrium AIMD simulations of the same systems used in the PFFMD. In AIMD, the electronic structure, which is optimized on the fly at each MD time step, responds adiabatically to the instantaneous local fields, so that—unlike in polarizable force fields—there is no imposed artificial partitioning of the electronic density into separate non-overlapping entities. Charge transfer and polarization effects are naturally accounted for, and finite-size effects are also fully included, so that the strength of the electric field varies at each point of space even on submolecular distances. AIMD simulations of aqueous ionic solutions have been found to give reliable results, provided that dispersion effects are carefully treated [268]. For quantifying the strength of the HBs, we employ ALMO-EDA [31,32,192] within Kohn–Sham density functional theory.

See Chapter 3 and Chapter 2 for more on simulation details and method descriptions.

6.2 Simulation results and discussion

In our TKE MD simulations, due to the action of the pump field polarized along x, we observe a transient difference $\triangle n = n_x - \frac{n_y+n_z}{2}$ between the refractive indices along the x and other two

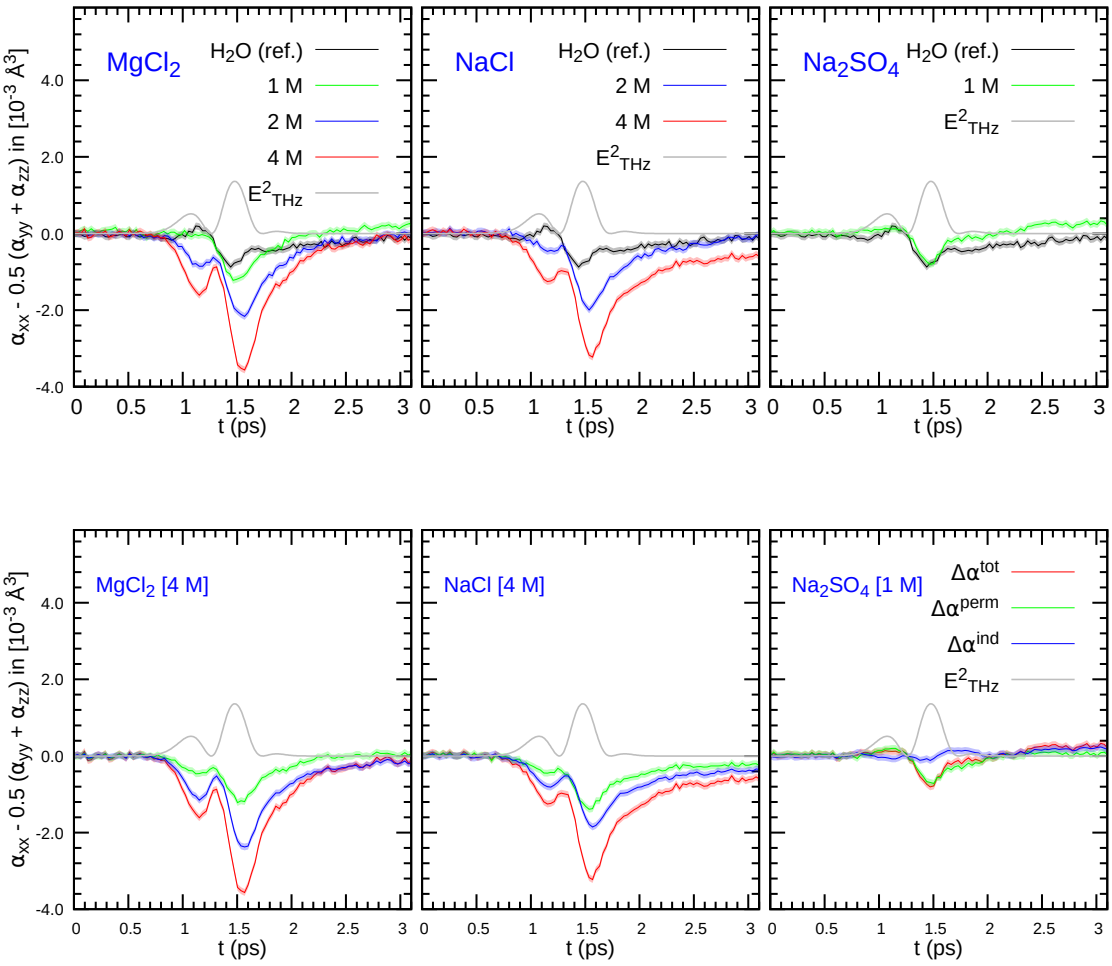

Figure 6.2: Simulated transient polarizability anisotropy of aqueous solutions of $MgCl_2$ (at 1 M, 2 M and 4 M), NaCl (at 2 M and 4 M), and Na_2SO_4 (at 1 M), respectively. In the first row just the total polarizability anisotropy contribution $\triangle\alpha$ is shown, whereas the second row displays the $\triangle\alpha$, single molecule $\triangle\alpha^{\mathrm{perm}}$, collision-induced $\triangle\alpha^{\mathrm{ind}}$ contributions. $\triangle\alpha^{\mathrm{perm}}$ (blue) and $\triangle\alpha^{\mathrm{ind}}$ (green) components of $\triangle\alpha$ (red) are shown only for MgCl2 solution at 4 M, for NaCl at 4 M and for Na_2SO_4 at 1 M, respectively. E^2_{THz} is the square of the THz electric field. The shadowed areas indicate standard errors.

directions y and z. The resulting birefringence is given by [68]

$$\triangle n \propto < \triangle\Pi(t)_{xx} - \frac{\triangle\Pi(t)_{yy} + \triangle\Pi(t)_{zz}}{2} > \tag{6.1}$$

where $\triangle\Pi(t)_{\alpha\beta}$ is the pump-induced change in the collective electronic polarizability tensor element $\Pi(t)_{\alpha\beta}$, α, β are the x,y, and z directional components. Here, Π refers to the liquid phase and contains contributions from interactions/collisions between molecules in the condensed phase. The variation $\triangle\Pi$ can, in principle, be written as a sum $\triangle\Pi^{\mathrm{M}} + \triangle\Pi^{\mathrm{I}}$, whose two contributions arise, respectively, from the intrinsic gas-phase molecular polarizability ($\triangle\Pi^{\mathrm{M}}$) and the intermolecular interactions and collisions ($\triangle\Pi^{\mathrm{I}}$) in the condensed phase [96,97,100].

The $\triangle\Pi^{M}(t)$ characterizes the degree of anisotropy of the unperturbed Π and is usually labelled $\triangle\alpha^{\mathrm{perm}}$ for single molecules. Averaging $\triangle\alpha$ over all molecules according to equation 6.1 yields an expression for single-molecule rotational birefringence $\triangle n_{rot}$ that scales with the degree of molecular alignment with respect to the polarization axis of the THz pump pulse. The averaged $\triangle\Pi^{\mathrm{I}}(t)$ makes another contribution to the transient birefringence and arises directly or indirectly from the pump-induced changes in the collision-induced polarizability. Additionally, THz electric-field-induced ionization and charge separation may contribute to the total polarizability of water [256,257]. However, as demonstrated by Elsässer and co-workers, the latter contributions modulate the isotropic part of the complex dielectric response of water, with negligible impact on its anisotropic response, measured in the TKE experiment [256,257]. Here the $\triangle\Pi^{\mathrm{I}}(t)$ is labelled as $\triangle\alpha^{\mathrm{ind}}(t)$ and computed using DID^{1,2} model. The $\triangle\alpha^{\mathrm{perm}}$ of the ions were modelled using the ionic polarizability parameters from refs. [159,173,210,211], whereas those of water were computed in the gas phase conditions using the parameters in Table 3.1.

The calculated THz electric-field-induced polarizability anisotropies $\triangle\Pi(t)$ of $MgCl_2$ (at 1 M, 2 M and 4 M), NaCl (at 2 M and 4 M), and Na_2SO_4 (at 1 M) are shown in Figure 6.2. The results are obtained from the molecular dynamics (MD) trajectories, using the atomic multipole optimized energetics for biomolecular applications (AMOEBA) polarizable force field and the extended-dipole/induced-dipole (XDID) model as described by Torri [95], but modified to include the second hyperpolarizability. Interestingly, relative to pure water, the $\triangle\Pi(t)$ amplitude of $MgCl_2$ is enhanced, while that of Na_2SO_4 is reduced. The amplitude drop of the Na_2SO_4 solution is modest and not as large as that observed in the experiment, likely due to limitations originating from the employed XDID model or the employed force field. The calculated $\triangle\Pi(t)$ for NaCl (at 2 M and 4 M) replicates the behaviour of $MgCl_2$.

As demonstrated in Chapter 5, when the single-cycle THz electric pulse is applied in the x-direction of the pure liquid water, the intramolecular energy transfer from rotational to translational motion of water occurs in yz- and zy-symmetry. The intramolecular energy transfer process then excites intermolecular energy transfer between two H-bonded water molecules via translation-translation (HB stretching and HB bending) motions. This is how the THz energy pumped into the rotational degrees of freedom of water is transferred into the translational motion of the neighbouring water molecules [41,44] in liquid water. In a previous paper [44], we showed that the decay of the TKE signal's tail reveals the relaxation of the translational motion of water molecules, most likely that of the HB bending mode due to its spectral proximity to the excitation frequency. Therefore, given the initial excitation of the rotational dynamics of water with the THz pump pulse, the rotation-to-translation energy transfer causes a coherent increase in the rate of the collisions between water molecules, which can be resolved as a change in the refractive index of the liquid via $\triangle\Pi^{\mathrm{I}}(t)$.

In light of the TKE response of pure water, the ion-induced enhancement/weakening of the TKE signals may indicate underlying changes in the strength of the intermolecular water–water hydrogen-bonding interactions, by which the rotational–translational coupling is modified. To examine the soundness of this proposition, we first decompose $\triangle\Pi(t)$ into the contributions $\triangle\Pi^{M}(t)$ and $\triangle\Pi^{\mathrm{I}}(t)$. The corresponding results for $MgCl_2$ at 4 M, NaCl at 4 M and Na_2SO_4 at 1 M are shown in Figure 6.2. Remarkably, while in $MgCl_2$ and NaCl solutions the collision-induced polarizability anisotropy

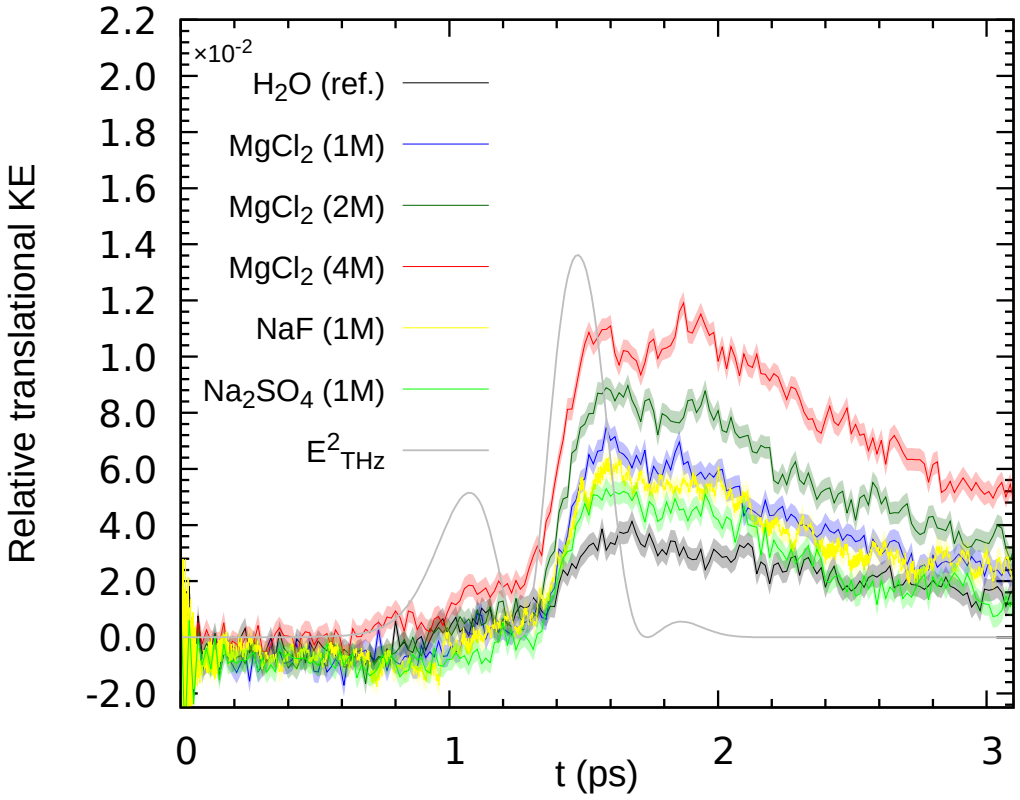

Figure 6.3: Temporal evolution of the ratio of the molecular translational KE to the total instantaneous KE of aqueous ionic solutions of MgCl2 at 1 M (blue), 2 M (dark green) and 4 M (red), Na2SO4 at 1 M (light green), NaF at 1 M (yellow) and pure liquid water (black), obtained from polarizable force field MD (PFFMD) simulations. The deviation of the ratio from the equilibrium value of 1/3 is plotted, so that a positive value indicates a relative increase in the respective KE contribution in comparison to an equilibrium (equipartitioned) distribution. Note that for the strong cation Mg^{2+}, the amplitude of the perturbation of the KE distribution substantially increases in comparison to the strong anion, SO_4^{2-}. E^2_{THz} is the square of the THz electric field. The shadowed areas indicate standard errors.

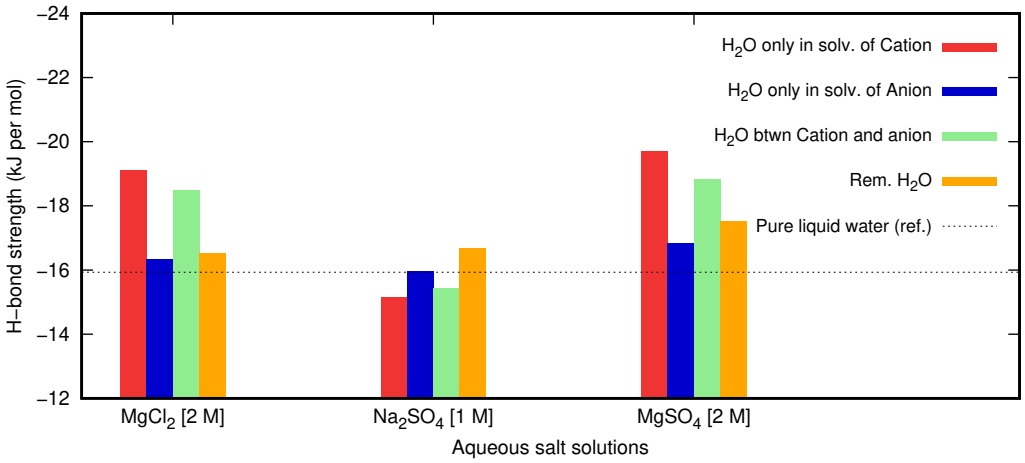

Figure 6.4: HB strength from equilibrium trajectories of AIMD simulations are obtained for every water molecule in the system, classified into four disjoint categories: from left to right, a water molecule in the solvation shell of a cation (red), an anion (blue), a water molecule shared between a cation and an anion (green) and the remaining bulk-type molecules (orange). For water molecules in the first solvation shell of an ion, the HBs correspond to those between water molecules in the first and second solvation shells of that ion. Notably, while the water–water HB strength between the first and second solvation shells of cations increases, it decreases around anions. We have used a simple geometric definition of a hydrogen bond, with an O–O distance less than 3.5 Å and an angle less tha 30^o.

$\triangle\Pi^{\mathrm{I}}(t)$ makes the dominant contribution to the total polarizability anisotropy, its contribution in the Na_2SO_4 solution is minor.

Along the same line, the increase/decrease of the collision-induced polarizability may also be observed in the KE of the translational motion of water molecules. Thereby, we calculate the transient excess translational KE(t) of water molecules in $MgCl_2$, NaF and Na_2SO_4 solutions. As shown in Figure 6.3, the translational KE(t) of water molecules in $MgCl_2$ solutions is substantially enhanced relative to pure water. The KE(t) of the water molecules in NaCl solutions also shows a similar trend. For the Na_2SO_4 and NaF solution, although the expected decrease in the translational KE(t) is not observed, its amplitude is not as large as that of the $MgCl_2$ solution at the same concentration. This parallels our previous observation that the employed parameterization of the polarizable force field underestimates the effects of Na_2SO_4 in the polarizability calculations.

To connect the latter findings with the local intermolecular interactions in water, we resort to equilibrium AIMD simulations and calculate the water–water HB strength. For quantifying the strength of the HBs, we employ ALMO-EDA [31,32,192] within Kohn–Sham density functional theory. The HBs are categorized into four disjoint classes: those between the first and second solvation shells of an anion; the same for cations; those involving one water molecule, which is simultaneously shared in the first solvation shell of an anion and a cation; and those between the remaining bulk-type water molecules, meaning that these HBs are between two water molecules, both of which are not in the first solvation shell of an ion.

As shown Figure in 6.4, by comparing the water–water HB strength around ions with that of the bulk-type water, the following conclusions can be drawn: In $MgCl_2$ solution, the Mg^{2+} ions with their high charge density lead the water–water HBs in their immediate surroundings to be 2-3 kJ/mol stronger than more distant HBs. This is in line with a recent experimental study by Shalit et al. denoting the ability of strong cations such as Mg^{2+} to structure the hydrogen-bonding network of water [274,275]. On the other hand, in the Na_2SO_4 solution, the SO_4^{2-} ions show an opposite trend, namely the neighbouring HBs are slightly weaker. Along the same lines, by analysing the changes in the OH-stretch vibration frequency of water molecules in the first and second solvation shells of

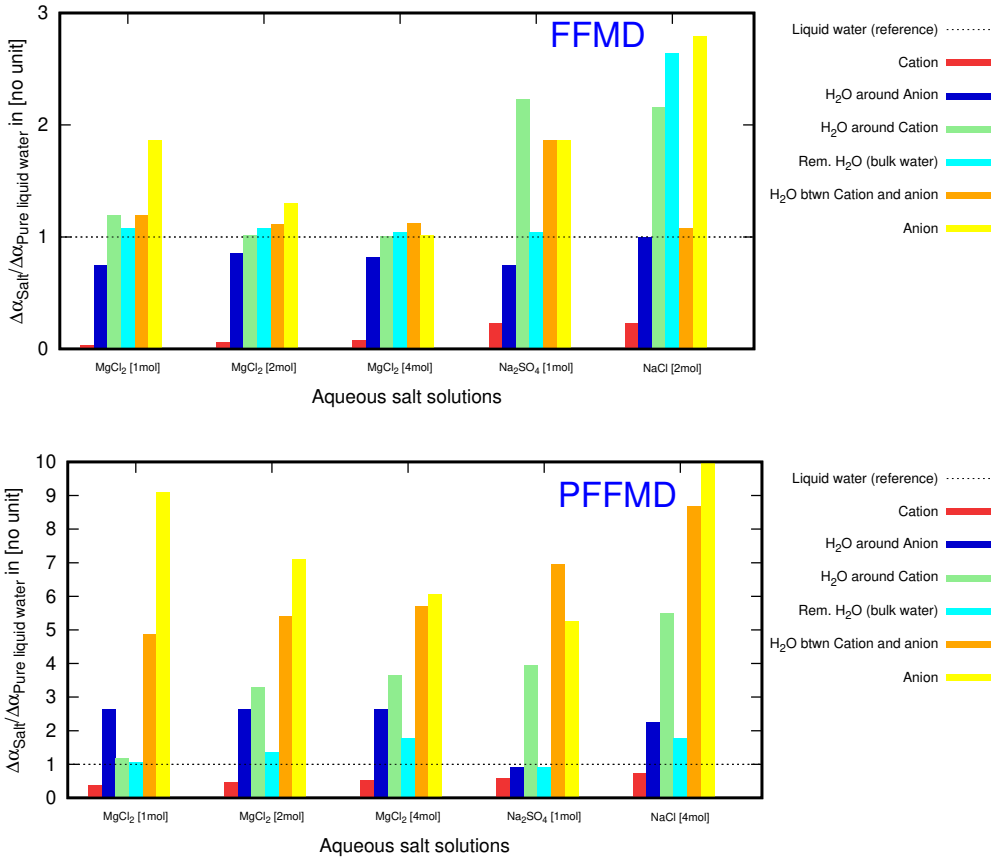

Figure 6.5: The negative maximum intensity of TKE-induced polarizability anisotropy normalized to pure liquid water for different classified molecules in several aqueous salt systems. Types of molecule: cations, anions, water around cation, water around anion, water between cation and anion, and all remaining water molecules as bulk water. The time in which the water molecule type probed is 1.5 ps. The polarizability anisotropy is calculated via the first- and second-order molecular hyperpolarizability enhanced DID model (DID^{1,2}). The numbers reported in this figure are per molecule. The systems were simulated using polarizable (top panel) and non-polarizable (bottom panel) force fields. For the sake of comparison, the non-polarizable (SPC/AMBER) simulation was performed with the same computational details as the polarizable (AMOEBA) simulation.

CO_3^{2-}, Yadav et al. reported the weakening of the water–water hydrogen-bonding strength around CO_3^{2-} (ref.[276]). Previous ab initio calculations on solvated clusters have also shown this increase (decrease) of the HB strength between the first and second solvation shells of cations (anions) [277].

Thereby, the emerging picture thus far is as follows. Ions influence the water–water intermolecular HB strength between the first and second solvation shells. Highly charged cations strengthen this HB interaction and highly charged anions weaken it. As a result, the first solvation shell of strongly charged cation (anion) undergoes intramolecular energy transfer from rotational to translational motion very faster (very slower) compared to pure liquid water. The rapid (slow) intramolecular energy transfer mechanism then excites the intermolecular energy transfer between the first and second solvation shells, respectively. Basically, the ion-induced change in the water–water interaction strength alters the intermolecular coupling between the rotational and translational degrees of freedom. As such, the THz energy initially deposited into the intermolecular rotational motion of water funnels into the translational motions, with the efficiency determined by the ionic content of the solution, and influences the collision-induced contribution to polarizability anisotropy, which is captured in our

TKE experiment and simulations[44,121].

In light of these results, the linear concentration dependence of the TKE signal amplitude in strong cationic solutions, holding even at elevated concentrations, may now be understood. In particular, in the extreme case of the $MgCl_2$ solution at 4 M, all water molecules are consumed in the first solvation shells of ions; hence, there is virtually no free water to form a second hydration shell for each ion[278]. Nevertheless, we still observe a linear trend in the concentration dependence of the calculated, quantities. We believe that in such solutions, the role of Cl^- in water–water interactions is critical. The water–Cl^- interaction strength is comparable with that of water–water in bulk (Fig. 6), and the dynamics of water molecules solvating Cl^- are minimally perturbed by Cl^- (ref.[279]). Thereby, there are still abundant water molecules in the system whose dynamics and HB strengths resemble that of bulk, by which the second solvation of Mg^{2+} at high concentrations can be formed.

To better understand the trend of TKE polarizability anisotropy response observed in terms of concentration and charge density, we separated the overall polarizability anisotropy for each type of molecule in the aqueous ionic solutions of $MgCl_2$ (1M, 2M, 4M), Na_2SO_4 (1M), and NaCl (1M, 2M), respectively. The molecular types are cations, anions, water around cation, water around anion, water between cation and anion, and all remaining water molecules as bulk water, respectively. The polarizability anisotropy for all these molecular types is shown in Figure 6.5. Both polarizable and non-polarizable force fields show that the polarizability anisotropy for cations is negligible, whereas it is very high for anions for all the simulated systems. This is to be expected, since cations are less polarizable than anions[173] However, as the salt concentration rises, the anion's polarizability anisotropy decreases while the cation's polarizability anisotropy increases slightly. The effect of ions on water in the first solvation shell can be understood from the polarizability anisotropy of water molecular types. Our results show that cations such as Mg^{2+} and Na^+ increase the polarizability anisotropy of water, while the highly charged anion as SO_4^{2-} suppresses it. However, the water in the middle of anions and cations exhibit stronger anisotropy than pure liquid water. Moreover, since the population of water between cations and anions are very high at the high salt concentrated aqueous solution, this species is the primary contributor to the anisotropy results. The anisotropy of bulk water is similar to that of pure liquid water, but as the salt concentration increases, the anisotropy increases. All these findings clearly suggest that the polarizability anisotropy of aqueous salt system is mainly governed by water specied shared between cation and anion, as well as bulk water.

We have further examined the THz-electric-field-induced molecular alignment/orientation response of the water molecules in pure H_2O, $MgCl_2$ (2 M), Na_2SO_4 (1 M) and $MgSO_4$ (2M) aqueous systems, as shown in Figure 6.6 (top). The inclusion of ions clearly leads to a apparent decrease in the alignment of water molecules to the field in comparison with the pure water. The alignment of the water molecules decreases in the order: pure H_2O, Na_2SO_4, $MgCl_2$, $MgSO_4$. Unlike simulated transient polarizability anisotropy, we don't observe any linearity with respect to the charge density.

To study the particular responses of water molecules around anions and cations, we have also separated the alignment responses, which come from the water molecules in the first solvation shell of the anions and cations, between them, from the remaining water altogether, this is shown in Figure 6.6 (bottom). The water molecules away from the ions exhibited stronger responses to the field than those close to the ions, and are in slightly close proximity to that of pure water. Since anions naturally have the ability to form H-bonding network in the place of water molecules, the water molecules around them strongly align and realign to the field as observed in the bulk water. Cations, on the other hand, lead to a strong intermolecular coupling because of their strong Coulombic interaction with the lone pair electrons of oxygen atoms in water molecules[280,281]. This restrains the alignment of the water molecules around them to the field unlike anions. However, water molecules around weakly charged or low charge density Na^+ cation almost align and realign as the anions. whereas the strongly charged or highly charged density Mg^{2+} cation restrain the alignment response of the water molecules. This result is in agreement with the recent work of Head-Gordon and Havenith Co-workers[66]. It is also interesting to report that the water molecules in $MgSO_4$ orient weakly to the field, while its cation

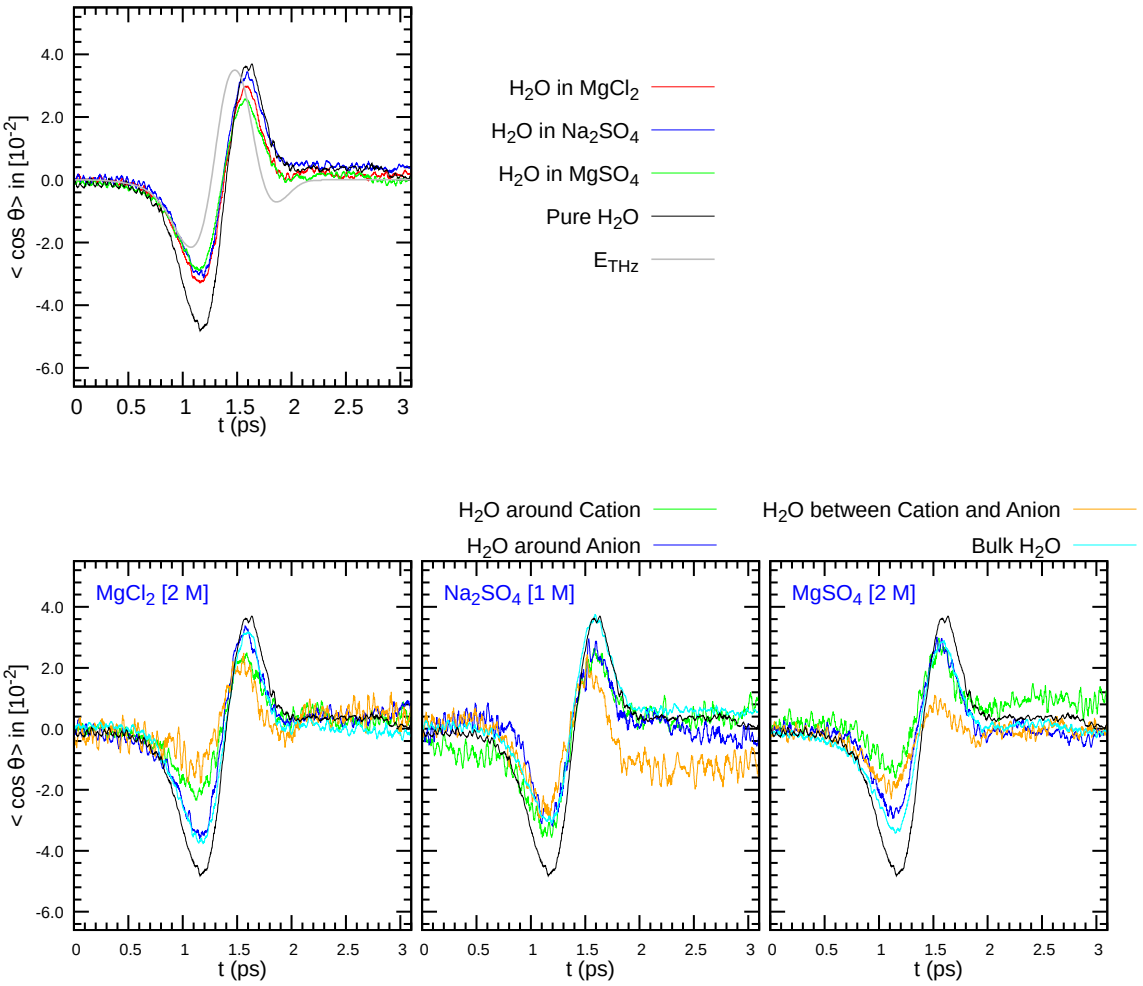

Figure 6.6: The THz-pulse-induced-orientational dynamics/water bisector of water molecules in pure H_2O, $MgCl_2$ [2M], Na_2SO_4 [1M] and $MgSO_4$ [2M]. In the first row just the total contribution, i.e., the water bisector for all water molecules is shown, whereas the second row displays the water bisector for all four disjoint categories. E_{THz} is the THz electric field. For these calculations, THz-pulsed-AIMD trajectories were used.

and anion combine with Cl^- and Na^+ cause the water molecules orient much stronger. This can be attributed to the non-additive and independent nature of ionic effects in water [282,283].

Chapter 7

Impact of intermolecular vibrational coupling effects on the sum-frequency generation spectra of the water/air interface

In this chapter, we have examined the impact of intermolecular vibrational coupling effects of the O-H stretch modes, as obtained by the surface-specific velocity-velocity correlation function approach, on the simulated sum-frequency generation spectra of the water/air interface. Our study shows that the inclusion of intermolecular coupling effects within the first three water layers, i.e., from the water/air interface up to a distance of 6 Å towards the bulk, is essential to reproduce the experimental SFG spectra. In particular, we demonstrate that these intermolecular vibrational contributions to the SFG spectra of the water/air interface are dominated by the coupling between the SFG active interfacial and SFG inactive bulk water molecules.

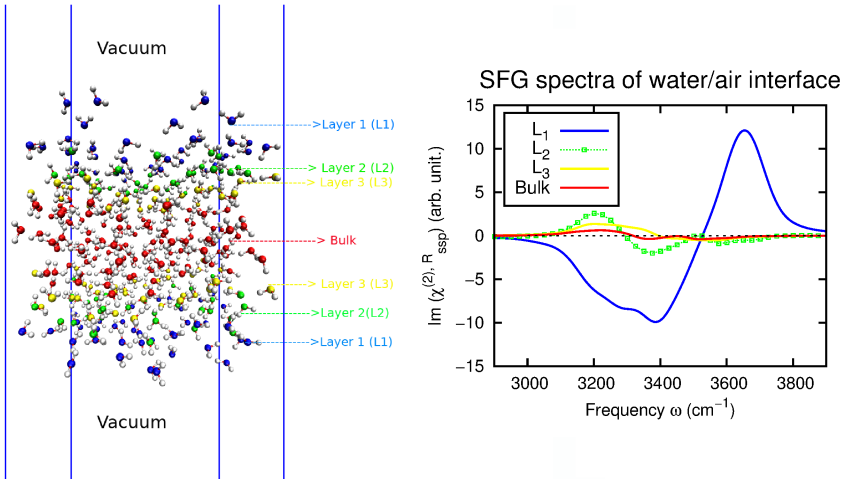

Figure 7.1: **Graphical Abstract:** Left Figure is the model of the simulated water/air interface. The bulk like water molecules are in the middle are shown in red, whereas the surface molecules, which are at the core of our investigations are, depending on the layer where they are located, colored in blue, green and yellow respectively. Right figure is the simulated SFG spectra of water/air interface for the represented water layers.

7.1 Introduction

The characterization of liquid water at aqueous interfaces is complex but essential for understanding physicochemical, environmental and biological processes such as organic catalysis on water [14], protein folding [15], atmospheric chemistry [16], electrochemical processes in aqueous batteries [17] and the function of biological membranes, as well as membrane proteins [18]. Among the various aqueous interfaces, the water/air interface is of special interest since it represents a well-studied model system for aqueous interfaces in general [55,284,285], which is why it is a good starting point for the present investigation.

Surface-sensitive vibrational sum-frequency generation (SFG) is presently one of the widely employed technique to characterize molecules directly at liquid interfaces [57,58,286,287]. The surface-sensitivity is due to the fact that it does not provide a signal in centrosymmetric or isotropic bulk media and is only active at interfaces or surfaces, where the symmetry is broken. In recent years, this technique has been very successful in providing vibrational spectra for various interfacial systems [54,288–292]. Among those, the water/air interface has been the most intensively studied system, both experimentally [53,56,292–298] and theoretically [58,292,297–308]. However, the interpretation of the experimental SFG spectra of the water/air interface in the spectroscopic range between 3000 and 3600 cm^{-1} is still a matter of great debate [53,58,294,297,302,306,308–310]. In this regard, theoretical SFG simulations have been employed to assist the interpretation and assignment of the O-H stretch vibrational features in the experimental SFG spectra [58,288,292,299,302,308,310,311]. Typically, these simulations include intra- and intermolecular vibrational couplings of O-H stretch modes [31,312–314], which strongly affects the speed and time scales of spectral diffusion and alters the SFG response of the O-H stretch frequency [292,294]. Yet, in practical SFG simulations, only the intramolecular vibrational coupling effects are explicitly included, while the intermolecular vibrational couplings are generally neglected [58,300,315,316], or just partially treated using a short correlation cutoff [299]. An alternative approach to compute SFG spectra is via the dipole moment-polarisability (μ-α) time-correlation function (TCF) [297,300,302], which however is computationally rather expensive since it requires relatively long trajectories (several ns) to reach numerical convergence [58]. This convergence issue has limited the usage of computationally expensive quantum-mechanical *ab-inito* and path-integral molecular dynamics (MD) simulations to obtain and interpret SFG spectra [105,252,253,317]. Nevertheless, recently a few studies have incorporated sufficiently long MD trajectories to study both of these coupling effects [58,292,299,302,303]. In particular it has been shown that intramolecular coupling effects gives rise to the vibrational O-H stretch response in the SFG spectra, while the intermolecular couplings induces a red-shift in the H-bonded O-H stretch response. Moreover, it has been shown that the intermolecular coupling induced SFG features in the spectra are in good agreement with experimental SFG spectra [292,299,302].

In the present study, the surface-specific velocity-velocity correlation function (ssVVCF) method, which was recently developed by some of us [58], has been employed. The chief advantage of this approach is the up to an order of magnitude faster convergence than the usual μ-α TCF scheme. Using this approach allows us to obtain well converged SFG spectra of the water/air interface in order to assess the impact of intermolecular coupling effects. For the purpose to demonstrate the significance of intermolecular couplings in the SFG simulations, the obtained SFG spectra are compared with experimental measurements. Furthermore, we have also employed an instantaneous layer analysis to separate the vibrational contributions arising from interfacial water molecules and to obtain unambiguous contributions to the overall SFG spectra. This instantaneous layer analysis has also allowed us to study intermolecular coupling effects that occur between the O-H stretch modes of the same water layer, as well as in different water layers of the system. Finally, we have presented the correlation between interface water structure and their SFG signal to better understand the water/air interface.

The remaining of this chapter is organized as follows. The computational details including the interface definition, MD and the ssVVCF formalism are described in section 7.2. Section 7.3 contains

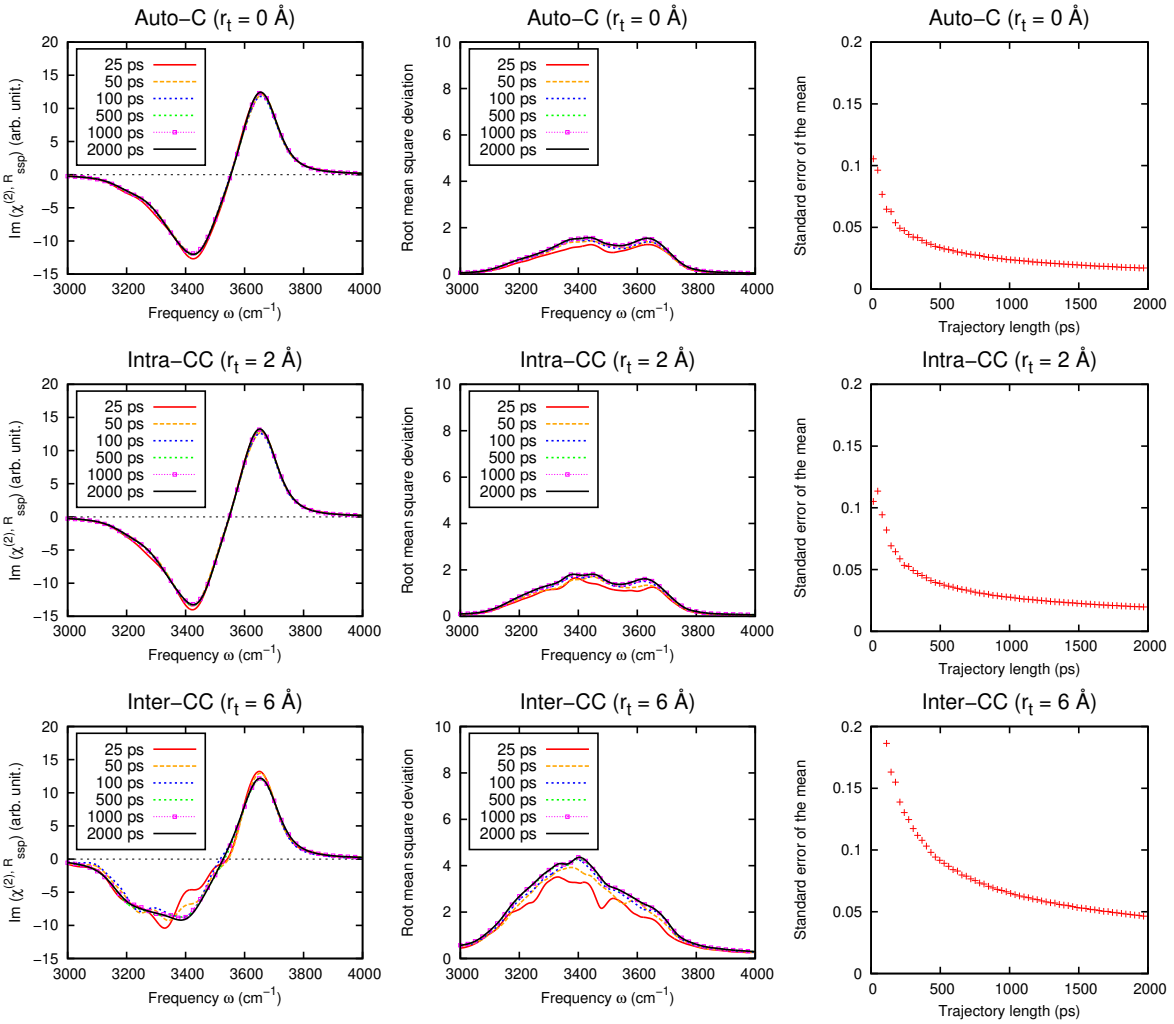

Figure 7.2: Simulated O-H stretch SFG spectra as a function of trajectory lengths (left panel), root mean square deviation within the SFG spectral region between 3000 - 4000 cm^{-1} (middle panel) and standard error of the mean (right panel). In the first row just the Auto-C contribution is shown, whereas in the second row the Intra-CC correlation term is added and in the third row also the Inter-CC contribution, respectively.

our simulation results and discussion, which is followed by a summary in section 7.4.

7.2 Computational Details

7.2.1 Partially Adiabatic Centroid Molecular Dynamics Simulations

A total of 250 statistically independent partially adiabatic centroid MD (PA-CMD) simulations of the water/air interface were performed at ambient conditions. In the PA-CMD scheme, the effective masses of the individual replicas that makes up the closed p-bead ring-polymers, which are isomorphic to the original quantum particles [318,319], are adjusted so as to shift the spurious oscillations beyond the spectral range of interest [320]. Specifically, the elements of the Parrinello-Rahman mass matrix are chosen so that the internal modes of the ring-polymer are shifted to a frequency of

$$\Omega = p^{p/p-1}\frac{k_B T}{\hbar}, \tag{7.1}$$

which allows for similar integration timesteps to be used than in conventional MD simulations [321].

Throughout the flexible q-TIP4P/F water model of Habershon et al. [320], augmented by the explicit three-body (E3B) interactions proposed by Skinner and coworkers [322], had been employed. Nevertheless, we find it important to note that the present flexible, but fixed point-charge water model is neither polarizable nor able to mimic cooperativity effects and chemical reactions that may take place in liquid water. Moreover, to be precise, we would like to emphasize that the E3B scheme was originally parametrized for the rigid TIP4P/2005 force-field of Abascal and Vega [323], which forms the basis and is hence very closely related to the used flexible q-TIP4P/F water model [320]. The simulated water slab consisted of 343 water molecules in an orthorhombic simulation cell of lengths 21.75 Å × 21.75 Å × 108.75 Å, respectively. To mimic the water/vapor interface, the supercell approach was employed by adding a large 43.5 Å long vacuum portion on both sides of the system along the non-periodic z-direction and applying periodic boundary conditions. Short-range interactions were truncated at 9 Å, whereas the Ewald summation technique was employed to treat the long-range electrostatic interactions. To explicitly consider nuclear quantum effects (NQE) in a computational efficient way, the ring polymer contraction scheme was used with a cutoff value of $\sigma = 5$ Å to reduce the electrostatic potential energy and force evaluations to a single Ewald sum, in order to speed up the calculations [320]. This is to say that 32 ring-polymer beads were employed to converge all relevant properties [122,252,320,324–327], while the computationally expensive part of the electrostatic interactions were contracted to the centroid only. In all simulations, using a discretized integration timestep of 0.1 fs, the system was first equilibrated 10 ps in the canonical ensemble, before microcanonical ensemble averages were computed over the following 8 ps, resulting in a total statistics of 2 ns to compute the present SFG spectra.

7.2.2 Interface definition

In order to decompose the eventual SFG spectra into its contributions of the different interfacial water layers, we first determine all water molecules that belong to the interfacial region of the water/vapor interface within all our trajectories and their corresponding residence times. Several techniques [328–331] and definitions [332–334] have been developed in the past to define the interfacial region and to identify the interfacial molecules. Here, the so-called Identification of the Truly Interfacial Molecules scheme is employed to unambiguously identify the water molecules that are truly located at the boundary of the two different phases at every timestep [328,330,331]. This technique determines the instantaneous interfacial water molecules by moving a probe sphere of a given radius R_{ps} along a set of lines that are perpendicular to the plane of the interface. All molecules hit by the probe spheres are considered as interfacial water molecules, whereas the position of the spheres when they are in contact with the interfacial molecules is defined to be the location of the instantaneous interface. Moreover, this technique also permits to unambiguously identify the molecules forming the successive (second, third, etc.) water layers by repeating the same procedure without the already identified molecular layer [328,330,331]. Throughout the present work, a probe sphere radius of $R_{ps} = 2$ Å has been used to identify the molecules in the topmost (L_1), second (L_2) and third (L_3) layer of water, whereas all remaining molecules are considered to be the bulk water.

7.2.3 SFG spectra calculations

The resonant term of the second order non-linear susceptibility is calculated using the ssVVCF formalism, pioneered by Nagata and Co-workers [58]. The equation used to calculate the resonant term

in this work is given by

$$\chi^{(2),R}_{abc}(\omega) = \begin{cases} \dfrac{Q(\omega)}{i\omega^2} \displaystyle\int_0^\infty dt\ e^{-i\omega t} \times \left\langle \sum_{i,j} g_t(r_{ij}(0); r_t)\ \dot{r}^{\mathrm{OH}}_{c,i}(0) \dfrac{\dot{\vec{r}}^{\mathrm{OH}}_j(t) \cdot \vec{r}^{\mathrm{OH}}_j(t)}{\left|\vec{r}^{\mathrm{OH}}_j(t)\right|} \right\rangle, & \text{if } a = b \\ 0, & \text{otherwise,} \end{cases} \tag{7.2}$$

where $r_{ij}(t)$ is the distance between the center of masses of O-H groups i and j at time t, whereas $g_t(r_{ij}; r_t)$ is the function to control the cross-correlation terms with the cross-correlation cutoff radius of r_t. The intramolecular distances and velocities of O-H group j at time t are denoted as $r^{\mathrm{OH}}_j(t)$ and $\dot{r}^{\mathrm{OH}}_j(t)$, respectively. The quantum correction factor $Q(\omega)$ was taken from Ref.[58] and the Hann window function was applied for the Fourier transformation of the TCF. Even though non-Condon effects are neglected, all intramolecular coupling effects are included in terms of the auto-correlation (Auto-C) and intramolecular cross-correlation (Intra-CC) function, whereas the intermolecular coupling is included using the intermolecular cross-correlation (Inter-CC) function of the O-H stretch modes. Nevertheless, it is important to realize that within this formalism, the amount of correlation is increasing by enlarging r_t. For example, when $r_t = 0$ Å, only the auto-correlation of O-H stretch modes is included. However, increasing r_t to 2 Å entails the correlations within a water molecule, that is the auto-correlation and the intramolecular cross-correlation, but no intermolecular cross-correlation. However, only for r_t much greater than 2 Å, all three three correlation contributions are explicitly taken into account. Although in the latter case, the present ssVVCF technique is generally more accurate and computationally much cheaper than the conventional μ-α TCF approach[58], it still requires rather long trajectories to obtain unbiased SFG spectra.

Hence, in this work, we first assessed the necessary trajectory length to get unbiased SFG spectra with minimal variance as quantified by the standard error of the mean (SEM). The spectra, which are shown in Fig. 7.2, are computed for three different cutoff radii ($r_t = 0$ Å, 2 Å and 6 Å) to demonstrate the impact of r_t on the eventual result and on the required minimal trajectory length. We found that for $r_t = 0$ Å and 2 Å respectively, a trajectory length of 100 ps is good enough to converge the statistical uncertainties of the corresponding SFG spectra. Therefore, relatively short trajectories are sufficient for a converged SFG calculation with auto-correlation and intramolecular cross-correlation terms. But, in the case of $r_t = 6$ Å, the SEM is very slowly decaying leading to the oscillations that are visible in the spectral range 3000 - 3600 cm^{-1}. This is to say that for large values of r_t, the convergence with respect to the trajectory is slower, which is why at least 500 ps are required. In other words, the convergence within the present ssVVCF methods, is highly dependent on the intermolecular cross-correlation term. However, in contrast to previous works[58], which have not been able to observe any advantage using larger values of r_t, we find that even though the convergence of the ssVVCF method is somewhat slower, the results can be nevertheless systematically improved by increasing r_t at moderate trajectory lengths, given that the window length to compute the TCF is chosen be small. Based on these results, all following SFG calculations were based on a trajectory length of 200 ps, except for the calculations with $r_t >> 2$ Å, where 1000 ps was used in order to achieve well converged SFG spectra. Throughout a window length of ∼1 ps was employed during which the set water molecules were kept fixed. As can be seen in Fig.7.3 and 7.4, this does not lead to any bias in the eventual SFG spectra.

In addition, we have also studied the impact of the intermolecular coupling effect on the SFG spectra of water/air interface by varying r_t from 3 to 10 Å, as shown in Fig. 7.5. By visual inspection it can be seen that there are substantial differences when increasing r_t up to 3 Å, and smaller ones between 4 to 10 Å. However, a closer inspection of the negative peak position, which is shown in the inset of Fig. 7.5, shows that the latter is not quite converged until r_t is at least 6 Å. This is to say that a much larger value of r_t than previously suggested is necessary to explicitly include all relevant intermolecular vibrational coupling effects within the SFG spectra. Hence, in this work, we set $r_t = 6$ Å, which is also in agreement with the distance of water molecules in the third layer and

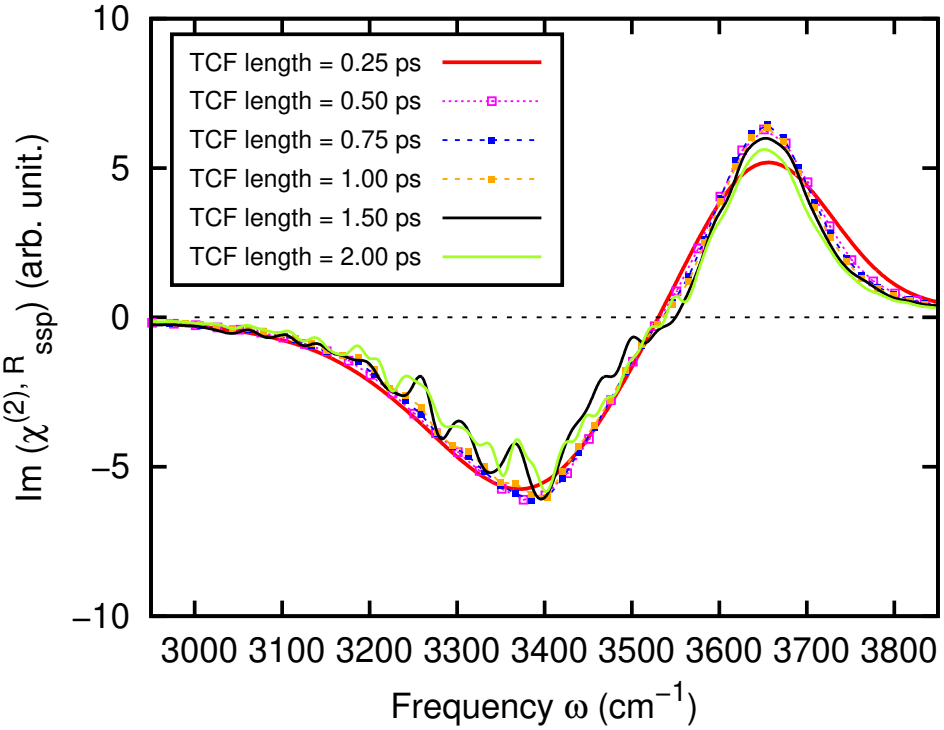

Figure 7.3: Simulated O-H stretch SFG spectra of the water/air interface, as a function of time correlation function length.

the instantaneous water surface.

The SFG spectra are computed using the source code[335] that we developed.

7.3 Simulation results and discussion

7.3.1 Effects of intermolecular vibrational coupling of OH stretch modes on the SFG spectra of water/air interface

The time-averaged density profiles of the identified water layers (L_1 - L_3) and the full water/air interface system as a function of z-coordinate are shown in Fig. 7.6. Beyond L_3, the particle density $\rho(z)$ resumes its original bulk value, which is why we simply denoted is as bulk water. The interface is usually defined as the region where the density varies from 95% to 5% of the bulk density, whereas the position so called Gibbs dividing surface is defined as the location where the average density equals 50% of the bulk density[253]. According to this definition, the thickness of the interface and the location of the Gibbs dividing surface are $\sim$ 3.7 Å and 10.65 Å, respectively. However, contrary to the former, the latter definition defines just the averaged instead of the instantaneous interface. As a consequence, it does not take water molecules that dynamically switches between L_1, L_2, and L_3 at different times explicitly into account, as opposed to the instantaneous interfacial profiles of Fig. 7.6. Therein, the density profiles of the individual layers follow the Gaussian distribution, whose average location and width can be easily characterized by using their peak position and full width at half-maximum that are ($\pm$ 9.6 Å, 2 Å), ($\pm$ 7.5 Å, 2 Å) and ($\pm$ 5.4 Å, 2 Å) for the (center position, width) of layers L_1, L_2, and L_3, respectively. Hence, the identified first water layer extends from the instantaneous interface to a distance of 2.0 Å towards the bulk, whereas the second water layer ranges from 2.0 Å to 4.0 Å and the third water layer from 4.0 to 6.0 Å from the instantaneous interface,

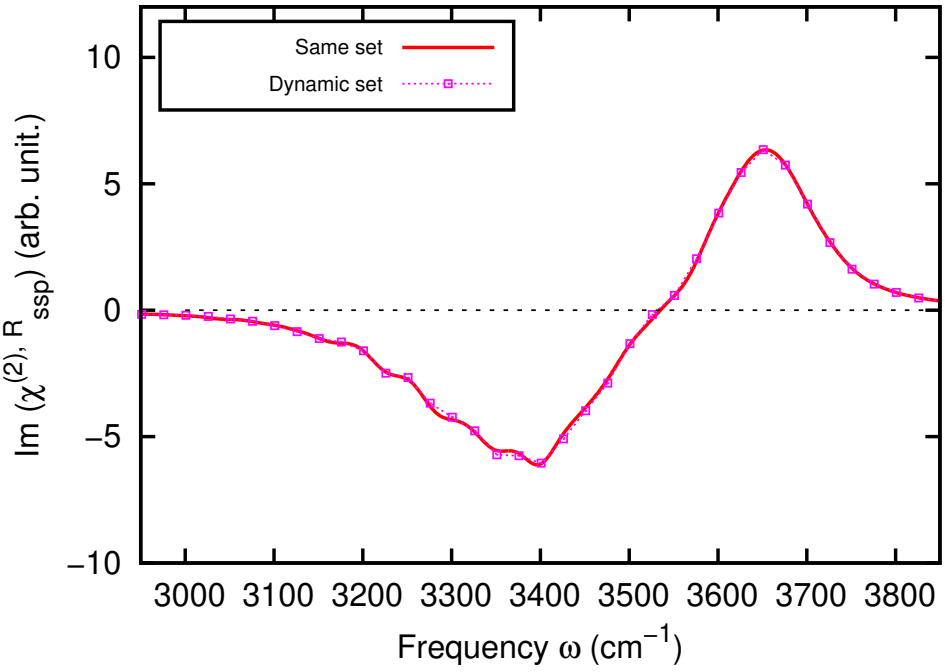

Figure 7.4: Simulated O-H stretch SFG spectrum of the water/air interface, where the same fixed set of water molecules within the distance r_t are used. For comparison, the SFG spectrum, where the set of water molecules within the distance r_t is dynamically recomputed for each MD step is shown.

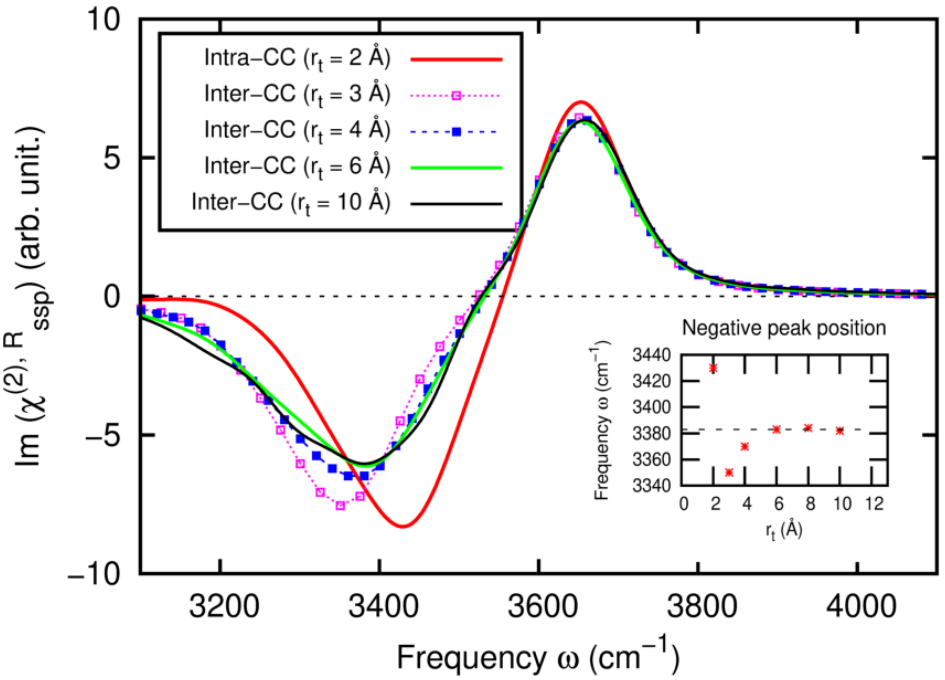

Figure 7.5: Simulated O-H stretch SFG spectra of the water/air interface, as a function of correlation cutoffs r_t. The inset shows the peak position of the negative peak as a function of r_t.

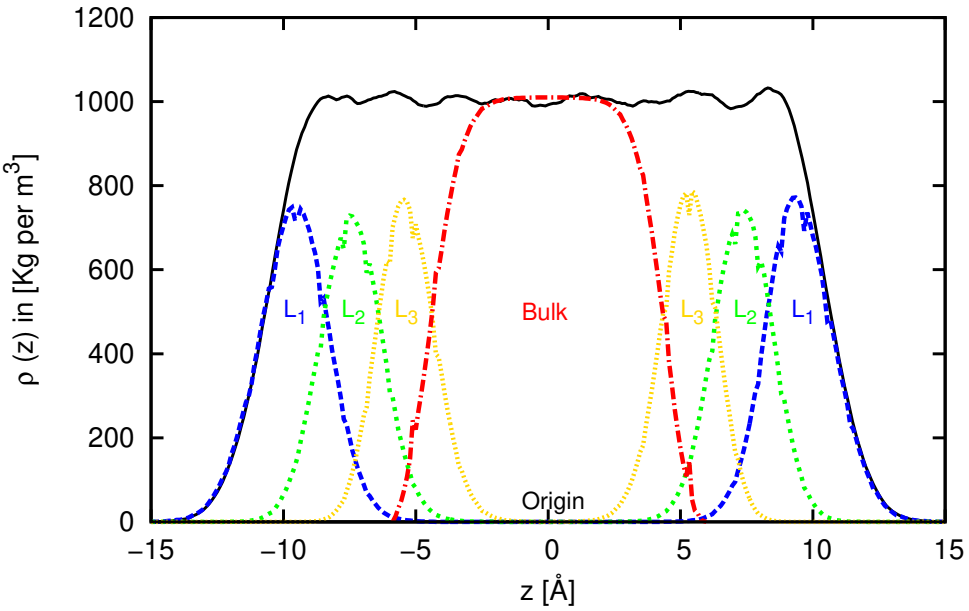

Figure 7.6: Density profiles of the identified instantaneous water layers (L1 - L3) as a function of the z-coordinate, as well as of the full water/air interface.

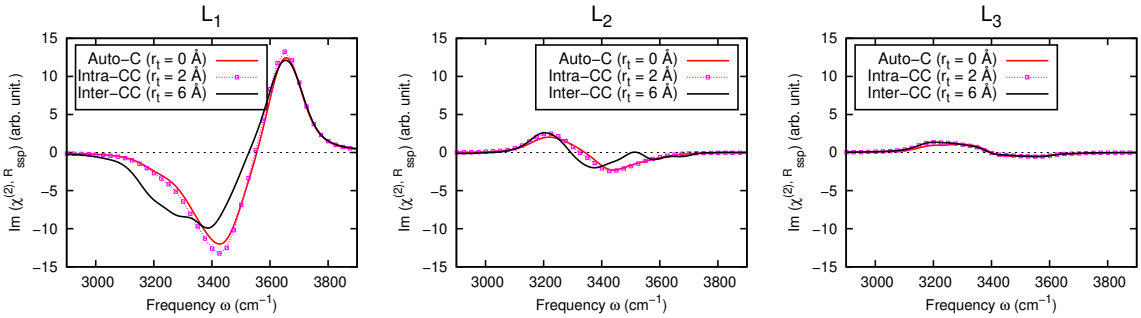

Figure 7.7: Simulated O-H stretch SFG spectra as a function of r_t for L_1 (left panel), L_2 (middle panel) and L_3 (right panel).

respectively.

For the purpose to determine the interfacial thickness of the water/air interface based on the SFG selection rule, we computed the SFG spectra individual as a function of water layer, as shown in Fig. 7.7. The SFG signal is detected from the water molecules in the top most layer (i.e., the sum of L_1 and L_2) only that extend from the instantaneous interface to a distance of 4 Å towards the bulk. Beyond 4 Å, the intensity of the signal becomes almost zero as a result of the centrosymmetrical orientation of the corresponding water molecules that is why we consider the interfacial thickness of the water/air interface to be 4 Å, which is very close to the value of the previous MD simulations [62,63,252,253]. Therefore, only the water molecules in the first two layers are considered as the interfacial molecules from this point on.

The simulated O-H stretch SFG spectra of the interfacial molecules at the water/air interface are shown in Fig. 7.8. In these spectra, we observe a sharp positive peak centred at ~ 3650 cm^{-1} that corresponds to the O-H stretch vibration of the dangling O-H groups pointing out of the water into the vacuum and a broad negative peak in the $\sim 3000 - 3550$ cm^{-1} range, which corresponds to the O-H stretch vibration of H-bonded O-H groups pointing towards the bulk. After blue-shifting the simulated spectra by 50 cm^{-1}, the peak positions as well as the intensities are both in nearly quantitative

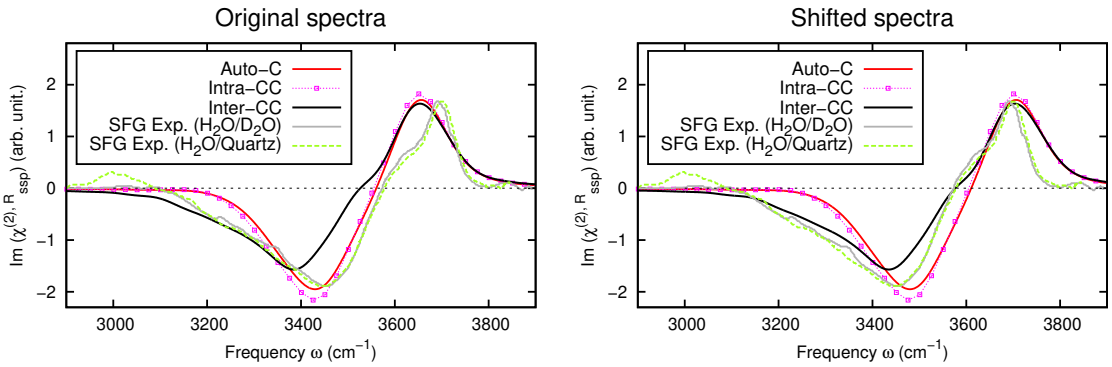

Figure 7.8: Simulated O-H stretch SFG spectra of the water/air interface in terms of the three different correlation terms. The experimental data refers to the usage of D_2O and crystalline quartz as a reference to calibrate the phase and amplitude, respectively. The original SFG spectra are shown in the left panel, whereas in the right panel the peak of the dangling O-H SFG signal was shifted to the corresponding experimental peak position, i.e. by 50 cm^{-1}.

agreement with the experimental data [293]. The only exception is the high frequency region of the dangling O-H peak, where our simulations does not fully reproduce the experimental measurements. Moreover, the shape of the shoulder in the dangling O-H peak is not quantitatively reproduced. In fact, it has been previously reported that the shape of the shoulder cannot be exactly reproduced by the ssVVCF method [58], but only using the direct μ-α TCF approach. Yet, the positive signal at $\sim$ 3000 cm^{-1}, found in SFG experiments using crystalline quartz as a reference [293], is not present in our SFG spectra. Nevertheless, this signal was found to be a bias originating from the contamination and/or adsorbed water on the quartz surface that inevitably affects the quartz reference signal [293,295]. It was also reported that quartz as a reference surface within SFG measurements of the liquid water can generate an additional phase error, which again induces this $\sim$ 3000 cm^{-1} positive signal [293]. In any case, including the Inter-CC effects, the present SFG spectra are in nearly quantitative agreement with those obtained using the more sophisticated many-body potential by Paesani and coworkers [302], as well as *ab-inito* MD simulations of Sulpizi and Gaigeot [63,299,300].

First, we analyze the changes in both peaks in terms of the correlation terms: The dangling O-H peak remains almost unaffected, while the H-bonded O-H peak changes when the intermolecular cross-correlation term is added. As is apparent from Fig. 7.8, introducing the intermolecular cross-correlation term results in a shift of the H-bonded O-H peak position by 50 cm^{-1} from 3430 cm^{-1} to 3380 cm^{-1}. Moreover, the intermolecular cross-correlation term entails a slightly decreased SFG signal in the range of 3380 - 3600 cm^{-1} and at the same time enhanced amplitude between 3000 - 3380 cm^{-1}. This is to say that the inclusion of the intermolecular vibrational coupling effects as obtained by the intermolecular cross-correlation term is essential for the ssVVCF method to reproduce the experimental SFG spectra of the water/air interface. Second, in comparison to previous theoretical studies that have observed a sizable enhancement of the negative peak at $\sim 3000-3350$ cm^{-1} induced by intermolecular coupling effects [58,292,299], our results entails only a smaller such enhancement that is in better agreement with experiment. The latter is due to the fact that the SFG spectra of Fig. 7.8 includes the small but apparently significant contributions of L_2. As can be seen in Fig. 7.7, a new positive peak appears at 3200 cm^{-1}, whereas the dangling O-H peak is vanishing, indicating that single H-donor water molecules are absent in L_2. More importantly, the positive peak of L_2 entails to cancellation with the corresponding peak of L_1 leading to a reduction of the overall SFG signal at 3200 cm^{-1} in agreement with experimental measurements [293].

The impact of NQE can be clearly seen in Fig. 7.9, showing that the inclusion of NQE leads to a blue-shift of $\sim$ 50 cm^{-1} with respect to experimental SFG measurements, whereas neglecting

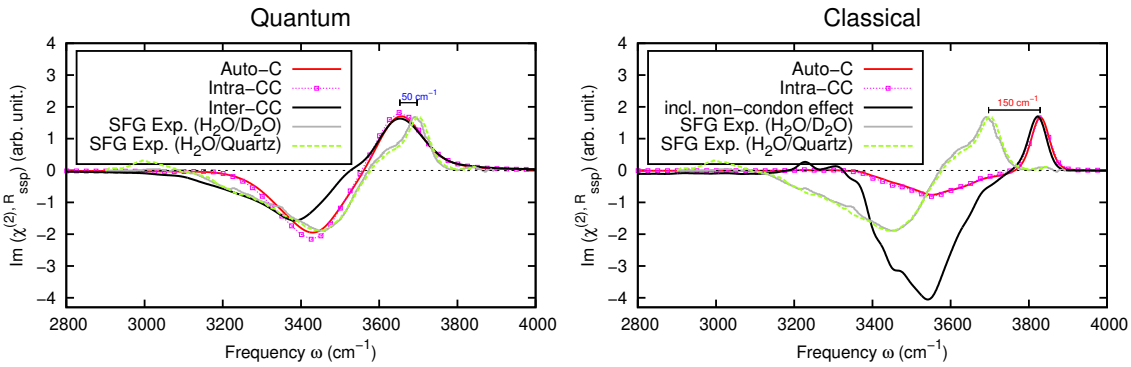

Figure 7.9: Simulated O-H stretch SFG spectra of the water/air interface, with NQE (quantum simulation) and without (classical simulation). For the sake of comparison, the classical simulation was performed with the same computational details as the quantum simulation. However, in the classical simulation the intermolecular cross-correlation term is neglected due to the shorter simulation time (∼40 ps), but as is common practice in classical MD simulations, non-Condon effects were included to enhance the H-bonded O-H peak.

NQE entails a red-shift of $\sim$ 150 cm^{-1}. This is to say that NQE makes up for a blue-shift of as much as $\sim$ 200 cm^{-1} that is a well known phenomenon and have already been reported by previous studies [122,302,324,325]. Yet, neglecting NQE, non-Condon or many-body effects are necessary to obtain good agreement with experimental SFG measurements in terms of the intensities within the H-bonded O-H peak region [58,302].

To study the origin behind the intermolecular vibrational contribution in our SFG spectra, we have separated the intermolecular contribution, which originates from the interfacial water molecules, from the vibrational coupling between the bulk and interfacial water molecules. For that purpose, we distinguish between intralayer and interlayer intermolecular coupling effects. As can be seen in Fig. 7.10, the inclusion of the intermolecular cross-correlation term within the interfacial water layer (dotted green line), results in a slightly enhanced amplitude of the SFG signal at 3200 - 3380 cm^{-1} and a slightly reduced amplitude of the 3380 - 3600 cm^{-1} SFG peak. At the same time, these coupling effects entails a slight red-shift of the H-bonded O-H stretch frequency. However, only a tiny enhancement of the 3350 - 3410 cm^{-1} SFG signal and a red-shift of ∼20 cm^{-1} can be attributed to the 2D H-bonded structure (located in L_1, i.e. the dotted blue line), where the H-bonded network is oriented parallel to the instantaneous water surface [62,63,252]. This is to be expected, since the OH groups involved in such a H-bonded network can generate only a negligible SFG signature due to their orientation parallel to the instantaneous water surface, which we believe is the reason for such a tiny enhancement and red-shift in the spectra. Yet, most intermolecular contributions are due to the interlayer coupling between the interfacial water and L_3 (dashed orange line), whereas the remaining contributions are originating mainly from the coupling between interfacial water layer and L_2. In fact, this remaining contribution can be mainly attributed to the coupling between water molecules in L_1 and L_2, since the total intermolecular contribution from the water molecules of L_2 are very small, as is apparent in Fig. 7.7. The interlayer coupling between more distant layers give rise to a tiny intermolecular contribution to the SFG spectra. All of these results clearly suggest that the intermolecular vibrational contributions in the SFG spectra of water/air interface are governed by the coupling between the SFG active interfacial layer and the SFG inactive centrosymmetric bulk layer.

To elucidate the relationship between the intermolecular vibrational contributions in the SFG spectra and the H-bonding network at the water/air interface, we plot the Inter-CC function corresponding to non-donor (ND), single-donor (SD) and double-donor (DD) water configurations separately, as shown in Fig. 7.11. We find that most of the intermolecular contributions are coming from the

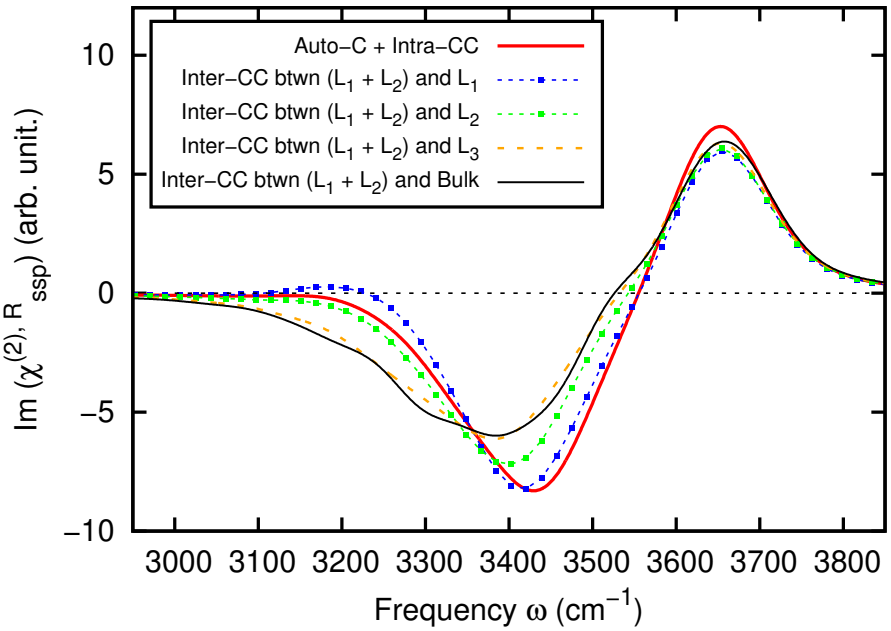

Figure 7.10: Simulated O-H stretch SFG spectra, where the intermolecular coupling effects are separated into intralayer and interlayer contributions. In addition, the SFG spectra including just Auto-C and Intra-CC, but no Inter-CC correlation terms is shown for comparison (red curve).

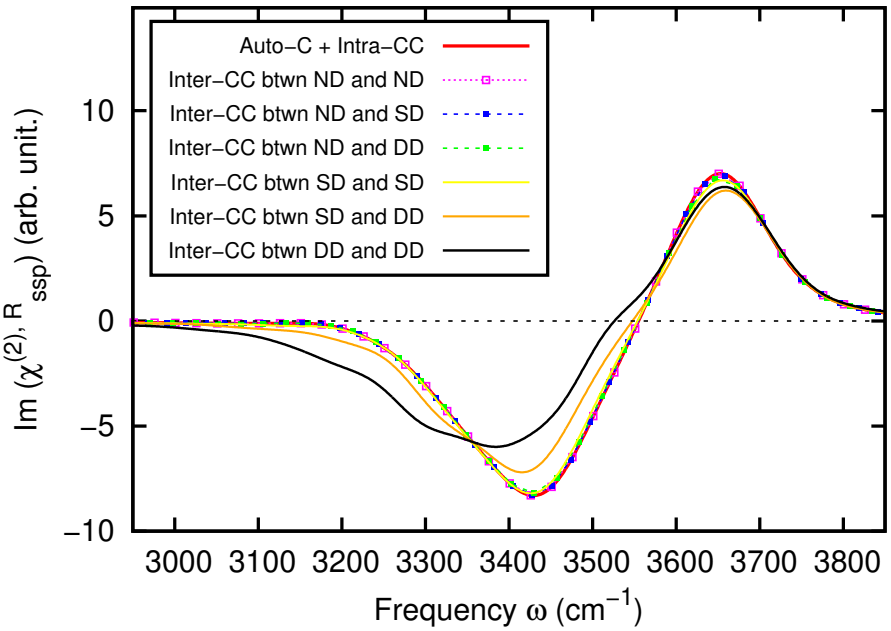

Figure 7.11: Simulated O-H stretch SFG spectra, where the different Inter-CC contributions are shown as a function of the H-bond network of the interfacial water molecules. In addition, the SFG spectra including just Auto-C and Intra-CC, but no Inter-CC correlation terms is shown for comparison (red curve).

intermolecular coupling between DD and DD water configurations (black line), whereas the remaining contributions are coming from the intermolecular coupling between SD and DD water motifs (orange line). The intermolecular coupling between SD and SD water configurations (yellow line) are insignificant for the SFG spectra. Moreover, since the population of ND water motifs are very small at the interface[253], they also are not able to contribute to the spectra. These results clearly suggests that the intermolecular contributions to the SFG spectra are governed by intermolecular coupling effects between DD and DD water, as well as between SD and DD water configurations, which is consistent with previous works of others[63,303,310,311,336].

7.3.2 Correlation between interface water and their SFG signal

Now that we have successfully reproduced the experimental SFG measurement of the water/air interface, we have attempted to correlate the simulated SFG spectra of the water/air interface to the orientation of the interfacial water molecules, which give rise to the OH stretching bands in the spectra. The distorted HB network at the water/air interface contained different types of water species based on orientation, therefore the simulated spectra are broken down into the contributions of each water species and interpreted. The process of decomposition shows each water species' vibrational signature as well as their degree of proximity to one another.

For the purpose of the coming correlations and interpretation, the L_1 shown in the Figure 7.6 is further divided into two regions, region A and region B. This is depicted in Figure 7.12. The Region A is for the molecules in the z-range where the overall density is less than 10 percent of the maximum density of L_1, whereas the region B is for the z-range, where the overall density is greater than 10 percent of the maximum density of L_1. In other words, region A corresponds to the molecules in the most extreme convex points in the capillary wave on the L_1, whereas the region B corresponds to the remaining molecules of L_1.

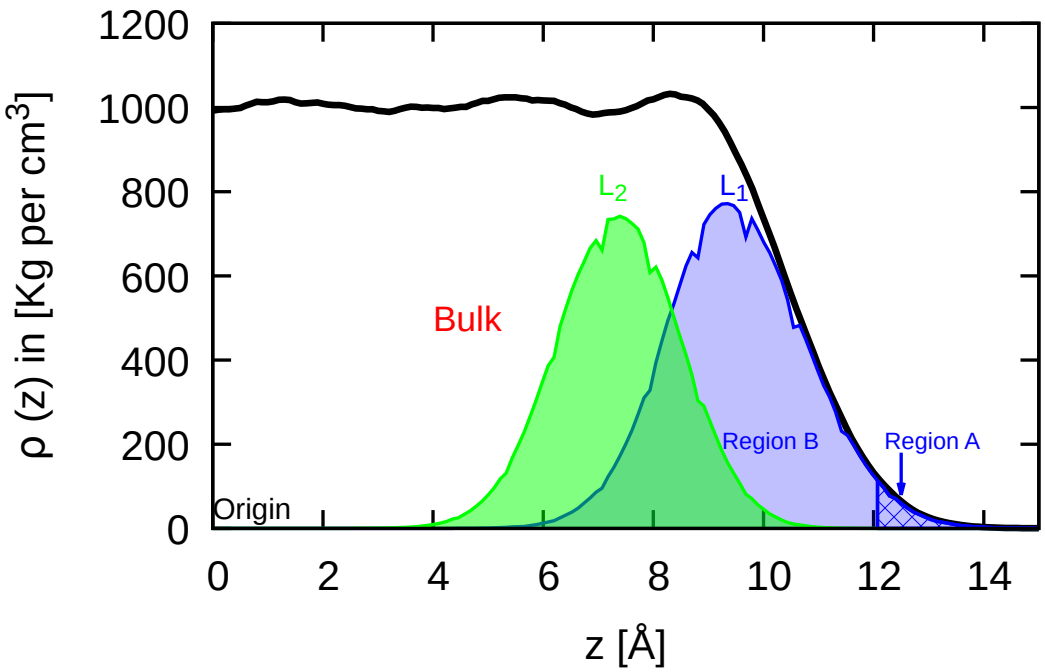

Figure 7.12: The simulated density profiles of the identified instantaneous water layers (L_1 and L_2) as a function of the z-coordinate, as well as of the full water/air interface. A small pattern is drawn in L_1 to distinguish the region A and region B.

For our SFG spectra-water structure correlation, we require a prior knowledge on the structural

information of the identified interfacial molecules. Hence, we have determined the joint angular probability distribution $\mathrm{P}\binom{cos(\xi)}{cos(\tau)}$, where τ is the angle between an OH vector and the surface normal, which is the z-direction pointing towards the air phase. Two values of τ are obtained for every water molecule and ξ is the angle between the molecular dipole and the surface normal. This approach has been previously used by others to characterize the orientation of water molecules near solid interfaces[337]. It is important to note that the distribution $\mathrm{P}\binom{cos(\xi)}{cos(\tau)}$ is obtained relative to an isotropic distribution P_0 given by the following equation,

$$P_0\binom{cos(\xi)}{cos(\tau)} = \left[2\pi\sqrt{sin^2(\frac{\alpha}{2}) - cos^2(\tau) - cos^2(\xi) + 2cos(\xi)cos(\tau)cos(\frac{\alpha}{2})}\right]^{-1} \tag{7.3}$$

where $\alpha = (\sim 109.47^\circ)$ is the angle between the two OH vectors in a water molecule. The two-dimensional plots obtained show the full orientational information which can be correlated to the SFG spectra. Each spot in the plots corresponds to a water species with a certain orientation.

The most important orientation of the interfacial water molecules at the water/air interface are shown in the Figure 7.13. In the region A of L_1, the angular probability distribution is located only at $\binom{1}{0.5}$ and $\binom{-0.5}{0.5}$. These locations correspond to a particular water species (labelled as I) having its molecular dipole pointing towards air, with one of its OH group pointing straight up and the other one pointing downward at an acute angle of 14° along the plane of the interface. The angular probability distribution of region B looks like a 2D Gaussian and is centered at $\binom{0}{0}$, which corresponds to the water species (labelled as IV) having its OH groups dipole as well its molecular dipole both parallel to the interface. The regions around the center point correspond to four different orientations (labelled as II, III, V and VI). Particularly the water species III, IV and V in region B make the so called 2D HB Network[62,63,252] at water/air interface. The angular probability distribution of L_2 shows three distinct distributions. The distributions located at $\binom{-1}{0.5}$ and $\binom{0.5}{0.5}$ correspond to a single water species (labelled as VII) with its molecular dipole pointing downwards, with one of its OH group pointing straight down towards bulk and other one pointing upward at an acute angle of 14° along the plane of the interface. This orientation is mirror image of the orientation of water species I. The remaining distribution at $\binom{0.5}{0.5}$ corresponds to the water species (labelled as VIII) with its molecular dipole and OH group dipoles both pointing upward toward air. Both the OH groups in this water species makes H-bonds with the lone pair of electron in the water of region B. The SFG signal for all the eight water species is shown in Figure 7.14.

L_1: The separated SFG signal reveals the resemblance and divergence in OH stretch vibrational characteristics among all those water species at L_1. The magnitude of the signal reflects the molecular orientation and the peak position of the signal reflects the strength of the H-bonds in the HB network at the interface. The different vibrational characteristics and magnitudes basically shows the heterogeneity in the OH stretch modes at the water/air interface.

The SFG signal of water species $\binom{I}{II}\binom{III}{IV}\binom{V}{VI}$ at L_1 exhibits a $\binom{\text{bimodal distribution with positive and negative peaks}}{\text{bimodal distribution with two positive peaks but overlapping}}\binom{\text{symmetric unimodal positive distribution like normal distribution}}{\text{no distribution}}\binom{\text{left-skewed distribution}}{\text{symmetric negative unimodal distribution}}$. This helps to understand the connectivity and HB strengths in the distorted HB network at the water/air interface. For example, the water species II points upward and make H-bond with the lone pair of electron in water species I in the region A. The OH group in water species V and VI make H-bonds with the lone pair of electron in water species VII in the L_2. The OH groups in water species III, IV and V make the so called 2D intralayer HB Network at the interface[62,63,252]. The water species VI is located at the slope of the capillary wave, where the gradient is very large. In this location, the one of the OH group of this species is very often free, that's why we observe a SFG signal at free OH mode region. This was first

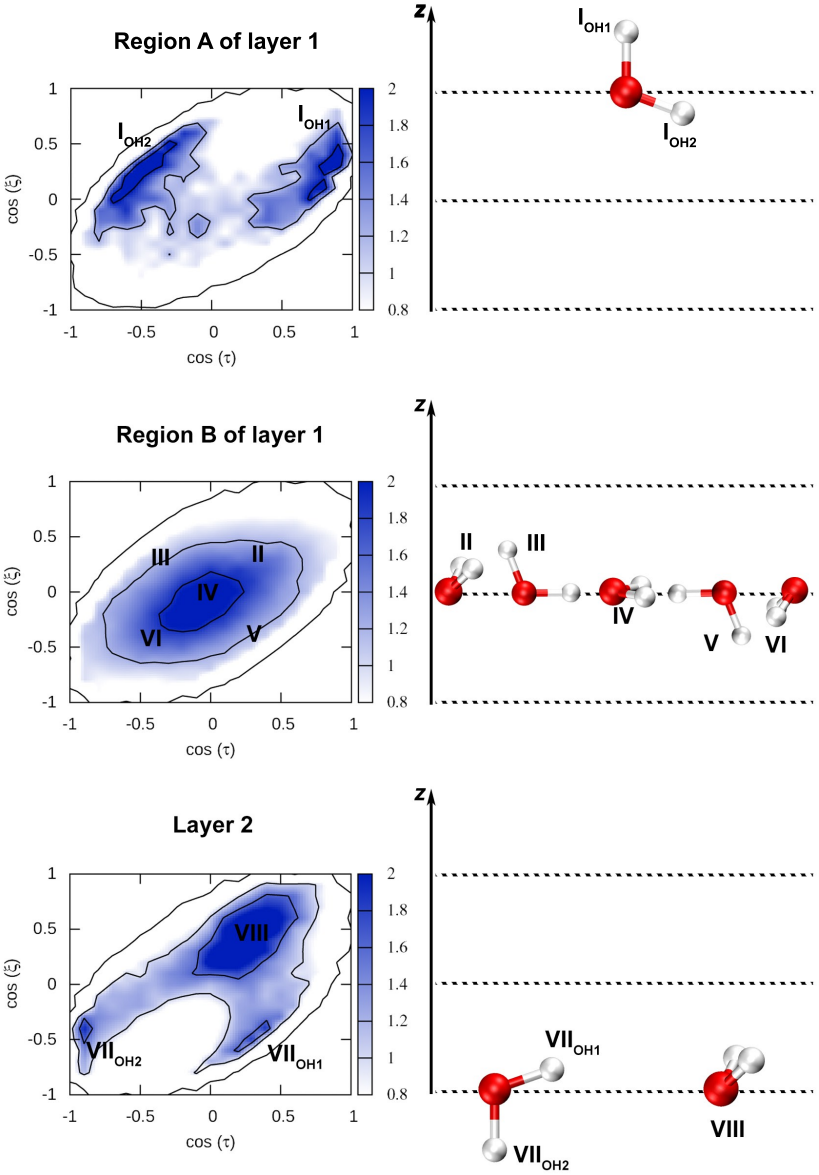

Figure 7.13: Left figure shows the joint angular probability distribution for water molecules in Region A and B of L_1, and for water molecules in L_2. Right figure shows the preferential water orientation in both the layers.

well demonstrated by Nagata and Co-workers [338].

The intermolecular couplings induce same SFG features for all the water species at L_1 and doesn't bring any usefully information for the correlation. However, the coupling induces a small positive peak at 3400 cm^{-1} and a small negative peak at 3200 cm^{-1}, which entail a slightly decreased SFG signal in the range of 3380–3600 cm^{-1} and at the same time enhanced amplitude between 3000–3380 cm^{-1} in the negative H-bonded peak of spectra of L_1. The positive peak at 3400 cm^{-1} is responsible for the shoulder in the SFG spectra of water species III.

L_2: Th water species VIII and VII at L_2 connect the region B in L_1 and the bulk water. Both the species exhibit unimodal distributions in positive and negative directions due to their orientations. The positive and negative distributions from them cancel each other, resulting in a small contribution to the spectra of L_2. The small positive peak at 3200 cm^{-1} appears in the spectra of L_2 can now be undoubtedly attributed to the water species VIII, whereas the negative peak at 3400 cm^{-1} to water

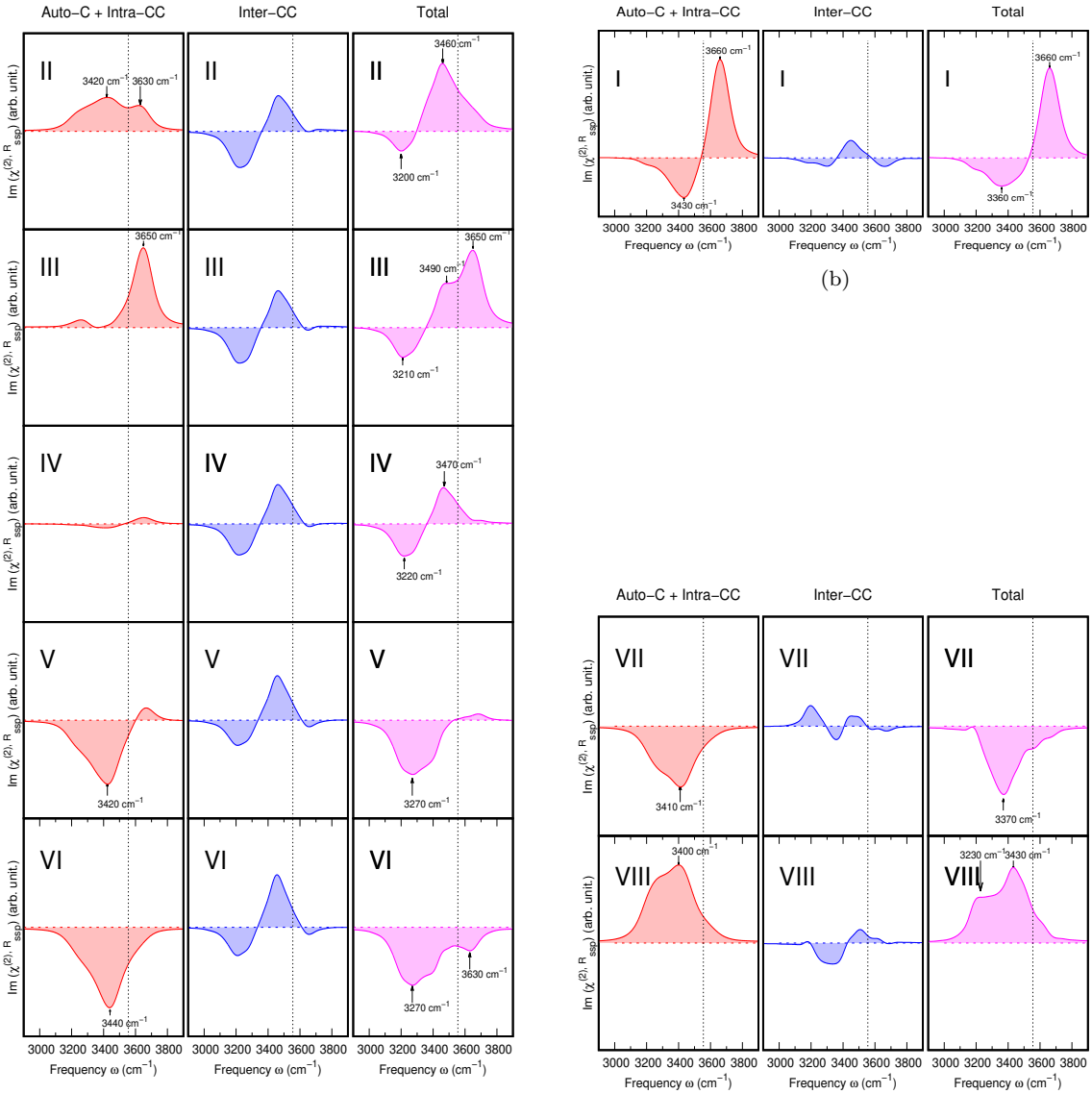

Figure 7.14: The SFG signals of the important water species in Regions A (Figure b) and B (Figure a) located at L_1, and in L_2 (Figure c), respectively.. The intramolecular contributions are shown in the left column, purely intermolecular contributions in the middle, and total contributions in the right column.

species VII. Interestingly, both the water species exhibit mixed symmetric and asymmetric OH stretch modes, which are similar to bulk IR and Raman spectra of liquid water [314].

Interesting findings from the correlations:

- The SFG signal of water species VI exhibits somewhat like a symmetric OH stretching modes, whereas the remaining all of them exhibits strongly asymmetric OH stretching modes due to their strong asymmetric hydrogen bonding environments [9]. In L_2, both the water species exhibit mixed symmetric and asymmetric OH stretch modes, which are similar to bulk IR and Raman spectra of liquid water [314].
- This water species IV is inactive in ssp-polarisation due to its parallel orientation with respect to the interface. However, it also contributes moderately to some of the positive and negative SFG features in the spectra via the intermolecular coupling, as can be clearly seen in the Inter-CC simulated SFG spectra of water species IV.
- Water species III is purely contributing to the sharp positive peak at 3700 cm^{-1} attributed to the free OH groups pointing toward air. Water species VI is purely contributing to the broad negative peak in the spectroscopic range 3200 - 3600 cm^{-1} attributed to the H-bonded OH groups pointing toward.
- From our correlations, we infer that the positive dangling OH group peak in the SFG spectra arises from the water species I, II and III, while the negative H-bonded OH group peak originate from the water species V, VI and VII. The intermolecular contribution, i.e., positive peak at 3400 cm^{-1} and a negative peak at 3200 cm^{-1} from the water species II-VI and bulk water entails a slightly decreased SFG signal in the range of 3380–3600 cm^{-1} and at the same time enhanced amplitude between 3000–3380 cm^{-1} in the negative peak of the spectra.
- The SFG fragments presented here could be used to fit into the experimentally measured SFG spectrum for many aqueous interfaces.

7.4 Conclusion

We have investigated the impact of intermolecular vibrational coupling effects on the of O-H stretch modes in SFG spectra of the water/air interface. We find that these intermolecular coupling effects, as determined using the intermolecular cross-correlation term, induces a red-shift of the H-bonded O-H stretch peak by $\sim$ 50 cm^{-1}. Moreover, they also entail a somewhat decreased SFG signal between 3380 - 3600 cm^{-1}, while, at the same time, leading to an enhanced amplitude at 3000 - 3380 cm^{-1}. Including these intermoleclular coupling effects, leads to systematically improved SFG spectra that are in much better agreement with experimental measurements. Our investigation also shows that the inclusion of intermolecular coupling effects within the first three water layers, i.e. from the water/air interface up to a distance of 6 Å, is essential to quantitatively reproduce experimental SFG spectra. Even though this comes at the price of a somewhat slower convergence with respect to trajectory length (100 ps for $r_t \leq 2$Å, but 500 ps for $r_t \geq 6$Å), we nevertheless believe that the inclusion of these effects should be taken into account in future SFG simulations. Furthermore, based on an instantaneous layer analysis to isolate the contribution of the individual water layer, we find that the intermolecular vibrational contribution to the SFG spectra of the water/air interface is dominated by the coupling between the SFG active interfacial water molecules and SFG inactive bulk water, whereas more distant coupling effects are inessential. Most of the intermolecular contributions within the SFG spectra are due to intermolecular coupling effects between DD and DD water structures, whereas the remaining contributions are mainly from the intermolecular vibrational coupling between SD and DD water motifs. We believe that the correlation between the SFG signal and interface water that

has been presented will help one understand the structural dynamics of the HB network at aqueous interfaces.

Chapter 8

Conclusion

This thesis work primarily complements the time-resolved THz-pump-optic-Raman-probe [44,121] experiments done to deeply understand the intermolecular HB, intermolecular energy transfer and solute-solvent interactions in aqueous systems. This is achieved by reproducing their THz-pulse-induced transient birefringence measurements using the classical DID models, as well as by facilitating the origin and interpretation of the measurements using several theoretical frameworks. The most important theoretical findings of this thesis work are presented below:

We have simulated the THz-electric-field-induced transient collective polarizability anisotropy of pure liquid water and several aqueous salt systems, via simple and molecular hyperpolarizabilities extended DID models, using polarizable and non-polarizable force field MD trajectories. The MD trajectories were directly simulated with the effect of a single-cycle THz pulse used in the time-resolved TKE experiments of Mohsen and Vasileios [121], but with a stronger intensity to overcome statistical problems. Our simulations show that the hyperpolarizabilities extended DID model faithfully reproduces several experimental measurements, while the simple DID model is not sufficient. The comparisons of polarizability anisotropy results of polarizable and non-polarizable force fields show that the inclusion of induced polarization effects [164–166] in force field MD is important to reproduce various experimentally measured concentration-dependent birefringence of aqueous salt systems. Thereby, we suggest that the improvement of non-polarizable force field parameters is strongly required for the water structure and ion solvation in the strong aqueous salt solutions. Furthermore, we also noticed that the improvement of the polarizable force field parameters developed by Martin Head-Gordon and Co-workers [218] for sulfate ion-water interactions is necessary, because the parameterization underestimates (overestimates) the effects of Na_2SO_4 in the polarizability anisotropy (rotation-to-translation KE transfer) calculations.

With the remarkable results of our polarizability anisotropy, separated kinetic energies and rotation-translation cross-correlation function simulations, we have also understood how the energy transfer within the hydrogen bond network of liquid water happens. Our simulations showed that when the single-cycle THz electric pulse is applied in the x-direction of the pure liquid water, the intramolecular energy transfer (or mechanism) from rotation to translation motion of water occurs in less than 100 fms [263] and in the yz- and zy-symmetry. The intramolecular energy transfer process then excites intermolecular energy transfer between two H-bonded water molecules via translation-translation (HB stretching and HB bending modes) motions but not via direct rotation-translation interaction between water molecules. The ensuing intermolecular energy transfer causes the molecular structural anisotropy (i.e., the asymmetric hydrogen bonding environment) and enhanced anharmonicity. Since the latter energy transfer occurs on a timescale of a few hundred femtoseconds, the intramolecular energy transfer of a water molecule is faster than the intermolecular energy transfer between two water molecules [260–262]. All these findings basically demonstrate how the THz pulse energy deposited into the rotational motion of water molecules (IR active) is transferred into the translational motion of

neighboring water molecules (Raman active), which in turn affects the collision-induced contribution to the collective polarizability anisotropy of aqueous systems that is observed in TKE experiments and simulations [44,121].

The decomposition of the simulated polarizability anisotropy of the aqueous salt solutions further reveals that cations strongly increase the collective polarizability anisotropy of water, while anions suppress it. However, the water shared between an anion and a cation exhibit stronger anisotropy than pure liquid water. In addition, we also find that the TKE transform isotropic polarizability of anions into highly anisotropic, while the cations exhibit almost negligible anisotropy. We have further employed ALMO-EDA to measure the strength of the HBs in $MgSO_4$, Na_2SO_4 and $MgCl_2$ aqueous systems. The ALMO-EDA showed that the Mg^{2+} ions in $MgCl_2$ solution with their high charge density lead the water-water HBs in their immediate surrounding to be 2 - 3 kJ/mol stronger than ones in the pure liquid water. On the other hand, in the Na_2SO_4 solution the SO_4^{2-} ions show an opposite trend, namely the neighboring HBs are slightly weaker. Thereby, ions influence the water-water intermolecular HB strength between their first and the second solvation shells. Highly charged cations strengthen this HB interaction and highly charged anions weaken it. As a result, the first solvation shell of strongly charged cation (anion) undergoes intramolecular energy transfer from rotation to translation motion very faster (very slower) compared to pure liquid water. The rapid (slow) intramolecular energy transfer mechanism then excites the intermolecular energy transfer between the first and second solvation shells, respectively. Basically, the ion-induced change in the water-water interaction strength, alters the intermolecular coupling between the rotational and the translational degrees of freedom. As such, the terahertz energy originally deposited into the intermolecular rotational motion of the water is transferred into the translational motions with the efficiency determined by the ionic content of the solution and affects the collision-induced contribution to the collective polarizability anisotropy observed in TKE experiments and simulations [44,121].

The opposite impact of strong anions and cations on the water–water intermolecular interactions is in line with the impact of ion polarity on the stabilization and denaturation of proteins' tertiary structure in aqueous solutions (that is, the Hofmeister effect) [30,339]. While strongly hydrated cations denature proteins, mainly by direct preferential binding to the polar amide groups or by pairing with the protein's negatively charged groups [27,340,341], the mechanism of protein stabilization by strongly hydrated anions remains elusive. Our findings regarding the weakening of the water–water HB strength in the presence of strong anions may support the mechanism suggested by Collins et al., according to which the anion-induced protein stabilization is water mediated and attributed to the 'interfacial effects of strongly hydrated anions near the surface of proteins [342]. Less efficient energy transfer in water and weaker water–water intermolecular interactions may result in converting the liquid into a 'less good solvent' by strong anions, which may drive the proteins to minimize their solvent-accessible surface area by folding [342]. Thereby, we believe that this time-resolved THz-pump-optic-Raman-probe technique can be employed to measure the efficiency of the rotational-translational energy transfer in aqueous solutions and open a new avenue to explore the impact of ions and biological macromolecules on the H-bonding structure of water [343].

Chapter 9

Supplementary information

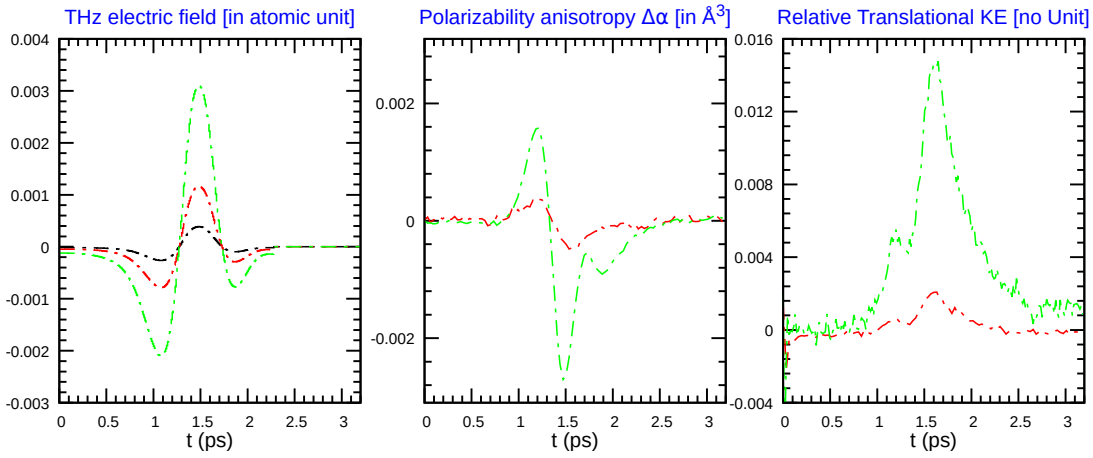

Figure 9.1: The time-varying polarizability anisotropy (middle panel), and translational kinetic energy (right panel) of the simulated SPC liquid water under THz electric pulse with different intensities (left panel). The relative translational KE is about an order of magnitude higher than the polarizability anisotropy.

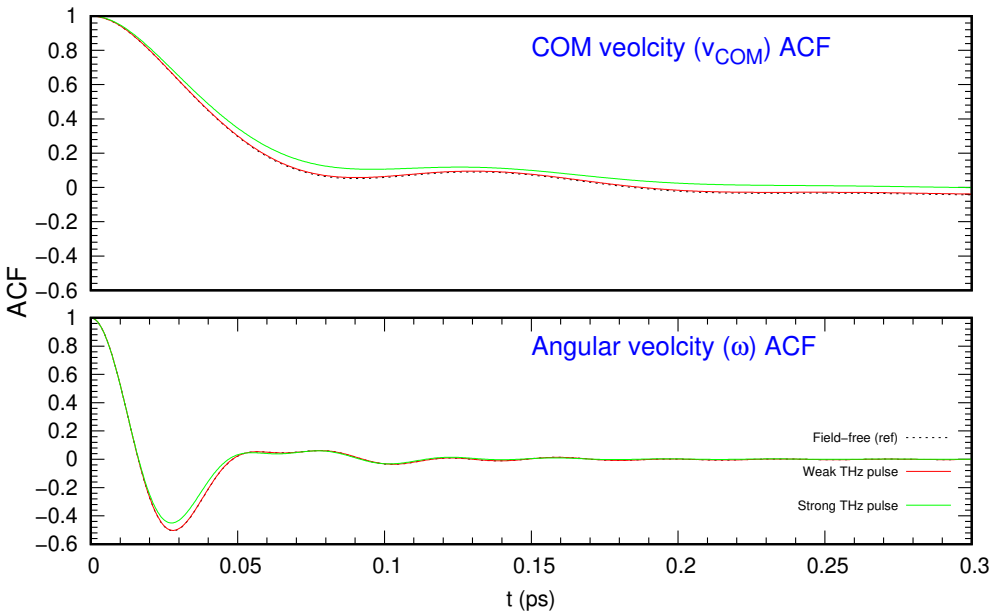

Figure 9.2: The ACFs of the translational and rotational velocities of individual water molecules in SPC liquid water under field-on (strong and weak THz pulses used) and field-free conditions. In this figure, the Cartesian coordinates axis system is used. The field is applied in the x-direction of the system.

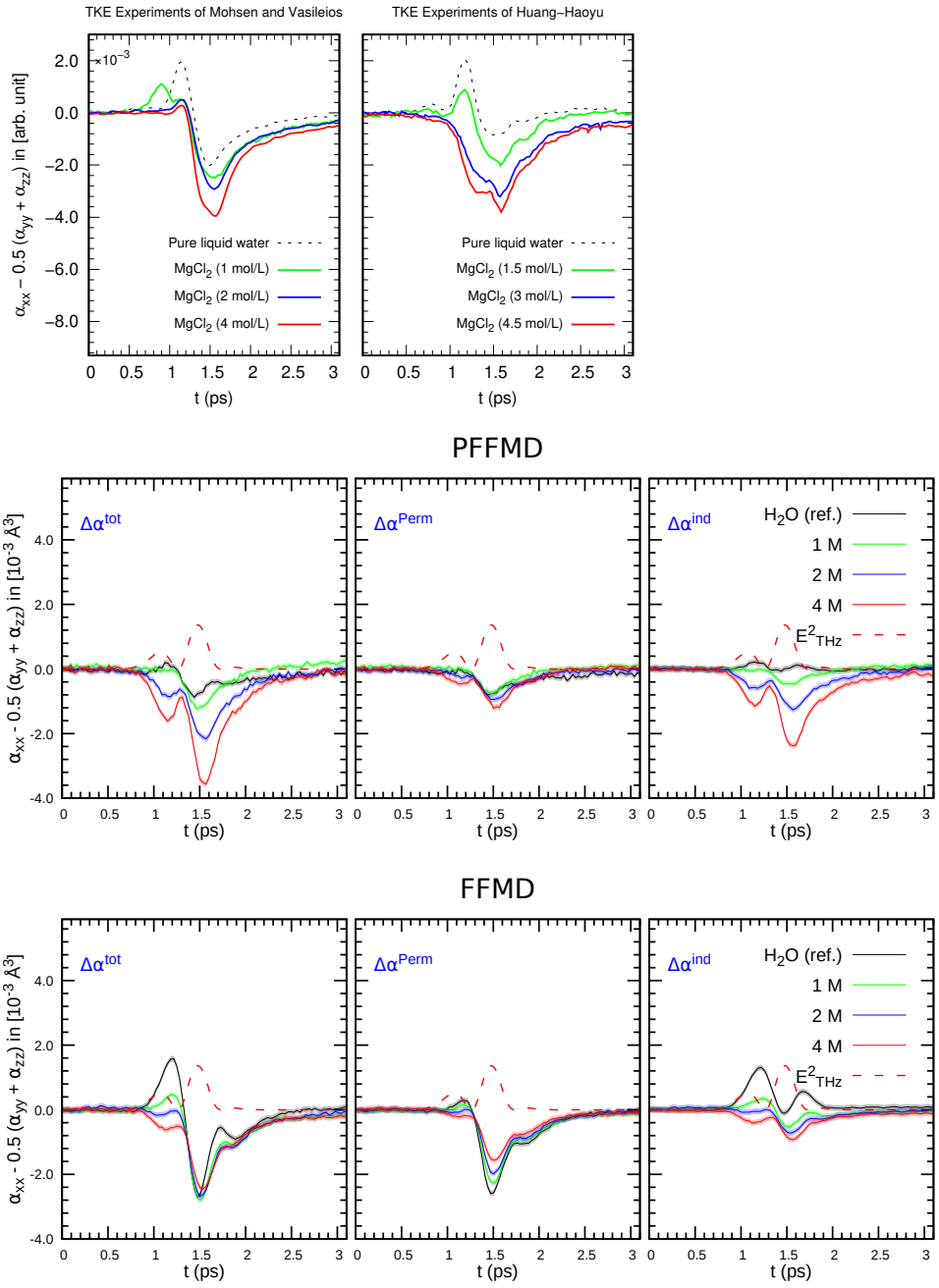

Figure 9.3: The transient polarizability anisotropy of pure liquid water and MgCl2 aqueous systems at three different concentrations, obtained via TKE experiments and MD simulations In the first row of the figure, the experimentally measured concentration-dependent birefringence is shown, whereas in the second and third rows, the simulated polarizability anisotropies of PFFMD and FFMD are shown, respectively. In the second and third rows, the first column shows the total contribution, the second column shows the permanent contribution, and the third column shows the induced contribution. The polarizability anisotropy is calculated via the first- and second-order molecular hyperpolarizabilities of the extended DID model. Experimental data were taken from the Ref. [44,72,121,241].

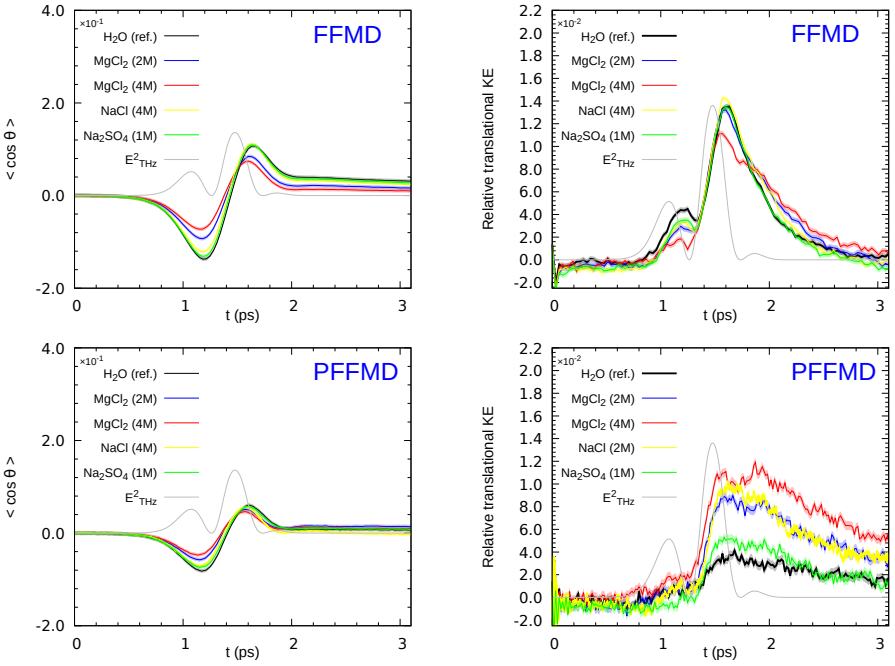

Figure 9.4: Left Figures show the THz-pulse-induced-orientational dynamics of water molecules in various aqueous systems, simulated with FFMD (top panel) and PFFMD (bottom panel). Right Figures show the THz-pulse-induced-tranalstional KE of water molecules in various aqueous systems, simulated with FFMD (top panel) and PFFMD (bottom panel).

Bibliography

[1] P. Ball, *Life's Matrix: A Biography of Water*, American Library Association, 2000.

[2] F. Franks, *Water*, RSC Paperbacks, The Royal Society of Chemistry, 2000.

[3] F. Mallamace, C. Branca, M. Broccio, C. Corsaro, C.-Y. Mou, and S.-H. Chen, Proceedings of the National Academy of Sciences **104**, 18387 (2007).

[4] F. H. Stillinger, Science **209**, 451 (1980).

[5] F. Mallamace, G. Mensitieri, D. Mallamace, M. Salzano de Luna, and S.-H. Chen, International Journal of Molecular Sciences **21** (2020).

[6] C.-C. Yu, K.-Y. Chiang, M. Okuno, T. Seki, T. Ohto, X. Yu, V. Korepanov, H. o Hamaguchi, M. Bonn, J. Hunger, and Y. Nagata, Nature Communications **11** (2020).

[7] H. Elgabarty, N. K. Kaliannan, and T. D. Kühne, Scientific Reports **9** (2019).

[8] T. D. Kühne, M. Krack, and M. Parrinello, Journal of Chemical Theory and Computation **5**, 235 (2009).

[9] C. Zhang, R. Z. Khaliullin, D. Bovi, L. Guidoni, and T. D. Kühne, The Journal of Physical Chemistry Letters **4**, 3245 (2013).

[10] T. Elsaesser, Ultrafast Vibrational Dynamics of Hydrogen-Bonded Dimers and Base Pairs, in *Ultrafast Infrared Vibrational Spectroscopy*, pp. 35–72, CRC Press, 2013.

[11] M. D. Fayer, editor, *Ultrafast Infrared Vibrational Spectroscopy*, CRC Press, 2013.

[12] E. B. Wilson, J. C. Decius, P. C. Cross, and B. R. Sundheim, Journal of The Electrochemical Society **102**, 235C (1955).

[13] M. A. Henderson, Surface Science Reports **46**, 1 (2002).

[14] S. Narayan, J. Muldoon, M. G. Finn, V. V. Fokin, H. C. Kolb, and K. B. Sharpless, Angewandte Chemie International Edition **44**, 3275 (2005).

[15] C. M. Dobson, Nature **426**, 884 (2003).

[16] B. J. F. Pitts, Proceedings of the National Academy of Sciences of the United States of America **107**, 6566 (2010).

[17] J. Y. Luo, W. J. Cui, P. He, and Y. Y. Xia, Nature Chemistry **2**, 760 (2010).

[18] J. A. Killian and G. V. Heijne, Trends in Biochemical Sciences **25**, 429 (2000).

[19] D. Möller, *Chemistry for Environmental Scientists*, De Gruyter, 2022.

[20] K. S. Pitzer, Physics and Chemistry of the Earth **13-14**, 249 (1981).

[21] C. D. Bortner and J. A. Cidlowski, Frontiers in Cell and Developmental Biology **8** (2020).

[22] W. Voigt, Pure and Applied Chemistry **83**, 1015 (2011).

[23] W. Voigt, Pure and Applied Chemistry **87**, 1099 (2015).

[24] L. Suo, O. Borodin, T. Gao, M. Olguin, J. Ho, X. Fan, C. Luo, C. Wang, and K. Xu, Science **350**, 938 (2015).

[25] M. Fang, L. Qiao, M. Wu, Y. Ye, M. Yang, S. Liu, H. Zhang, and X. Ma, Journal of Power Sources **563**, 232815 (2023).

[26] H. I. Okur, J. Hladílková, K. B. Rembert, Y. Cho, J. Heyda, J. Dzubiella, P. S. Cremer, and P. Jungwirth, The Journal of Physical Chemistry B **121**, 1997 (2017).

[27] V. Balos, B. Marekha, C. Malm, M. Wagner, Y. Nagata, M. Bonn, and J. Hunger, Angewandte Chemie **131**, 338 (2018).

[28] L. P. Savtchenko, M. M. Poo, and D. A. Rusakov, Nature Reviews Neuroscience **18**, 598 (2017).

[29] B. Hribar, N. T. Southall, V. Vlachy, and K. A. Dill, Journal of the American Chemical Society **124**, 12302 (2002), PMID: 12371874.

[30] F. Hofmeister, Archiv für Experimentelle Pathologie und Pharmakologie **25**, 189 (1888).

[31] T. D. Kühne and R. Z. Khaliullin, Nature Communication **4**, 1450 (2013).

[32] T. D. Kühne and R. Z. Khaliullin, Journal of the American Chemical Society **136**, 3395 (2014).

[33] A. K. Das, O. N. Demerdash, and T. Head-Gordon, Journal of Chemical Theory and Computation **14**, 6722 (2018).

[34] Y. Mao, O. Demerdash, M. Head-Gordon, and T. Head-Gordon, Journal of Chemical Theory and Computation **12**, 5422 (2016).

[35] S. Kakinuma, T. Ishida, and H. Shirota, The Journal of Physical Chemistry B **121**, 250 (2017).

[36] T. Zhang, Z. Zhang, X. Zhao, C. Cao, Y. Yu, X. Li, Y. Li, Y. Chen, and Q. Ren, Applied Optics **59**, 4775 (2020).

[37] M. Thämer, L. D. Marco, K. Ramasesha, A. Mandal, and A. Tokmakoff, Science **350**, 78 (2015).

[38] M. Galvin and D. Zerulla, ChemPhysChem **12**, 913 (2011).

[39] J. Savolainen, S. Ahmed, and P. Hamm, Proceedings of the National Academy of Sciences **110**, 20402 (2013).

[40] B. D. Bursulaya and H. J. Kim, The Journal of Physical Chemistry B **101**, 10994 (1997).

[41] H. Zhao, Y. Tan, L. Zhang, R. Zhang, M. Shalaby, C. Zhang, Y. Zhao, and X.-C. Zhang, Light: Science & Applications **9** (2020).

[42] H. Zhao, Y. Tan, R. Zhang, Y. Zhao, C. Zhang, X.-C. Zhang, and L. Zhang, Optics Express **29**, 36379 (2021).

[43] H. Zhao, Y. Tan, R. Zhang, Y. Zhao, C. Zhang, and L. Zhang, Optics Letters **46**, 230 (2021).

[44] H. Elgabarty, T. Kampfrath, D. J. Bonthuis, V. Balos, N. K. Kaliannan, P. Loche, R. R. Netz, M. Wolf, T. D. Kühne, and M. Sajadi, Science Advances **6** (2020).

[45] H. Zhao, Y. Tan, T. Wu, R. Zhang, Y. Zhao, C. Zhang, and L. Zhang, Optics Communications **497**, 127192 (2021).

[46] D. Ojha, K. Karhan, and T. D. Kühne, Scientific Reports **8**, 16888 (2018).

[47] C. K. Egan, B. B. Bizzarro, M. Riera, and F. Paesani, Journal of Chemical Theory and Computation **16**, 3055 (2020), PMID: 32250613.

[48] H. Elgabarty and T. D. Kühne, Physical Chemistry Chemical Physics **22**, 10397 (2020).

[49] S. A. Roget, K. A. Carter-Fenk, and M. D. Fayer, Journal of the American Chemical Society **144**, 4233 (2022), PMID: 35226487.

[50] J. A. Fournier, W. Carpenter, L. De Marco, and A. Tokmakoff, Journal of the American Chemical Society **138**, 9634 (2016), PMID: 27404015.

[51] D. H. Dagade and S. S. Barge, ChemPhysChem **17**, 902 (2016).

[52] R. Zhang and W. Zhuang, The Journal of Chemical Physics **140**, 054507 (2014).

[53] Q. Du, R. Superfine, E. Freysz, and Y. R. Shen, Physical Review Letters **70**, 2313 (1993).

[54] Q. Du, E. Freysz, and Y. R. Shen, Physical Review Letters **72**, 238 (1994).

[55] Y. R. Shen and V. Ostroverkhov, Chemical Reviews **106**, 1140 (2006).

[56] N. Ji, V. Ostroverkhov, and Y. R. Shen, Physical Review Letters **100**, 096102 (2008).

[57] Y. R. Shen, The Journal of Physical Chemistry C **116**, 15505 (2012).

[58] T. Ohto, K. Usui, T. Hasegawa, M. Bonn, and Y. Nagata, The Journal of Chemical Physics **143**, 124702 (2015).

[59] N. K. Kaliannan, A. H. Aristizabal, H. Wiebeler, F. Zysk, T. Ohto, Y. Nagata, and T. D. Kühne, Molecular Physics **118**, 1620358 (2020).

[60] D. Ojha, N. K. Kaliannan, and T. D. Kühne, Communications Chemistry **2** (2019).

[61] R. Khatib, T. Hasegawa, M. Sulpizi, E. H. G. Backus, M. Bonn, and Y. Nagata, The Journal of Physical Chemistry C **120**, 18665 (2016).

[62] S. Pezzotti, A. Serva, and M. P. Gaigeot, Journal of Chemical Physics **148**, 174701 (2018).

[63] S. Pezzotti, D. R. Galimberti, and M. P. Gaigeot, Journal of Physical Chemistry Letters **8**, 3133 (2017).

[64] T. Fukasawa, T. Sato, J. Watanabe, Y. Hama, W. Kunz, and R. Buchner, Physical Review Letters **95** (2005).

[65] H. Yada, M. Nagai, and K. Tanaka, Chemical Physics Letters **464**, 166 (2008).

[66] F. Novelli, L. Ruiz Pestana, K. C. Bennett, F. Sebastiani, E. M. Adams, N. Stavrias, T. Ockelmann, A. Colchero, C. Hoberg, G. Schwaab, T. Head-Gordon, and M. Havenith, The Journal of Physical Chemistry B **124**, 4989 (2020), PMID: 32450043.

[67] F. Novelli, C. Y. Ma, N. Adhlakha, E. M. Adams, T. Ockelmann, D. Das Mahanta, P. Di Pietro, A. Perucchi, and M. Havenith, Applied Sciences **10** (2020).

[68] M. Sajadi, M. Wolf, and T. Kampfrath, Nature Communications **8** (2017).

[69] T. Kampfrath, M. Wolf, and M. Sajadi, Chemical Physics Letters **692**, 319 (2018).

[70] T. Kampfrath, R. K. Campen, M. Wolf, and M. Sajadi, The Journal of Physical Chemistry Letters **9**, 1279 (2018).

[71] Y. Xu and M. Havenith, The Journal of Chemical Physics **143**, 170901 (2015).

[72] H. Huang, *Terahertz-induced ultrafast symmetry control in condensed matter*, PhD dissertation, Universität Hamburg, 2020.

[73] G. J. Johnson, Reference Reviews **24**, 32 (2010).

[74] P. V. Rysselberghe, The Journal of Physical Chemistry **36**, 1152 (1932).

[75] E. Ditler, C. Kumar, and S. Luber, The Journal of Chemical Physics **154**, 104121 (2021).

[76] A. Putrino and M. Parrinello, Physical Review Letters **88**, 176401 (2002).

[77] S. Luber, M. Iannuzzi, and J. Hutter, The Journal of Chemical Physics **141**, 094503 (2014).

[78] S. Baroni, S. de Gironcoli, A. Dal Corso, and P. Giannozzi, Reviews of Modern Physics **73**, 515 (2001).

[79] V. F. Rozsa and G. Galli, The Journal of Physical Chemistry B **125**, 2183 (2021).

[80] G. Cassone, J. Sponer, S. Trusso, and F. Saija, Physical Chemistry Chemical Physics **21**, 21205 (2019).

[81] E. Aprà, A. Bhattarai, E. Baxter, S. Wang, G. E. Johnson, N. Govind, and P. Z. El-Khoury, Applied Spectroscopy **74**, 1350 (2020).

[82] Q. Wan, L. Spanu, G. A. Galli, and F. Gygi, Journal of Chemical Theory and Computation **9**, 4124 (2013).

[83] D. M. Wilkins, A. Grisafi, Y. Yang, K. U. Lao, R. A. DiStasio, and M. Ceriotti, Proceedings of the National Academy of Sciences **116**, 3401 (2019).

[84] G. M. Sommers, M. F. Calegari Andrade, L. Zhang, H. Wang, and R. Car, Physical Chemistry Chemical Physics **22**, 10592 (2020).

[85] B. Thole, Chemical Physics **59**, 341 (1981).

[86] P. T. van Duijnen and M. Swart, The Journal of Physical Chemistry A **102**, 2399 (1998).

[87] H. Torii and M. Tasumi, The Journal of Physical Chemistry A **104**, 4174 (2000).

[88] K. Polok, The Journal of Physical Chemistry B **122**, 1638 (2018).

[89] P.-H. Tang and T.-M. Wu, Journal of Molecular Liquids **301**, 112363 (2020).

[90] Z. Pan, T. Wu, T. Jin, Y. Liu, Y. Nagata, R. Zhang, and W. Zhuang, The Journal of Chemical Physics **142**, 212419 (2015).

[91] L. C. Geiger and B. M. Ladanyi, Chemical Physics Letters **159**, 413 (1989).

[92] A. A. Milischuk and B. M. Ladanyi, The Journal of Physical Chemistry B **117**, 15729 (2013).

[93] M. DelloStritto and J. Sofo, The Journal of Physical Chemistry A **121**, 3045 (2017), PMID: 28375616.

[94] P. Hamm, The Journal of Chemical Physics **141**, 184201 (2014).

[95] H. Torii, Chemical Physics Letters **353**, 431 (2002).

[96] M. S. Skaf and S. M. Vechi, The Journal of Chemical Physics **119**, 2181 (2003).

[97] M. T. Sonoda, S. M. Vechi, and M. S. Skaf, Physical Chemistry Chemical Physics **7**, 1176 (2005).

[98] P.-H. Tang and T.-M. Wu, Journal of Molecular Liquids **269**, 38 (2018).

[99] I. Harczuk, O. Vahtras, and H. Ågren, Physical Chemistry Chemical Physics **18**, 8710 (2016).

[100] M. S. Skaf and M. T. Sonoda, Physical Review Letters **94**, 137802 (2005).

[101] M. D. Elola and B. M. Ladanyi, The Journal of Chemical Physics **126**, 084504 (2007).

[102] M. DelloStritto, M. L. Klein, and E. Borguet, The Journal of Physical Chemistry A **123**, 5378 (2019).

[103] I. V. Kurnikov and M. Kurnikova, The Journal of Physical Chemistry B **119**, 10275 (2015).

[104] T. D. Kühne, M. Iannuzzi, M. Del Ben, V. V. Rybkin, P. Seewald, F. Stein, T. Laino, R. Z. Khaliullin, O. Schütt, F. Schiffmann, D. Golze, J. Wilhelm, S. Chulkov, M. H. Bani-Hashemian, V. Weber, U. Borštnik, M. Taillefumier, A. S. Jakobovits, A. Lazzaro, H. Pabst, T. Müller, R. Schade, M. Guidon, S. Andermatt, N. Holmberg, G. K. Schenter, A. Hehn, A. Bussy, F. Belleflamme, G. Tabacchi, A. Glöß, M. Lass, I. Bethune, C. J. Mundy, C. Plessl, M. Watkins, J. VandeVondele, M. Krack, and J. Hutter, The Journal of Chemical Physics **152**, 194103 (2020).

[105] T. D. Kühne, WIREs Computational Molecular Science **4**, 391 (2014).

[106] M. P. Allen and D. J. Tildesley, *Computer simulation of liquids*, Oxford University Press, London, England, 2 edition, 2017.

[107] P. Cieplak, F.-Y. Dupradeau, Y. Duan, and J. Wang, Journal of Physics: Condensed Matter **21**, 333102 (2009).

[108] Z. Jing, C. Liu, S. Y. Cheng, R. Qi, B. D. Walker, J.-P. Piquemal, and P. Ren, Annual Review of Biophysics **48**, 371 (2019).

[109] J. W. Ponder and D. A. Case, Force Fields for Protein Simulations, in *Protein Simulations*, volume 66 of *Advances in Protein Chemistry*, pp. 27–85, Academic Press, 2003.

[110] M. Salanne, Physical Chemistry Chemical Physics **17**, 14270 (2015).

[111] C. Liu, J.-P. Piquemal, and P. Ren, Journal of Chemical Theory and Computation **15**, 4122 (2019), PMID: 31136175.

[112] M. L. Laury, L.-P. Wang, V. S. Pande, T. Head-Gordon, and J. W. Ponder, The Journal of Physical Chemistry B **119**, 9423 (2015).

[113] P. Ren and J. W. Ponder, The Journal of Physical Chemistry B **108**, 13427 (2004).

[114] D. P. Chong, Canadian Journal of Chemistry **96**, 10 (2018).

[115] M. D. Elola and B. M. Ladanyi, The Journal of Physical Chemistry B **110**, 15525 (2006).

[116] F. Ingrosso and B. M. Ladanyi, The Journal of Physical Chemistry B **117**, 654 (2013).

[117] T. Ishida, The Dynamical Properties on Ionic Liquids: Insights from Molecular Dynamics Study, in *Ionic Liquids*, edited by J. ichi Kadokawa, chapter 1, IntechOpen, Rijeka, 2013.

[118] M. Paolantoni and B. M. Ladanyi, The Journal of Chemical Physics **117**, 3856 (2002).

[119] M. Sha, S. A. Yamada, and M. D. Fayer, The Journal of Physical Chemistry B **125**, 3163 (2021).

[120] A. J. Farrell, M. González-Jiménez, G. Ramakrishnan, and K. Wynne, The Journal of Physical Chemistry B **124**, 7611 (2020).

[121] V. Balos, N. K. Kaliannan, H. Elgabarty, M. Wolf, T. D. Kühne, and M. Sajadi, Nature Chemistry **14**, 1031 (2022).

[122] D. Ojha, A. Henao, and T. D. Kühne, The Journal of Chemical Physics **148**, 102328 (2018).

[123] T. Ohto, K. Usui, T. Hasegawa, M. Bonn, and Y. Nagata, The Journal of Chemical Physics **143**, 124702 (2015).

[124] S. Mamatkulov and N. Schwierz, The Journal of Chemical Physics **148**, 074504 (2018).

[125] M. Gonzalez, Collection SFN **12**, 169–200 (2011).

[126] R. Zhou, Molecular modeling at the atomic scale, 2014.

[127] N. J. English and C. J. Waldron, Physical Chemistry Chemical Physics **17**, 12407 (2015).

[128] L. Verlet, Physical Review **159**, 98 (1967).

[129] M. Tuckerman, B. J. Berne, and G. J. Martyna, The Journal of Chemical Physics **97**, 1990 (1992).

[130] W. F. V. Gunsteren and H. J. C. Berendsen, Molecular Simulation **1**, 173 (1988).

[131] N. Bou-Rabee, Entropy **16**, 138 (2014).

[132] U. Stocker, D. Juchli, and W. F. van Gunsteren, Molecular Simulation **29**, 123 (2003).

[133] S. Kim, Physics Procedia **53**, 60 (2014), 26th Annual CSP Workshop on "Recent Developments in Computer Simulation Studies in Condensed Matter Physics", CSP 2013.

[134] B. Bhargava, Chapter 3 - Molecular dynamics simulations of ionic liquids, in *Theoretical and Computational Approaches to Predicting Ionic Liquid Properties*, edited by A. Joseph and S. Mathew, pp. 87–104, Elsevier, 2021.

[135] W. D. Cornell, P. Cieplak, C. I. Bayly, I. R. Gould, K. M. Merz, D. M. Ferguson, D. C. Spellmeyer, T. Fox, J. W. Caldwell, and P. A. Kollman, Journal of the American Chemical Society **117**, 5179 (1995).

[136] S. Kashefolgheta and A. Vila Verde, Physical Chemistry Chemical Physics **19**, 20593 (2017).

[137] S. Kashefolgheta and A. Vila Verde, Physical Chemistry Chemical Physics **20**, 28346 (2018).

[138] I. Soteras Gutiérrez, F.-Y. Lin, K. Vanommeslaeghe, J. A. Lemkul, K. A. Armacost, C. L. Brooks, and A. D. MacKerell, Bioorganic Medicinal Chemistry **24**, 4812 (2016), Advances in Computational and Medicinal Chemistry.

[139] K. Vanommeslaeghe and A. D. MacKerell, Journal of Chemical Information and Modeling **52**, 3144 (2012).

[140] W. Yu, X. He, K. Vanommeslaeghe, and A. D. MacKerell Jr., Journal of Computational Chemistry **33**, 2451 (2012).

[141] K. Vanommeslaeghe, E. P. Raman, and A. D. MacKerell, Journal of Chemical Information and Modeling **52**, 3155 (2012).

[142] K. Vanommeslaeghe, E. Hatcher, C. Acharya, S. Kundu, S. Zhong, J. Shim, E. Darian, O. Guvench, P. Lopes, I. Vorobyov, and A. D. Mackerell Jr., Journal of Computational Chemistry **31**, 671 (2010).

[143] W. Scott, P. Hunenberger, I. Tironi, A. Mark, S. Billeter, J. Fennen, A. Torda, T. Huber, P. Kruger, and W. Gunsteren, The Journal of Physical Chemistry. A: Molecules, Spectroscopy, Kinetics, Environment, General Theory **103**, 3596 (1999).

[144] H. Sun, The Journal of Physical Chemistry B **102**, 7338 (1998).

[145] W. L. Jorgensen, D. S. Maxwell, and J. Tirado-Rives, Journal of the American Chemical Society **118**, 11225 (1996).

[146] B. Doherty, X. Zhong, S. Gathiaka, B. Li, and O. Acevedo, Journal of Chemical Theory and Computation **13**, 6131 (2017).

[147] H. Berendsen, J. Postma, W. van Gunsteren, and J. Hermans, *Interaction Models for Water in Relation to Protein Hydration*, volume 11, pp. 331–342, Springer, 1981.

[148] H. J. C. Berendsen, J. R. Grigera, and T. P. Straatsma, The Journal of Physical Chemistry **91**, 6269 (1987).

[149] W. L. Jorgensen, Journal of the American Chemical Society **103**, 335 (1981).

[150] W. L. Jorgensen, J. Chandrasekhar, J. D. Madura, R. W. Impey, and M. L. Klein, The Journal of Chemical Physics **79**, 926 (1983).

[151] P. Loche, P. Steinbrunner, S. Friedowitz, R. R. Netz, and D. J. Bonthuis, The Journal of Physical Chemistry B **125**, 8581 (2021).

[152] E. A. Vázquez-Montelongo, J. E. Vázquez-Cervantes, and G. A. Cisneros, International Journal of Molecular Sciences **21** (2020).

[153] P. Raiteri, R. Demichelis, and J. D. Gale, The Journal of Physical Chemistry C **119**, 24447 (2015).

[154] M. T. Panteva, G. M. Giambaşu, and D. M. York, Journal of Computational Chemistry **36**, 970 (2015).

[155] H. Nakano, T. Yamamoto, and S. Kato, The Journal of Chemical Physics **132**, 044106 (2010).

[156] J. Picálek, B. Minofar, J. Kolafa, and P. Jungwirth, Physical Chemistry Chemical Physics **10**, 5765 (2008).

[157] S. P. Kadaoluwa Pathirannahalage, N. Meftahi, A. Elbourne, A. C. G. Weiss, C. F. McConville, A. Padua, D. A. Winkler, M. Costa Gomes, T. L. Greaves, T. C. Le, Q. A. Besford, and A. J. Christofferson, Journal of Chemical Information and Modeling **61**, 4521 (2021).

[158] J. W. Ponder, C. Wu, P. Ren, V. S. Pande, J. D. Chodera, M. J. Schnieders, I. Haque, D. L. Mobley, D. S. Lambrecht, R. A. DiStasio, M. Head-Gordon, G. N. I. Clark, M. E. Johnson, and T. Head-Gordon, The Journal of Physical Chemistry B **114**, 2549 (2010).

[159] A. Grossfield, P. Ren, and J. W. Ponder, Journal of the American Chemical Society **125**, 15671 (2003).

[160] Y. Shi, Z. Xia, J. Zhang, R. Best, C. Wu, J. W. Ponder, and P. Ren, Journal of Chemical Theory and Computation **9**, 4046 (2013).

[161] P. Ren and J. W. Ponder, The Journal of Physical Chemistry B **107**, 5933 (2003).

[162] X. He, P. E. M. Lopes, and A. D. MacKerell Jr, Biopolymers **99**, 724 (2013).

[163] D. S. Patel, X. He, and A. D. MacKerell, The Journal of Physical Chemistry B **119**, 637 (2015).

[164] M. Schmollngruber, V. Lesch, C. Schröder, A. Heuer, and O. Steinhauser, Physical Chemistry Chemical Physics **17**, 14297 (2015).

[165] J. Melcr and J.-P. Piquemal, Frontiers in Molecular Biosciences **6** (2019).

[166] G. G. Ferenczy and C. A. Reynolds, The Journal of Physical Chemistry A **105**, 11470 (2001).

[167] T.-M. Chang and L. X. Dang, The Journal of Physical Chemistry A **113**, 2127 (2009).

[168] O. Borodin, The Journal of Physical Chemistry B **113**, 11463 (2009).

[169] F. Thaunay, G. Ohanessian, and C. Clavaguéra, Chemical Physics Letters **671**, 131 (2017).

[170] T. A. Halgren, Journal of the American Chemical Society **114**, 7827 (1992).

[171] A. Stone, Chemical Physics Letters **83**, 233 (1981).

[172] A. J. Stone, Journal of Chemical Theory and Computation **1**, 1128 (2005).

[173] J. J. Molina, S. Lectez, S. Tazi, M. Salanne, J.-F. Dufrêche, J. Roques, E. Simoni, P. A. Madden, and P. Turq, The Journal of Chemical Physics **134**, 014511 (2011).

[174] J. A. Rackers, Z. Wang, C. Lu, M. L. Laury, L. Lagardère, M. J. Schnieders, J.-P. Piquemal, P. Ren, and J. W. Ponder, Journal of Chemical Theory and Computation **14**, 5273 (2018).

[175] https://github.com/TinkerTools/Tinker.

[176] L. Lagardère, L.-H. Jolly, F. Lipparini, F. Aviat, B. Stamm, Z. F. Jing, M. Harger, H. Torabifard, G. A. Cisneros, M. J. Schnieders, N. Gresh, Y. Maday, P. Y. Ren, J. W. Ponder, and J.-P. Piquemal, Chemical Science **9**, 956 (2018).

[177] https://github.com/TinkerTools/tinker-hp.

[178] W. Wang and R. D. Skeel, The Journal of Chemical Physics **123**, 164107 (2005).

[179] F. Aviat, A. Levitt, B. Stamm, Y. Maday, P. Ren, J. W. Ponder, L. Lagardère, and J.-P. Piquemal, Journal of Chemical Theory and Computation **13**, 180 (2017).

[180] J. E. Lennard-Jones, Proceedings of the Physical Society **43**, 461 (1931).

[181] P. P. Ewald, Annalen der Physik **369**, 253 (1921).

[182] U. Essmann, L. Perera, M. L. Berkowitz, T. Darden, H. Lee, and L. G. Pedersen, The Journal of Chemical Physics **103**, 8577 (1995).

[183] H. Wang, P. Zhang, and C. Schütte, Journal of Chemical Theory and Computation **8**, 3243 (2012).

[184] M. J. Harvey and G. De Fabritiis, Journal of Chemical Theory and Computation **5**, 2371 (2009).

[185] M. Deserno and C. Holm, The Journal of Chemical Physics **109**, 7678 (1998).

[186] A. Y. Toukmaji and J. A. Board, Computer Physics Communications **95**, 73 (1996).

[187] K. Zhou and B. Liu, Chapter 3 - Control techniques of molecular dynamics simulation, in *Molecular Dynamics Simulation*, edited by K. Zhou and B. Liu, pp. 67–96, Elsevier, 2022.

[188] G. Raabe, Introduction to statistical mechanics, in *Molecular Simulation Studies on Thermophysical Properties*, pp. 5–30, Springer Singapore, Singapore, 2017.

[189] M. C. G. Lim and Z. Zhong, Building an MD Simulation Program, in *Carbon Nanotubes as Nanodelivery Systems*, Springer Briefs in applied sciences and technology, pp. 7–16, Springer Singapore, Singapore, 2013.

[190] V. Brázdová and D. R. Bowler, *Molecular Dynamics and Monte Carlo*, chapter 6, pp. 75–88, John Wiley Sons, Ltd, 2013.

[191] https://www2.ph.ed.ac.uk/~dmarendu/MVP/MVP03.pdf.

[192] R. Z. Khaliullin, E. A. Cobar, R. C. Lochan, A. T. Bell, and M. Head-Gordon, The Journal of Physical Chemistry A **111**, 8753 (2007).

[193] R. Z. Khaliullin and T. D. Kühne, Physical Chemistry Chemical Physics **15**, 15746 (2013).

[194] D. Manogaran and Y. Subramanian, The Journal of Physical Chemistry B **121**, 11344 (2017), PMID: 29120641.

[195] G. J. Evans and M. W. Evans, Journal of Molecular Liquids **26**, 63 (1983).

[196] G. Evans and M. Evans, Journal of Molecular Liquids **32**, 183 (1986).

[197] M. W. Evans, Journal of Chemical Physics **76**, 5480 (1982).

[198] M. W. Evans, Physical Review A **33**, 1903 (1986).

[199] M. W. Evans, Physical Review Letters **50**, 371 (1983).

[200] M. Evans, Physica B+C **131**, 273 (1985).

[201] M. W. Evans, Journal of Chemical Physics **77**, 4632 (1982).

[202] M. W. Evans, Journal of Chemical Physics **76**, 5473 (1982).

[203] M. W. Evans, Journal of Chemical Physics **78**, 925 (1983).

[204] M. W. Evans, G. C. Lie, and E. Clementi, Physical Review A **36**, 226 (1987).

[205] N. Meyer, V. Piquet, J.-F. Wax, H. Xu, and C. Millot, Journal of Molecular Liquids **275**, 895 (2019).

[206] P. K. Mishra, O. Vendrell, and R. Santra, Angewandte Chemie International Edition **52**, 13685 (2013).

[207] N. K. Kaliannan, Computational Materials Science **135**, 90 (2017).

[208] N. K. Kaliannan, K. Krishnamurthy, S. Sreerama, and A. M. R. J. J. Rathnam, Computational Materials Science **146**, 90 (2018).

[209] J. Horbach, Journal of Physics: Condensed Matter **20**, 244118 (2008).

[210] P. Jungwirth, J. E. Curtis, and D. J. Tobias, Chemical Physics Letters **367**, 704 (2003).

[211] D. Jiao, C. King, A. Grossfield, T. A. Darden, and P. Ren, The Journal of Physical Chemistry B **110**, 18553 (2006).

[212] H. Chen, M. Liu, and T. Yan, Chemical Physics Letters **752**, 137555 (2020).

[213] H. Sekino and R. J. Bartlett, The Journal of Chemical Physics **98**, 3022 (1993).

[214] D. M. Elking, L. Perera, R. Duke, T. Darden, and L. G. Pedersen, Journal of Computational Chemistry **32**, 3283 (2011).

[215] C. Huiszoon, Molecular Physics **58**, 865 (1986).

[216] H. Ito, J.-Y. Jo, and Y. Tanimura, Structural Dynamics **2**, 054102 (2015).

[217] J. Sala, E. Guàrdia, and M. Masia, The Journal of Chemical Physics **133**, 234101 (2010).

[218] D. S. Lambrecht, G. N. I. Clark, T. Head-Gordon, and M. Head-Gordon, The Journal of Physical Chemistry A **115**, 11438 (2011).

[219] P. Raiteri, A. Schuitemaker, and J. D. Gale, The Journal of Physical Chemistry B **124**, 3568 (2020).

[220] M. J. Abraham, T. Murtola, R. Schulz, S. Páll, J. C. Smith, B. Hess, and E. Lindahl, SoftwareX **1-2**, 19 (2015).

[221] R. Hockney, S. Goel, and J. Eastwood, Journal of Computational Physics **14**, 148 (1974).

[222] B. Hess, H. Bekker, H. J. C. Berendsen, and J. G. E. M. Fraaije, Journal of Computational Chemistry **18**, 1463 (1997).

[223] https://github.com/cp2k/cp2k.

[224] G. Lippert, J. Hutter, and M. Parrinello, Molecular Physics **92**, 477 (1997).

[225] J. VandeVondele and J. Hutter, The Journal of Chemical Physics **127**, 114105 (2007).

[226] S. Grimme, J. Antony, S. Ehrlich, and H. Krieg, The Journal of Chemical Physics **132**, 154104 (2010).

[227] R. Resta, Reviews of Modern Physics **66**, 899 (1994).

[228] I. Souza, J. Íñiguez, and D. Vanderbilt, Physical Review Letters **89**, 117602 (2002).

[229] https://github.com/NaveenKaliannan/Dipole-Polarisability.

[230] K. Aidas, C. Angeli, K. L. Bak, V. Bakken, R. Bast, L. Boman, O. Christiansen, R. Cimiraglia, S. Coriani, P. Dahle, E. K. Dalskov, U. Ekström, T. Enevoldsen, J. J. Eriksen, P. Ettenhuber, B. Fernández, L. Ferrighi, H. Fliegl, L. Frediani, K. Hald, A. Halkier, C. Hättig, H. Heiberg, T. Helgaker, A. C. Hennum, H. Hettema, E. Hjertenæs, S. Høst, I.-M. Høyvik, M. F. Iozzi, B. Jansík, H. J. A. Jensen, D. Jonsson, P. Jørgensen, J. Kauczor, S. Kirpekar, T. Kjærgaard, W. Klopper, S. Knecht, R. Kobayashi, H. Koch, J. Kongsted, A. Krapp, K. Kristensen, A. Ligabue, O. B. Lutnæs, J. I. Melo, K. V. Mikkelsen, R. H. Myhre, C. Neiss, C. B. Nielsen, P. Norman, J. Olsen, J. M. H. Olsen, A. Osted, M. J. Packer, F. Pawlowski, T. B. Pedersen, P. F. Provasi, S. Reine, Z. Rinkevicius, T. A. Ruden, K. Ruud, V. V. Rybkin, P. Sałek, C. C. M. Samson, A. S. de Merás, T. Saue, S. P. A. Sauer, B. Schimmelpfennig, K. Sneskov, A. H. Steindal, K. O. Sylvester-Hvid, P. R. Taylor, A. M. Teale, E. I. Tellgren, D. P. Tew, A. J. Thorvaldsen, L. Thøgersen, O. Vahtras, M. A. Watson, D. J. D. Wilson, M. Ziolkowski, and H. Ågren, WIREs Computational Molecular Science **4**, 269 (2014).

[231] O. Vahtras, H. Ågren, P. Jorgensen, H. J. A. Jensen, T. Helgaker, and J. Olsen, The Journal of Chemical Physics **97**, 9178 (1992).

[232] M. Jaszuński, P. Jorgensen, H. Koch, H. Ågren, and T. Helgaker, The Journal of Chemical Physics **98**, 7229 (1993).

[233] D. Jonsson, P. Norman, and H. Ågren, The Journal of Chemical Physics **105**, 6401 (1996).

[234] P. Norman, D. Jonsson, O. Vahtras, and H. Ågren, Chemical Physics Letters **242**, 7 (1995).

[235] A. Luzar and D. Chandler, Nature **379**, 55 (1996).

[236] M. Mantina, A. C. Chamberlin, R. Valero, C. J. Cramer, and D. G. Truhlar, The Journal of Physical Chemistry A **113**, 5806 (2009).

[237] CRC Handbook, *CRC Handbook of Chemistry and Physics, 88th Edition*, CRC Press, 88 edition, 2007.

[238] G. D. Stucky, S. R. Marder, and J. E. Sohn, *Linear and Nonlinear Polarizability*, chapter 1, pp. 2–30, American Chemical Society, 1991.

[239] H. Haken and H. C. Wolf, Molecules in Electric and Magnetic Fields, in *Molecular Physics and Elements of Quantum Chemistry*, pp. 27–49, Springer Berlin Heidelberg, 2004.

[240] E. C. Le Ru and P. G. Etchegoin, Chapter 2 - Raman spectroscopy and related optical techniques, in *Principles of Surface-Enhanced Raman Spectroscopy*, edited by E. C. Le Ru and P. G. Etchegoin, pp. 29–120, Elsevier, Amsterdam, 2009.

[241] V. Balos, N. K. Kaliannan, H. Elgabarty, M. Wolf, T. D. Kühne, and M. Sajadi, Time resolved THz-Raman spectroscopy reveals that cations and anions distinctly modify intermolecular interactions of water, https://doi.org/10.5281/zenodo.6514905, 2022.

[242] P. Zalden, L. Song, X. Wu, H. Huang, F. Ahr, O. D. Mücke, J. Reichert, M. Thorwart, P. K. Mishra, R. Welsch, R. Santra, F. X. Kärtner, and C. Bressler, Nature Communications **9**, 2142 (2018).

[243] M. C. Hoffmann, N. C. Brandt, H. Y. Hwang, K.-L. Yeh, and K. A. Nelson, Applied Physics Letters **95**, 231105 (2009).

[244] J. T. Titantah and M. Karttunen, Scientific Reports **3** (2013).

[245] H. Elgabarty, R. Z. Khaliullin, and T. D. Kühne, Nature Communications **6** (2015).

[246] T. Ishiyama and K. Kitanaka, The Journal of Physical Chemistry C **124**, 23287 (2020).

[247] M. Huš and T. Urbic, The Journal of Chemical Physics **136**, 144305 (2012).

[248] A. Vegiri, Journal of Molecular Liquids **112**, 107 (2004), Recent Progress in Liquid State Theory. A collection of papers in the honour of Professor Myroslav Holovko on the Occasion of his 60th birthday.

[249] Z.-Q. Huang, R.-Y. Yang, W.-Z. Jiang, and Q.-L. Zhang, Chinese Physics Letters **33**, 013101 (2016).

[250] W. Sun, Z. Chen, and S. yi Huang, Journal of Shanghai University (English Edition) **10**, 268 (2006).

[251] T. Todorova, A. P. Seitsonen, J. Hutter, I.-F. W. Kuo, and C. J. Mundy, The Journal of Physical Chemistry B **110**, 3685 (2006).

[252] J. Kessler, H. Elgabarty, T. Spura, K. Karhan, P. Partovi-Azar, A. A. Hassanali, and T. D. Kühne, The Journal of Physical Chemistry B **119**, 10079 (2015).

[253] T. D. Kühne, T. A. Pascal, E. Kaxiras, and Y. Jung, The Journal of Physical Chemistry Letters **2**, 105 (2011).

[254] I.-C. Lin, A. P. Seitsonen, I. Tavernelli, and U. Rothlisberger, Journal of Chemical Theory and Computation **8**, 3902 (2012).

[255] A. Bankura, A. Karmakar, V. Carnevale, A. Chandra, and M. L. Klein, The Journal of Physical Chemistry C **118**, 29401 (2014).

[256] A. Ghalgaoui, B. P. Fingerhut, K. Reimann, T. Elsaesser, and M. Woerner, Physical Review Letters **126**, 097401 (2021).

[257] A. Ghalgaoui, L.-M. Koll, B. Schütte, B. P. Fingerhut, K. Reimann, M. Woerner, and T. Elsaesser, The Journal of Physical Chemistry Letters **11**, 7717 (2020), PMID: 32822177.

[258] M. Sharma, R. Resta, and R. Car, Physical Review Letters **95** (2005).

[259] A. Pasquarello and R. Resta, Physical Review B **68** (2003).

[260] M. Heyden, J. Sun, S. Funkner, G. Mathias, H. Forbert, M. Havenith, and D. Marx, Proceedings of the National Academy of Sciences **107**, 12068 (2010).

[261] I. Ohmine and S. Saito, Accounts of Chemical Research **32**, 741 (1999).

[262] G. E. Walrafen, The Journal of Physical Chemistry **94**, 2237 (1990).

[263] M. L. Cowan, B. D. Bruner, N. Huse, J. R. Dwyer, B. Chugh, E. T. J. Nibbering, T. Elsaesser, and R. J. D. Miller, Nature **434**, 199 (2005).

[264] A. Vegiri, Journal of Molecular Liquids **110**, 155 (2004), Novel Approaches to the Structure and Dynamics of Liquids: Experiments, Theories, and Simulations.

[265] A. Geiger and T. Kowall, Hydrogen Bonding and Molecular Mobility in Aqueous Systems, in *Hydrogen Bond Networks*, pp. 23–35, Springer Netherlands, 1994.

[266] J. Hunger, S. Niedermayer, R. Buchner, and G. Hefter, The Journal of Physical Chemistry B **114**, 13617 (2010), PMID: 20936836.

[267] R. Tomaš, Acta Chimica Slovenica , 531 (2015).

[268] E. Pluhařová, O. Marsalek, B. Schmidt, and P. Jungwirth, The Journal of Physical Chemistry Letters **4**, 4177 (2013).

[269] S. Yue and A. Z. Panagiotopoulos, Molecular Physics **117**, 3538 (2019).

[270] Y. Ding, A. A. Hassanali, and M. Parrinello, Proceedings of the National Academy of Sciences **111**, 3310 (2014).

[271] F. Moučka, I. Nezbeda, and W. R. Smith, Journal of Chemical Theory and Computation **9**, 5076 (2013), PMID: 26583422.

[272] D. D. Tommaso and N. H. de Leeuw, Physical Chemistry Chemical Physics **12**, 894 (2010).

[273] S. Yip, editor, *Handbook of Materials Modeling*, Springer Netherlands, 2005.

[274] I. Waluyo, C. Huang, D. Nordlund, U. Bergmann, T. M. Weiss, L. G. M. Pettersson, and A. Nilsson, The Journal of Chemical Physics **134**, 064513 (2011).

[275] A. Shalit, S. Ahmed, J. Savolainen, and P. Hamm, Nature Chemistry **9**, 273 (2016).

[276] S. Yadav and A. Chandra, The Journal of Physical Chemistry B **122**, 1495 (2018), PMID: 29301399.

[277] T. Urbic, Chemical Physics Letters **610-611**, 159 (2014).

[278] R. Mancinelli, A. Botti, F. Bruni, M. A. Ricci, and A. K. Soper, The Journal of Physical Chemistry B **111**, 13570 (2007), PMID: 17988114.

[279] D. Laage and J. T. Hynes, Proceedings of the National Academy of Sciences **104**, 11167 (2007).

[280] Y. Marcus, *Ion Properties*, pp. 1101–1106, Springer New York, 2014.

[281] H. Kanno, K. Yonehama, A. Somraj, and Y. Yoshimura, Chemical Physics Letters **427**, 82 (2006).

[282] K. J. Tielrooij, N. Garcia-Araez, M. Bonn, and H. J. Bakker, Science **328**, 1006 (2010).

[283] V. Balos, M. Bonn, and J. Hunger, Physical Chemistry Chemical Physics **19**, 9724 (2017).

[284] G. L. Richmond, Chemical Reviews **102**, 2693 (2002).

[285] L. R. Pratt and A. Pohorille, Chemical Reviews **102**, 2671 (2002).

[286] A. G. Lambert, P. B. Davies, and D. J. Neivandt, Applied Spectroscopy Reviews **40**, 103 (2005).

[287] A. Morita, Chemical Physics Letters **398**, 361 (2004).

[288] Y. Nagata and S. Mukamel, Journal of the American Chemical Society **132**, 6434 (2010).

[289] M. Okuno and T. Ishibashi, The Journal of Physical Chemistry C **119**, 9947 (2015).

[290] S. Strazdaite, J. Versluis, E. H. G. Backus, and H. J. Bakker, Journal of Chemical Physics **140**, 054711 (2014).

[291] M. Hankett, Y. Liu, X. Zhang, C. Zhang, and Z. Chen, Journal of Polymer Science Part B: Polymer Physics **51**, 311 (2013).

[292] J. Schaefer, E. H. G. Backus, Y. Nagata, and M. Bonn, Journal of Physical Chemistry Letters **7**, 4591 (2016).

[293] S. Nihonyanagi, R. Kusaka, K. Inoue, A. Adhikari, S. Yamaguchi, and T. Tahara, Journal of Chemical Physics **143**, 124707 (2015).

[294] C. Hsieh, M. Okuno, J. Hunger, E. H. G. Backus, Y. Nagata, and M. Bonn, Angewandte Chemie International Edition **53**, 8146 (2014).

[295] S. Yamaguchi, Journal of Chemical Physics **143**, 034202 (2015).

[296] M. G. Brown, E. A. Raymond, H. C. Allen, L. F. Scatena, and G. L. Richmond, The Journal of Physical Chemistry A **104**, 10220 (2000).

[297] S. Nihonyanagi, T. Ishiyama, T. K. Lee, S. Yamaguchi, M. Bonn, A. Morita, and T. Tahara, Journal of the American Chemical Society **133**, 16875 (2011).

[298] F. Perakis, L. D. Marco, A. Shalit, F. Tang, Z. R. Kann, T. D. Kühne, R. Torre, M. Bonn, and Y. Nagata, Chemical Reviews **116**, 7590 (2016).

[299] R. Khatib and M. Sulpizi, Journal of Physical Chemistry Letters **8**, 1310 (2017).

[300] M. Sulpizi, M. Salanne, M. Sprik, and M. P. Gaigeot, Journal of Physical Chemistry Letters **4**, 83 (2013).

[301] T. Ishiyama, H. Takahashi, and A. Morita, Journal of Physics: Condensed Matter **24**, 124107 (2012).

[302] G. R. Medders and F. Paesani, Journal of the American Chemical Society **138**, 3912 (2016).

[303] D. R. Moberg, S. C. Straight, and F. Paesani, The Journal of Physical Chemistry B **122**, 4356 (2018).

[304] A. Morita and J. T. Hynes, Chemical Physics **258**, 371 (2000).

[305] T. Ishiyama and A. Morita, Annual Review of Physical Chemistry **68**, 355 (2017).

[306] T. Ishiyama and A. Morita, The Journal of Physical Chemistry C **113**, 16299 (2009).

[307] A. Morita and J. T. Hynes, The Journal of Physical Chemistry B **106**, 673 (2002).

[308] B. M. Auer and J. L. Skinner, Journal of Chemical Physics **129**, 214705 (2008).

[309] M. Sovago, R. K. Campen, G. W. H. Wurpel, M. Muller, H. J. Bakker, and M. Bonn, Physical Review Letters **100**, 173901 (2008).

[310] Y. Ni and J. L. Skinner, Journal of Chemical Physics **145**, 031103 (2016).

[311] C. J. Tainter, Y. Ni, L. Shi, and J. L. Skinner, Journal of Physical Chemistry Letters **4**, 12 (2013).

[312] J. H. Choi and M. Cho, Journal of Chemical Physics **138**, 174108 (2013).

[313] C. Zhang, R. Z. Khaliullin, D. Bovi, L. Guidoni, and T. D. Kühne, Journal of Physical Chemistry Letters **4**, 3245 (2013).

[314] B. M. Auer and J. L. Skinner, Journal of Chemical Physics **128**, 224511 (2008).

[315] T. Ohto, H. Tada, and Y. Nagata, Physical Chemistry Chemical Physics **20**, 12979 (2018).

[316] T. Ohto, E. H. G. Backus, C. S. Hsieh, M. Sulpizi, M. Bonn, and Y. Nagata, Journal of Physical Chemistry Letters **6**, 4499 (2015).

[317] T. D. Kühne, M. Krack, F. R. Mohamed, and M. Parrinello, Physical Review Letters **98**, 066401 (2007).

[318] D. Chandler and P. G. J. Wolynes, Journal of Chemical Physics **74**, 4078 (1981).

[319] M. Parrinello and A. Rahman, Journal of Chemical Physics **80**, 860 (1984).

[320] S. Habershon, T. E. Markland, and D. E. Manolopoulos, Journal of Chemical Physics **131**, 024501 (2009).

[321] M. Parrinello and A. Rahman, Physical Review Letters **45**, 1196 (1980).

[322] C. J. Tainter, P. A. Pieniazek, Y. Lin, and J. L. Skinner, Journal of Chemical Physics **134**, 184501 (2011).

[323] J. L. F. Abascal and C. Vega, Journal of Chemical Physics **123**, 234505 (2005).

[324] M. Rossi, M. Ceriotti, and D. E. Manolopoulos, Journal of Chemical Physics **140**, 234116 (2014).

[325] T. Spura, C. John, S. Habershon, and T. D. Kühne, Molecular Physics **113**, 808 (2015).

[326] A. Köster, T. Spura, G. Rutkai, J. Kessler, H. Wiebeler, J. Vrabec, and T. D. Kühne, Journal of Computational Chemistry **37**, 1828 (2016).

[327] C. John, T. Spura, S. Habershon, and T. D. Kühne, Physical Review E **93**, 043305 (2016).

[328] L. B. Partay, G. Hantal, P. Jedlovszky, A. Vincze, and G. Horvai, Journal of Computational Chemistry **29**, 945 (2008).

[329] P. Tarazona and E. Chacon, Physical Review B **70**, 235407 (2004).

[330] G. Hantal, P. Terleczky, G. Horvai, L. Nyulaszi, and P. Jedlovszky, The Journal of Physical Chemistry C **113**, 19263 (2009).

[331] M. Sega, S. S. Kantorovich, P. Jedlovszky, and M. Jorge, Journal of Chemical Physics **138**, 044110 (2013).

[332] M. Matsumoto, Y. Takaoka, and Y. Kataoka, Journal of Chemical Physics **98**, 1473 (1993).

[333] G. G. Lang, ChemTexts **1**, 1 (2015).

[334] A. P. Willard and D. Chandler, The Journal of Physical Chemistry B **114**, 1954 (2010).

[335] https://github.com/DCM-UPB/SFG-spectra-tool.

[336] I. V. Stiopkin, C. Weeraman, P. A. Pieniazek, F. Y. Shalhout, J. L. Skinner, and A. V. Benderskii, Nature **474**, 192 (2011).

[337] F. Sedlmeier, J. Janecek, C. Sendner, L. Bocquet, R. R. Netz, and D. Horinek, Biointerphases **3**, FC23 (2008).

[338] S. Sun, F. Tang, S. Imoto, D. R. Moberg, T. Ohto, F. Paesani, M. Bonn, E. H. G. Backus, and Y. Nagata, Physical Review Letters **121**, 246101 (2018).

[339] Y. Zhang and P. S. Cremer, Annual Review of Physical Chemistry **61**, 63 (2010).

[340] V. Balos, M. Bonn, and J. Hunger, Physical Chemistry Chemical Physics **17**, 28539 (2015).

[341] H. I. Okur, J. Kherb, and P. S. Cremer, Journal of the American Chemical Society **135**, 5062 (2013), PMID: 23517474.

[342] K. D. Collins, Methods **34**, 300 (2004), Macromolecular Crystallization.

[343] R. C. Remsing, T. T. Duignan, M. D. Baer, G. K. Schenter, C. J. Mundy, and J. D. Weeks, The Journal of Physical Chemistry B **122**, 3519 (2018), PMID: 29378124.